The Effects of Tip Clearance on Axial Compressor Pressure Rise

by

Syed Arif Khalid

Submitted to the Department of Mechanical Engineering
in partial fulfillment of the requirements for the degree of

Doctor of Philosophy

at the

MASSACHUSETTS INSTITUTE OF TECHNOLOGY

February 1995

©1995 Syed Arif Khalid. All rights reserved.

The author hereby grants to MIT permission to reproduce and to distribute publicly paper and electronic copies of this thesis document in whole or in part.

Author .....
Department of Mechanical Engineering
August 26, 1994

Certified by .....
Edward M. Greitzer
Thesis Supervisor

Certified by .....
Roger D. Kamm
Thesis Committee Chairman

Certified by .....
Choon S. Tan

Certified by .....
John J. Adamczyk

Accepted by .....
Ain A. Sonin
Chairman, Departmental Commitee on Graduate Students

APR 1995 ARCHIVES

The Effects of Tip Clearance on Axial Compressor Pressure Rise

by

Syed Arif Khalid

Submitted to the Department of Mechanical Engineering
on August 26, 1994, in partial fulfillment of the
requirements for the degree of
Doctor of Philosophy

Abstract

Numerical simulations of the flow in turbomachinery blade rows are used to investigate the effect of blockage due to tip clearance flow on axial compressor pressure rise. Three-dimensional Navier-Stokes computations were employed to examine the flow fields in a low speed stator, a low speed rotor, and a transonic fan. The computations enabled the mechanisms of blockage generation associated with tip clearance to be investigated and the parametric dependence to be determined.

An important aspect in blockage generation is the response of the low total pressure fluid in the vortex core to the passage pressure rise. The total pressure loss of this fluid results from the interaction of the leakage and passage flows prior to vortex roll-up. The role of the vortical structure associated with the clearance flow is primarily one of collecting the high loss fluid and thus setting the level of mixing that occurs for the low total pressure streamtubes.

A method of quantifying blockage in axial compressors was proposed and used with the computed flow fields to determine the design parameters upon which clearance-related blockage depends. A non-dimensional formulation which incorporated the static and relative total pressure changes in the tip region and the relevant blade row parameters collapsed all the computational results into a narrow band of data for normalized blocked area versus aerodynamic loading.

A simple model for clearance-related blockage was also developed, based on the growth of a turbulent wake in a pressure gradient. The results of the model were in good agreement with the three-dimensional computations. The simple model, as well as the parametric dependence, enable the effects of the important parameters and mechanisms to be clearly seen and offer good potential for their inclusion in the design of axial compressors.

Thesis Supervisor: Edward M. Greitzer
Title: H. N. Slater Professor of Aeronautics and Astronautics

Acknowledgments

Read: in the name of your Lord who created,
Created the human being from a clot.
Read: and your Lord is Most Bounteous,
Who taught by the pen,
Taught the human being that which he knew not.
Nay, but verily the human being is rebellious
That he thinks himself independent!
Verily unto your Lord is the return.

— Qur'an 96:1–8

This work was carried out with the support of the Allison Gas Turbine Division of General Motors Corporation which awarded me a GM Fellowship to pursue my doctorate degree. After becoming an independent company Allison Engine Company continued its support. Interest, support, and helpful advice came from Mr. Pete Tramm, my Mentor for the GM Fellowship program, and Dr. Robert Delaney, project monitor.

Now is also a good opportunity to acknowledge United Technologies Corporation for its support of my undergraduate education with the UTC Scholarship.

Thanks is due to my committee consisting of Prof. Ed "C'mon Arif!" Greitzer, Prof. Roger Kamm, Dr. Choon Tan, and Dr. John Adamczyk of NASA Lewis. This group provided the right balance of encouragement and criticism.

In addition I would like to thank Professors Nick Cumpsty, Frank Marble, and Ian Waitz. Their input was invaluable in this work. I also appreciate the advice and encouragement I received from Prof. A. Douglas Carmichael. I received considerable technical help from Dr. Kevin Kirtley and Mr. Mark Celestina at NASA Lewis. Mr. Robert Haimes of MIT went out of his way to support my use of his software.

Some of my colleagues who I would like to thank for their discussions and help are Andy Crook, Scott McNulty, Dave Tew, Amrit Khalsa, John Brookfield, Tonghuo Shang, Dave Darmofal, Diego Diaz, Ken Gordon, Ted Valkov, and Rajesh Khan.

I would also like to thank Ibrahim El Sanhouri, Radhouan Masmoudi, and Samir Nayfeh for their friendship and assistance. I am grateful for my cousins Mariam Tariq and, especially, Mohsin Ansari who made me feel "at home" while at MIT. I cannot express enough thanks to my parents-in-law, Tom and Linda Taylor, for their generosity and support throughout my work.

I wish to express my love to my wife, Pamela Taylor, who postponed her own aspirations to provide a nurturing environment for our children. I thank my daughter, Tasneem, for her patience when I worked late and for entertaining herself on occasions when I had to work and babysit at the same time.

At last I must express my love and appreciation for my mom and dad, Rizwana and Syed J. Khalid. My mom was always supportive. As for my dad, his enthusiasm for engineering was contagious, his advice was valuable, and it is to him that this thesis is dedicated.

Contents

List of Figures

List of Tables

Nomenclature

A	Area
b	Wake width
c	Blade chord
C_x	Inlet area averaged axial velocity
C_P	Pressure coefficient, $\frac{P - P_{t,ref}}{P_{t,ref} - P_{ref}}$
C_{P_t}	Pressure coefficient, $\frac{P_t - P_{t,ref}}{P_{t,ref} - P_{ref}}$
e_t	Absolute total internal energy
H	Enthalpy
P	Static pressure
q_{rms}	Residual convergence criterion
Q	Relative dynamic pressure
s	Blade spacing
t^*	Nondimensional streamwise distance of Chen et al. (1991)
u	Wake velocity
U	Blade tip speed, wake freestream velocity
U_{mid}	Blade speed at midspan
v	Relative velocity
V	Relative velocity magnitude in core region

y	Coordinate direction across boundary layer or wake
y_c^*	Nondimensional vortex center distance from blade of Chen et al. (1991)
β	Relative flow angle, wake depth parameter
δ	Boundary layer thickness
δ^*	Displacement thickness
Δc	Section of blade chord chord
Δl	Length of discrete wake
Γ	Circulation
ρ	Density
ρ_{av}	Mass flow rate/$(A_{in}C_x)$
θ	Wake momentum thickness
τ	Tip clearance
ω	Vorticity

Subscripts

b	Blocked
c	In core region
clr	For the clearance
d	In defect region
e	At edge of defect region
ex	At passage exit (trailing edge)
i	Ideal
in	At inlet near endwall
m	In mainflow direction

n	Normal to the blade surface
r	Radial component
r, θ	Using only r and θ components
ref	Mass averaged at inlet
t	Relative total thermodynamic quantity
vm	Vector mean
x	Axial component
y	In y-direction
z	In z-direction
γ	Component in the blade stagger direction
θ	Tangential component
0	Wake initial condition
12	In plane containing stations 1 and 2
13	In plane containing stations 1 and 3
2τ	At inlet 2τ from endwall
3τ	At inlet 3τ from endwall

Superscripts

$*$	Rotary themodynamic quantity

Operators

$\overline{()}$	Area average
$\overline{()}^a$	Area average over defect region

$\overline{\Delta()}^a$ Area average over defect region minus inlet value at 2τ from endwall

$\Delta_B()$ Difference across blade

Chapter 1

Introduction

1.1 Background

It has long been known that the flow in the endwall region of an axial compressor has a critical influence on overall performance and stability. For example, Wisler (1985) suggests that more than half the loss in an axial compressor is associated with the flow in the endwall region. The data presented by Koch (1981) also emphasizes the detrimental effect of increasing clearance between rotor tip and casing on the maximum pressure rise obtainable within a blade passage. There is thus strong motivation to understand the nature of the endwall flow field and to develop techniques to modify it.

In spite of the importance of the endwall flow field in determining the pressure rise capabilities of axial compressors, complete explanations of the mechanisms by which the endwall flow degrades compressor performance still do not exist. Because of this the present status is that empirical correlations are still employed in the design process.

To illustrate the effect of tip clearance, pressure rise versus mass flow characteristics for four different clearances are shown in Figure 1-1 (Smith and Cumpsty, 1984). The circle symbols indicate data for a compressor with "casing treatment,"

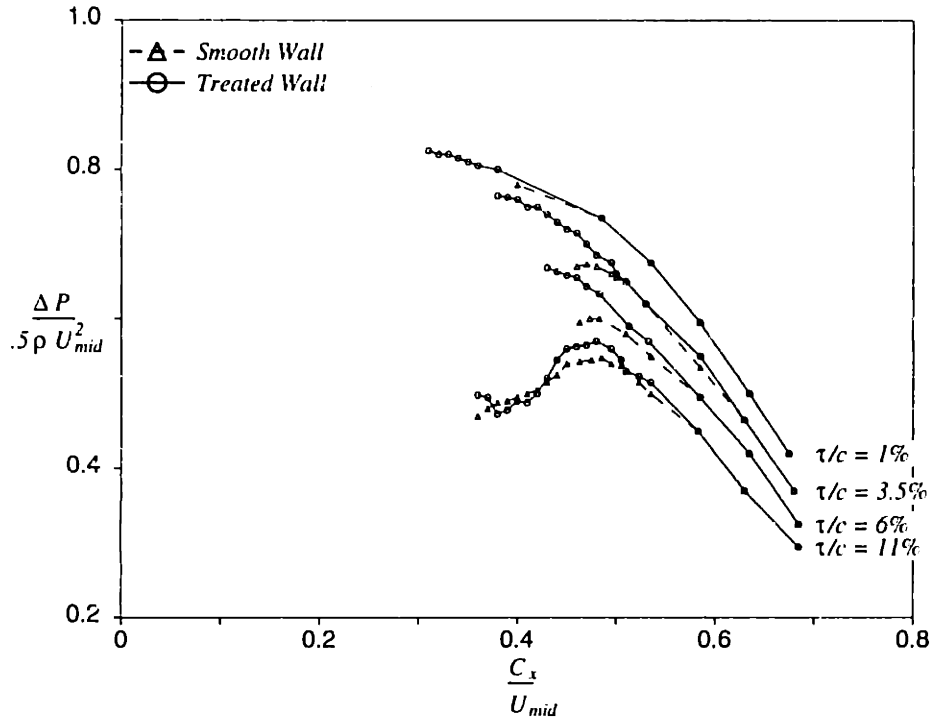

Figure 1-1: Compressor characteristics for several tip clearances from Smith and Cumpsty (1984)

to be described below, but at this point in the discussion only the smooth wall data, indicated by triangle symbols, are considered. As the mass flow through the compressor is decreased the non-dimensional pressure rise across the machine increases. At some value of mass flow, however, the pressure rise peaks and begins to drop. The peaking over of the characteristic is due to the increase in "blockage" and/or "deviation." Blockage is the reduction in effective flow area due to velocity defects. Deviation is reduced turning into the axial direction and hence also reductions in effective area. Further reductions in mass flow can bring about compressor "stall" with a rapid reduction in pressure rise with further reduction in mass flow.

Figure 1-1 shows the detrimental effect of tip clearance on pressure rise capability. Further, the mass flow at which the peak pressure rise occurs increases with increasing tip clearance so that the flow range is decreased. Clearance has little effect on the relative exit angle of the flow away from the endwall, so it is blockage rather than deviation which primarily limits the peak pressure rise. Smith (1970) and Koch (1981) imply that in modern compressors it is usually the flow in the endwall region that

limits the pressure rise capability.

Compressor stall often manifests itself as "rotating stall" in which a region of low throughflow velocity fluid rotates around the annulus of a blade row at some fraction of the rotor speed (Greitzer et al., 1979). The present ideas of rotating stall link its occurrence to the peaking over of the pressure rise characteristic. In compressors in which flow in the tip region is primarily responsible for blockage growth, the onset of rotating stall is thus linked to phenomena associated with clearance flow. Cumpsty (1989, p. 371) states that the airfoil aerodynamic loading away from the endwalls typically cannot account for the onset of the instability. Establishing the mechanisms by which clearance flow degrades pressure rise would help in developing a clear understanding of the features associated with rotating stall inception.

1.2 Previous Work

A summary of previous work which has had a strong influence on the present investigation is presented below.

Probably the most important work in establishing the link between tip clearance and stalling pressure rise is that of Smith (1970). Smith presented an analysis of axial velocity boundary layer displacement thickness, tangential force deficit thickness, static pressure rise, and efficiency, derived from a number of low speed compressor tests. He selected the staggered spacing between blades as the relevant length to normalize the boundary layer thickness. The normalized displacement thickness was related to: (1) the ratio of stage pressure rise to maximum stage pressure rise, and (2) the tip clearance normalized by staggered spacing. This work demonstrated the sensitivity of peak pressure rise to the endwall flow and tip clearance, although it was framed in terms of a circumferentially averaged view of the flow field. Although the term blockage was not used, the importance of the casing boundary layer (and hence the development of blockage associated with clearance) in setting the pressure rise

was clearly brought out.

Koch (1981) investigated the parametric dependence of stalling pressure rise capability of axial flow compressor stages. This work cast the relationship between geometry and stalling pressure rise in terms of parameters analagous to those for two-dimensional diffusers. Correlations of low speed experimental data related the stalling static pressure rise coefficient of a compressor stage to passage geometry, tip clearance, blade row axial spacing and Reynolds number. As with Smith (1970) staggered spacing between blades was used to normalize the clearance in order to correlate the effects of clearance. Koch showed that when the blade row performance was presented in terms of appropriate parameters the stalling pressure rise of a large body of compressor stages followed published trends for two-dimensional diffusers. Koch's contribution is probably second only to Smith (1970) in importance for the current investigation since both identified the causal link between clearance and pressure rise.

Inoue and Kuroumaru (1988) examined the endwall flow structure in a low speed axial compressor rotor passage. They found that with a clearance of roughly 0.5% of blade chord there was a strong interaction between the leakage flow and the incoming passage flow. The clearance vortex appeared to decay with increasing axial distance from the roll-up location near the leading edge of the blade. With a clearance of roughly 3.0% of chord the leakage flow became more prominant at downstream locations and negative axial velocity developed due to the rolling-up of the leakage flow.

Chen et al. (1991) treated the steady three-dimensional flow field of the tip clearance vortex as an unsteady two-dimensional flow with successive streamwise locations represented by successive points in time. Vortex trajectory (x, θ) was shown to be expressed as a single curve for all compressors. Data from a number of compressors were in close agreement with the theory. Since clearance height was the only length scale in the problem, the (x, θ) vortex trajectory was independent of tip clearance.

Storer and Cumpsty (1991) carried out experiments and computations for a linear

compressor cascade with tip clearance. The objective was to clarify mechanisms governing the leakage flow and sources of loss (i.e., reduction in compressor efficiency). The computations were obtained with a three-dimensional Reynolds-averaged Navier-Stokes solver. Comparison of the experimental and computational results showed that the computations captured the flow features associated with tip clearance and allowed a more detailed examination of the flow field than possible with experiment alone.

Using the inviscid leakage model of Rains (1954), Storer and Cumpsty (1991) showed that good predictions of the chordwise leakage velocity and angle distributions could be obtained using the pressures on the suction and pressure sides of the blade at each chordwise location and the total pressure of the fluid entering the clearance. The results imply that the leakage flow is pressure driven and can be related directly to midspan loading.

Storer and Cumpsty (1993) showed that most of the loss due to clearance could be attributed to the mixing of the leakage flow with the mainflow, with little loss occurring within the clearance space. Thus, detailed modeling of the tip region in the Navier-Stokes computations was not necessary for the effects of clearance to be captured by the computational code. An analysis of the loss due to clearance was developed using a control volume model of the blade passage and clearance flow. The model agreed well with their experiments, indicating that most of the clearance-related loss occurs within the passage, is not strongly dependent on the flow details, and can be captured by a control volume approach.

Adamczyk et al. (1993) carried out numerical experiments on the behavior of the tip clearance flow in a high speed fan rotor. They found that the area increase of the clearance vortex as it passes through the in-passage shock is the source of blockage associated with stall. They concluded also that the clearance over the forward portion of the blade controlled the flow processes leading to stall.

The vortical structure of the clearance flow has been mentioned by a number of investigators as an important feature. In this connection Brookfield (1993) clarified

some aspects of the growth of a vortex in an adverse pressure gradient using a simple model for a vortex as well as three-dimensional computations. His computations indicated that the swirl ratios for clearance vortices are typically well below the critical value required for vortex breakdown. Brookfield also showed that there are competing influences on the trajectory of the clearance vortex from streamline divergence and from turbulent dissipation. The former tended to move the vortex away from the suction surface of the blade whereas the effect of turbulence was to bring the vortex toward the suction surface. The two effects were to a large extent compensating.

One technique that has been used successfully to modify the stall point is to employ casing treatment, i.e. slots or circumferential grooves in the casing above the rotor tips. Such treatments have been found to improve the pressure rise capability. For example, the casing treatment configuration used to obtain the data in Figure 1-1 (circle symbols) resulted in increased peak pressure rise and reduced minimum mass flow for a given tip clearance. The operation of casing treatment is of interest not only as a means of improving the pressure rise characteristic, but also as a clue to the mechanisms of stall onset themselves. A review of the effects of tip clearance on axial compressor pressure rise should thus also include findings concerning casing treatment.

Takata and Tsukuda (1977) showed that casing treatment can be effective at improving stall margin for low speed compressors, indicating that the mechanism of casing treatment is not restricted to high speed flows. They suggested that the principal mechanism of slot (as opposed to circumferential groove) type casing treatment is associated with circumferential momentum interchange caused by the injected flow. Slots which were inclined into the casing such that the injected flow swirl was in the opposite sense of the rotor direction (i.e., having the same sense as the clearance vortex) resulted in stall margin improvement. Slots slanted the opposite direction increased the mass flow at which stall occurred.

Greitzer, et al. (1979) sought to explain the operation of casing treatment by

designing experiments in which influence of casing treatment on compressor stability was varied. This work demonstrated that casing treatment was effective at increasing stall margin when the blade row without treatment exhibited "wall" stall as opposed to "blade" stall. Wall stall occurs when the region of low axial velocity is associated with the endwall, blade stall when the flow over the blade surface near midspan separates from the surface. The blade row was converted from a blade stall to a wall stall configuration by doubling the number of blades, resulting in reduced blade loading for the same passage pressure rise coefficient.

Smith and Cumpsty (1984) carried out experiments on a low speed rotor at different tip clearances with and without casing treatment. They concluded that removal of high absolute swirl, high loss fluid from near the endwall, and its reintroduction near the leading edge of the passage is of primary importance. The unsteady effects of the flow near the slots appeared to be of secondary importance.

Cheng et al. (1984) examined the effect of slots in the hub of a cantilevered stator blade row, using this to simulate a rotor casing treatment geometry. They found that the effect of this "hub treatment" was to significantly increase the peak pressure rise and decrease the stalling mass flow for a blade configuration in which the type of stall was endwall (hub) stall as opposed to blade stall. This work was extended by Johnson and Greitzer (1987) who examined the effect of hub treatment on the stator examined by Cheng et al. (1984). They found that the treatment resulted in reduction of blockage and suggested that flow removal near the trailing edge of the passage is an important part of hub and casing treatment.

Lee and Greitzer (1990) investigated the effect of mass injection and suction on stalling pressure rise by independently varying each at the hub of the cantilevered stator blade row examined by Cheng et al. (1984). Both injection and suction were found to be beneficial for increasing pressure rise capability, but neither was as effective as the hub treatment in which both were present. The increase in stalling pressure rise with injection correlated with momentum flux in the streamwise direction, rather

than momentum flux magnitude only, for the injected flow. This suggested that one mechansism of casing treatment operation is the energizing of the endwall flow field.

Crook et al. (1993) used three-dimensional Reynolds-averaged Navier-Stokes computations to interrogate the flow field of a cantilevered compressor stator with clearance at the hub, with and without endwall treatment. The clearance vortex core was found to correspond to high loss fluid and it was suggested that this was an important source of blockage. Streamline traces indicated that the highest loss fluid was that which passed near the blade tip. The effects of endwall treatment were simulated by imposing injection and suction on the hub (i.e., suction near the trailing edge and injection near the leading edge). The computations indicated that the two principal effects of casing treatment are (1) removal of low total pressure, high blockage fluid at the rear of the passage, and (2) energizing the flow in the clearance vortex core.

1.3 Clearance Effects on Endwall Flow Structure

Past work on this topic provides ample reason to regard tip clearance as of primary importance in limiting the pressure rise obtainable in axial compressors. Another approach for assessing the influence of tip clearance is to examine the endwall flow structure directly. Using the computational method described in Section 2.2 different physical effects were eliminated one at a time to determine which have most impact on overall endwall flow structure. The blade passage geometry used is that of the low speed stator described in Section 2.3 with a tip clearance of 1.75% of chord.

Figure 1-2 shows the total pressure coefficient, C_{P_t}, at the trailing edge plane over approximately the bottom 35% of span for four different situations. In the coefficient the total pressure used as reference is the inlet mass averaged value and the dynamic pressure used for normalization is the difference between the mass averaged inlet total and static pressures. Figure 1-2a corresponds to the baseline situation with a clearance of 1.75% of chord, wall motion respect to the blade passage, and inlet

boundary layer skew from 90° at the hub to 51.0° at 12% span. This would be the situation closest to that in a compressor rotor tip region. In Figure 1-2b the conditions are the same except that the hub is stationary. In Figure 1-2c, in addition to fixing the endwall, the inlet hub boundary layer angle is specified as constant (51.0°). Figure 1-2d represents the flow field corresponding to no clearance (Crook et al., 1993).

Eliminating the wall motion or removing the hub boundary layer skew results in minor changes in the endwall flow field. The size and minimum level of the total pressure defect (which is associated with the clearance vortex) in the endwall region is similar for Figures 1-2a–c. However, as pointed out by Crook et al. (1993), eliminating the clearance results in a significant restructuring of the flow field. The majority of the loss is no longer located at mid-pitch, but is now concentrated in the boundary layers. Figure 1-2 illustrates the dominant role of clearance on the endwall flow structure.

1.4 Problem Statement and Research Questions

The purpose of this work is to establish the causal links between tip clearance flow and compressor operating range. This requires that the mechanisms of blockage, or the reduction in effective flow area, associated with clearance be understood.

The specific fluid dynamic questions to be addressed are:

- How do the tip leakage flow, the leakage vortex, and the overall endwall flow structure behave as the compressor mass flow is decreased?
- How can the mechanisms that cause blockage be quantified and their relative importance be assessed?
- What role does the vortical structure associated with the leakage flow play in establishing the blockage?
- How can one develop strategies to best control the endwall fluid dynamics?

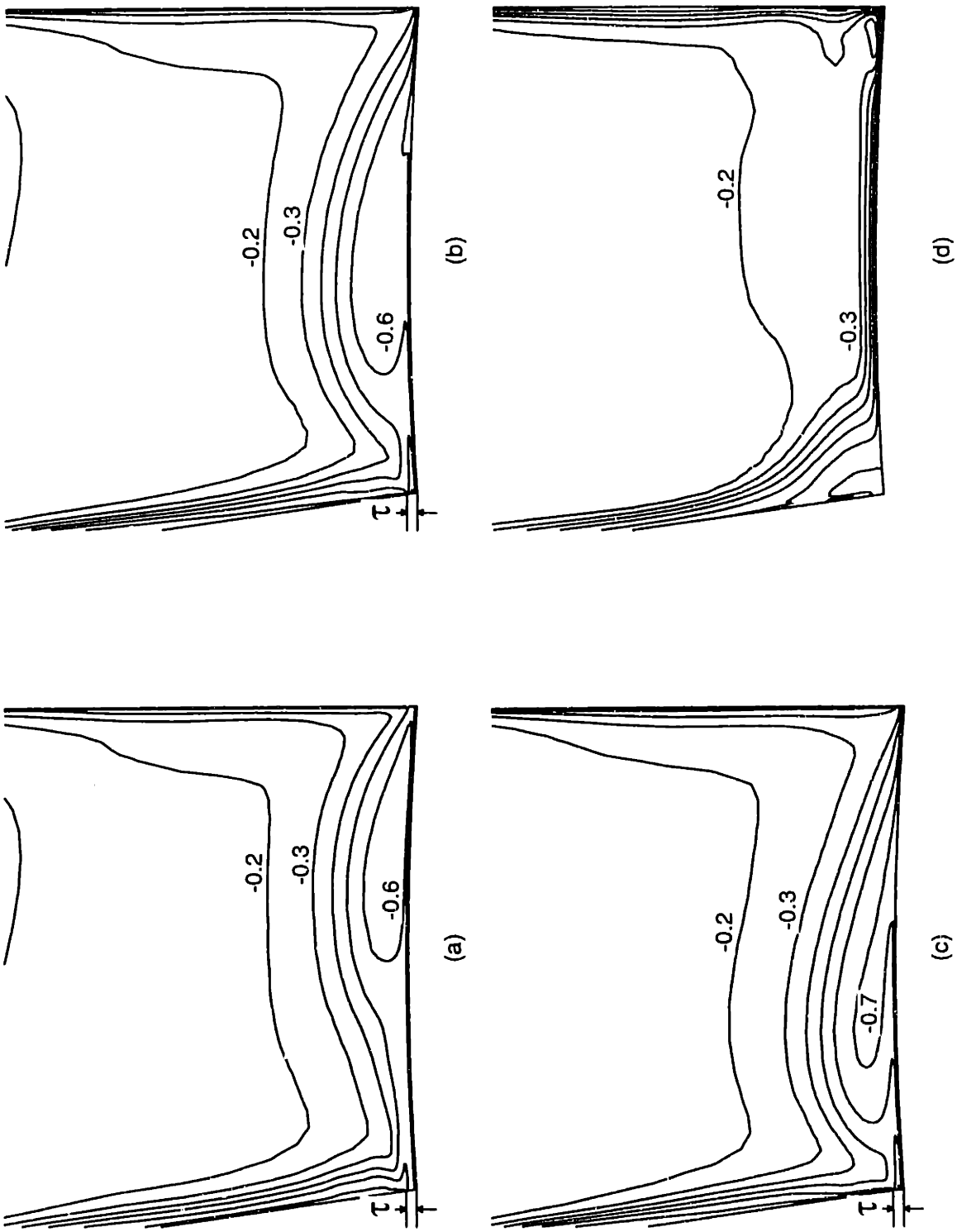

Figure 1-2: Trailing edge C_{P_t} over bottom 35% span of cantilevered stator with (a) wall motion, skewed boundary layer, and clearance; (b) stationary wall, skewed boundary layer, and clearance; (c) stationary wall, collateral boundary layer, and clearance; (d) stationary wall, skewed boundary layer, and no clearance

1.5 Approach to Address Issues

The common conclusion of several computational studies of the flow within a compressor blade passage is that steady three-dimensional Reynolds-averaged Navier-Stokes computations are capable of capturing the the major flow features in the passage. The approach taken in this investigation is to take advantage of such computational methods to address the research questions. Computational grids can generally be more finely spaced than measurement grids, so the flow can be resolved in greater detail. This allows quantification of effects which are difficult to measure in physical experiments. Also, the geometry and boundary conditions are relatively simple to modify, so the effects of changes over the appropriate range of parameters can be examined to identify generic trends.

Work is still underway in the development of computation methods which accurately predict three-dimensional flows. The emphasis in the present study is thus not on absolute values, but rather on identifying the important fluid dynamic phenomena and trends associated with tip clearance. Chapter 2 examines the ability of such a computational approach and shows that it is indeed a useful tool for addressing the issues raised in Section 1.4.

1.6 Contributions of Thesis

The major contributions of the work described in this thesis can be summarized as follows:

- A method of quantifying blockage in axial compressors has been developed.
- The functional relationship between the blockage due to tip leakage and the blade parameters has been extracted from the three-dimensional computations.
- A simple model for the development of blockage incorporating the features of the growth of a two-dimensional wake in an adverse pressure gradient has been

constructed.

- The implications of the functional dependence and simple model controlling the flow in the endwall region have been described and applications for design have been proposed.

1.7 Organization of Thesis

Chapter 2 provides an overview of the computational code used in this work and a discussion of computational issues which were addressed. In Chapter 3, a method for quantifying blockage in an axial compressor blade passage is presented. Chapter 4 covers the fluid dynamic aspects, including the development of a simple model and the parametric dependence of blockage associated with tip clearance. In Chapter 5, the implications of the parametric dependence and the simple model are presented, including applications for these in design. Chapter 6 presents overall conclusions and recommendations for future work.

Chapter 2

Method of Investigation

2.1 Introduction

In this chapter the approach taken to address the research questions is described. Brief discussion of the computational model used to simulate the flow fields is presented and the specific blade passage geometries and flow conditions are described. Finally, the issues which arose in the computational investigation are addressed.

2.2 Description of Computational Procedure

The computed flow fields were obtained using the three-dimensional Navier-Stokes flow solver described by Adamczyk, et al. (1989). The code solves the discretized steady, Reynolds-averaged form of the equations of motion (conservation of mass, momentum, and energy, plus the equation of state) in cylindrical coordinates. The equations are discretized in space and time following the method of Jameson et al. (1981). This means that the flow quantities are solved at cell centers and that the solution marches in time using a four-stage Runge-Kutta algorithm. The code is not time-accurate since local time stepping, based on the CFL number, is used.

The viscosity and heat transfer coefficients in the Reynolds-averaged equations

Blade	h/c	c/s	Stagger	Camber	τ/c %
Stator	1.9	1.2	45°	30°	1.75
	"	"	"	"	3.5
LSR	1.2	1.1	56°	31°	1.4
	"	"	"	"	3.0
	"	1.6	"	"	"
Fan	1.56	1.3	63°	11.4°	.25
	"	"	"	"	1.25
	"	"	"	"	2.0

Table 2.1: Geometric parameters for computed flow fields

are the sum of the laminar and turbulent values. The turbulent viscosity is obtained using the mixing length turbulence model of Baldwin and Lomax (1978) for wall bounded flows. No wake model is used. Stability is maintained in inviscid regions of the flow using a blend of second and fourth order smoothing operators (artificial viscosity), per Jameson et al. (1981). A summary of the formulation of the equations and discretizations is presented by Crook (1989).

2.3 Description of Computations Examined

2.3.1 Common features

Flow fields for three blade geometries were examined computationally: a stator, a low speed rotor, and a transonic fan rotor. All three had been the subjects of experimental investigations and qualitative flow features as well as some quantitative trends were established before the computations were obtained. Grid resolution used for all the geometries was similar. Table 2.1 summarizes the geometric parameters for the stator, low speed rotor (LSR), and transonic fan examined in this study. Tip clearance is presented as a percent of blade chord. A description of the computations examined for each of the geometries is given below.

2.3.2 Cantilevered stator

The stator blade row selected was one used in experiments at MIT described by Johnson (1985). The blades were cantilevered from the casing so that there was a clearance of 3.5% of blade chord at the hub. Using velocity vector data from experiment with this geometry Crook et al. (1993) showed that the Navier-Stokes solver captured the essential features of the endwall flow field. For example, the computations captured the circulation of the clearance vortex to within 16% and the location of the vortex agreed well with experiment.

When the quantititive trends of clearance-related blockage for the stator geometry were desired a grid was generated which was similar to the original, but utilized the periodic blade clearance model described in Section 2.4.5. Computations were also obtained with the clearance set to 1.75% of chord in order to examine the effect of clearance. Flow solutions were obtained for both clearances using the normalized inlet velocity distribution corresponding to the near-stall point in the experiment. Computed flow fields were also obtained with the incidence increased uniformly over the span by two and four degrees, leading to a peaking over of the pressure rise characteristic. Five degrees increased incidence resulted in reduced pressure rise and reverse flow at the exit boundary. Such an exit boundary condition makes the computation improperly specified, so the zero, two, and four degree additional incidence solution were used.

2.3.3 Low speed rotor

The low speed rotor blade row used was the General Electric E^3 Rotor B. The blade design is described by Wisler (1977). The test results upon which the computations were based are presented by Wisler (1981) and correspond to a clearance of 1.6% of chord. The grid dimensions used are those for the baseline grid described in Section 2.4.2. Flow fields for 1.4 and 3.0% clearance/chord were obtained for several loadings by increasing the exit pressure. As a result, computed pressure rise versus

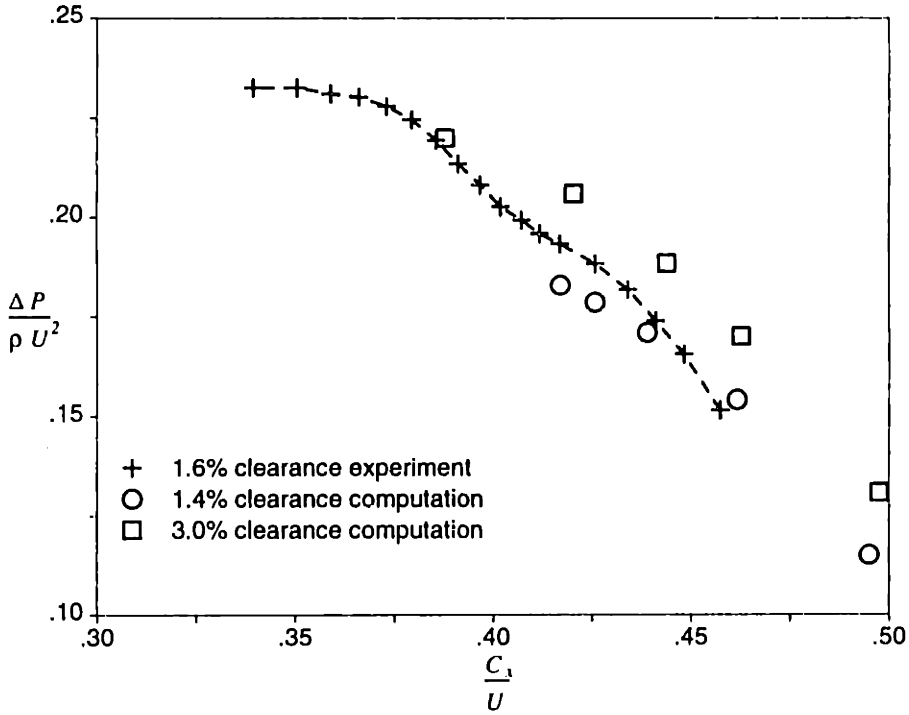

Figure 2-1: Experimental and computed pressure rise characteristics for low speed E^3 rotor

mass flow characteristics could be compared with experiment.

Figure 2-1 shows the experimental results for the rotor blade row as well as the results from the computations at the two clearances. The passage pressure rise coefficient at the casing, $\Delta P/(\rho U^2)$, is plotted against flow coefficient, C_x/U. For the computations with clearance roughly the same as experiment the predicted pressure rise is within 10% of experiment, although the computations underpredict the peak of the characteristic and overpredict the mass flow at which it occurs. With an increase in clearance from 1.4 to 3.0% the decrease in peak pressure rise is roughly 10%. The difference in stage peak pressure rise reported by Wisler (1981) for a change in clearance from 1.6 to 3.4% is 9.7%, a similar change for a comparable increase in clearance. The computations thus do capture the change in pressure rise associated with clearance.

To examine the behavior at a different solidity computations in which the blade spacing was decreased by 50% were also carried out. This geometry is listed as the third row corresponding to "LSR" in Table 2.1.

2.3.4 Transonic fan

The E^3 rotor represented a design for a core compressor. Another geometry of interest is that of a fan with a low hub to tip radius ratio, high stagger, and high Mach number at the tip. The fan examined is NASA Lewis Rotor 67 whose performance has been reported by Strazisar et al. (1989). Computed flow fields obtained with the code used in the present work have been compared with experiment by Adamczyk et al. (1993).

Computed flow fields were obtained at several loadings for three clearances: 0.25, 1.25, and 2.0% of chord. (The 0.25 and 1.25% clearance solutions were obtained by Adamczyk et al., 1993.) The computed trends in total pressure ratio and adiabatic efficiency were in good agreement with experiment.

2.4 Computational Issues

2.4.1 Flow Mach number

The computational method is best suited for moderate to high Mach numbers, so the inlet Mach number for the low speed computations was increased to 0.3 (roughly a factor of two compared to the experiments). The experimental Reynolds number could be maintained by reducing a dimensional length scale input to the code. As will be explained below, rather than setting the experimental Reynolds number for the low speed rotor, the Reynolds number was intentionally doubled in the computations.

2.4.2 Grid resolution

Description of computational grids

Grid requirements Having grid resolution which adequately captures the important flow features is a central concern when conducting any computational study. In particular, the solution should be "grid-independent", i.e., not change significantly with increased grid resolution. Cells must be clustered in regions where high gra-

dients exist. In addition, some rules-of-thumb (Kirtley, 1990) are followed so that non-physical effects are avoided. For example, the ratio of cell lengths in a given direction, called the stretching ratio, should not exceed 1.3. Also, the length of the cell divided by its width, or the cell aspect ratio, should be near unity where the flow is not unidirectional. In regions where the flow is roughly unidirectional, such as boundary layers, large aspect ratios are acceptable.

To avoid numerical errors in the cell-centered scheme, the grid should be as orthogonal as possible. For a simple single-block grid structure this implies that sharp changes in direction along a grid line (as would would be required to make the grid conform to the blade tip) should be avoided. The grid resolution study presented below is for the 3% chord clearance low speed rotor described in Section 2.3.

Relationship between coarse and fine grids To obtain a baseline grid, the results of other researchers were used for reference. Crook et al. (1993) used roughly fifty cells in each direction within the blade passage, but did not determine whether a coarser grid would have sufficed. Storer and Cumpsty (1991) used roughly thirty cells in each direction within the passage and obtained good agreement with experiment. Adamczyk et al. (1993) used thirty cells in the radial and circumferential directions and forty cells from leading to trailing edge for high speed fan and showed good agreement with the experimentally observed performance trends. All of the above cited work was accomplished on algebraic H-type grids.

The baseline grid was thus specified to have thirty cells (thirty-one nodes) in each direction within the passage, a stretching ratio of 1.2 in the axial and circumferential directions, and a stretching ratio of 1.3 in the radial direction. The grid extended roughly 80% axial chord upstream and roughly 100% axial chord downstream of the passage. Overall dimensions for the baseline grid were 61x31x31 (axial, radial, and circumferential directions, respectively). The flow in the clearance gap was simulated using the "periodic-blade" model suggested by Kirtley et al. (1990), in which the flow is transported tangentially through the gap with no loss in mass, momentum, and

energy.

When performing the grid study, Adamczyk (1992) suggested that a fine grid be designed such that the differences between it and the baseline grid be expressed by a single parameter. Increasing the number of cells in each direction by a factor of two (thus, increasing the total number of cells by a factor of eight) corresponded to the upper limit on grid resolution for which the computations could be carried out within reasonable computer run-times (a few days to a week on an IBM RS/6000 Model 580). For the differences between baseline and fine grids to be characterized by a single parameter, it was specified that the fine grid have twice as many cells as the baseline grid in each direction in any region of the flow field. The way to accomplish this is to obtain the fine grid first, then remove every other node in each curvilinear direction from the fine grid to obtain the baseline grid.

Halving the grid resolution as mentioned does not preserve cell stretching ratios. Removing every other node squares the stretching ratio. The objective is to have two grids such that the number of cell divisions along a grid line in both grids differs by the same ratio regardless of the extent of the grid line considered. To accomplish this, an increase in the number of cells in a certain direction by a factor n must be accompanied by a stretching ratio which is the n^{th} root of the stretching ratio of the original grid. The fine grid was thus generated with sixty (2×30) cells in each direction within the passage and with stretching ratios equal to the square root of the desired coarse grid stretching ratios, i.e., the fine grid stretching ratios were $\sqrt{1.2}$, $\sqrt{1.3}$, and $\sqrt{1.2}$ in the axial, radial, and circumferential directions, respectively.

An axial plane at 50% chord for the baseline and fine grids is shown in Figure 2-2. A radial plane at 100% span for the two grids is shown in Figure 2-3.

Effect of cell Reynolds number

Initial computations with the fine grid resulted in a separation bubble appearing on the suction surface over the last 5 percent of chord. It was found that a separation

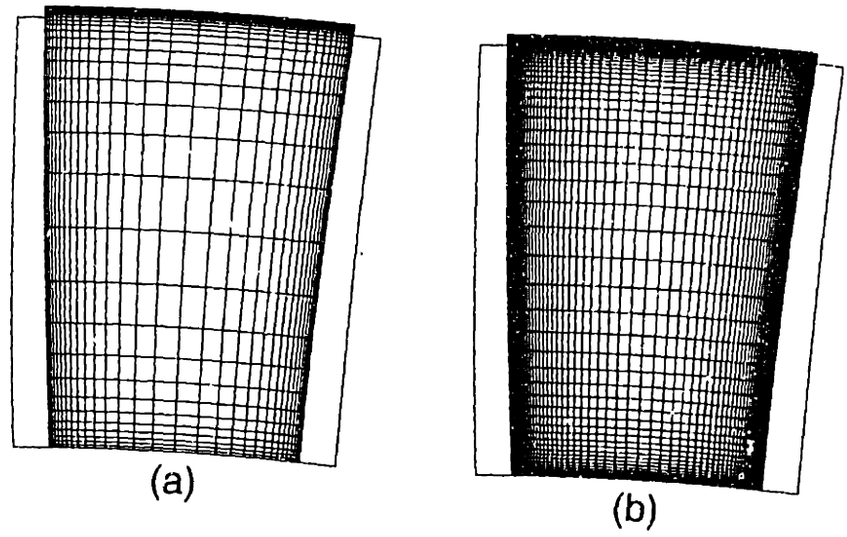

Figure 2-2: Axial planes at 50% chord for (a) baseline grid and (b) fine grid

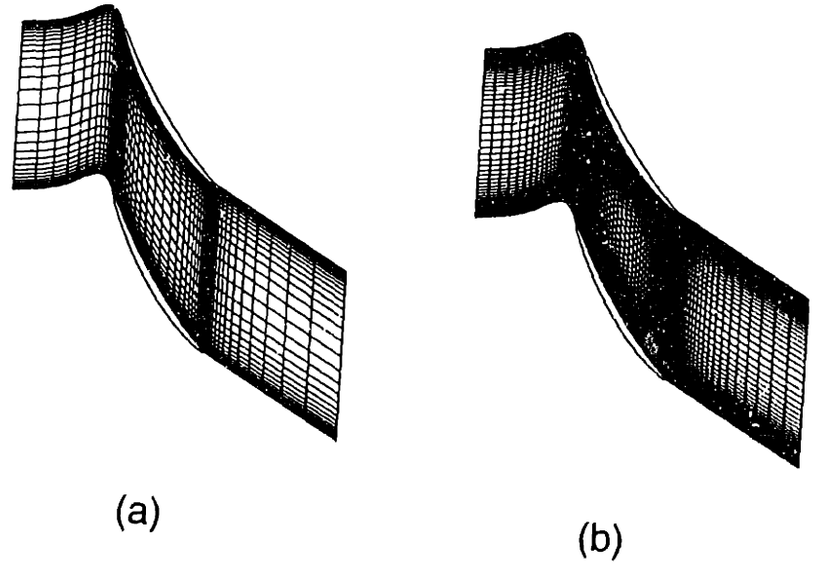

Figure 2-3: Radial planes at 100% span for (a) baseline grid and (b) fine grid

bubble could also be obtained by reducing the flow Reynolds number for a solution with the baseline grid. Since the separation bubble appeared when either the cell size or the flow Reynolds number was reduced, it was concluded that the separation was an effect of changes in the cell Reynolds number. It thus had to be determined whether the appearance of the separation was due to improved flow resolution or to some aspect of the numerics.

For the flow condition examined the Lieblein (1953) diffusion factor was roughly 0.4, well below the value of 0.6 at which blade boundary separation might be expected. The appearance of the separation bubble with increased resolution was thus not viewed as associated with an improved physical modeling due to the increased resolution. A more probable cause was some aspect of the numerical procedure.

The cell Reynolds number depends on local cell size and flow velocity and it affects the number of grid lines within a given y^+ distance from the wall. Cell Reynolds number thus affects both the turbulence model as well as the application of wall functions (which toggled on if the y^+ value of the nearest grid node to the wall exceeds a specified value). Wall functions were not found to affect the development of the bubble, however, so it was concluded that the separation was due to some aspect of the turbulence model.

The experimental Reynolds number (based on inlet relative velocity at midspan and chord) for the low speed rotor was 3.5×10^5. Reducing the flow Reynolds number in the computation by 30% caused the separation bubble to appear for a grid with resolution intermediate between the baseline and fine grids. Thus, the appearance of the separation bubble was sensitive to the flow Reynolds number for the grid in the Reynolds number range examined with the computations. According to Rhoden (1956) the boundary layer behavior in compressor cascades is nearly independent of Reynolds number for Reynolds numbers in excess of 2×10^5. Thus, the Reynolds number sensitivity is peculiar to the computations with the turbulence model.

Having determined that the separation bubble is due to numerical rather than

physical effects, the objective was to prevent its formation so that solutions using the baseline grid and fine grid could be compared. By carrying out the computations with a flow Reynolds number equal to twice that of the experiment the separation bubble was eliminated from the fine grid solution. There was little effect on the flow features of the baseline grid solution.

The influence of Reynolds number demonstrates the need for caution when performing a numerical investigation. The computational code may be suited for a range of parameters which are different from the physical situation being simulated. In such cases, it may be advisable to modify the conditions being simulated to better suit the computational model, provided that the modified flow situation still includes the flow features and relationships of interest.

Comparison of flow features

Grid independence was assessed for a low speed rotor flow field in which the effects of clearance were pronounced. The large clearance (3% of chord) geometry was simulated and the exit pressure used was roughly the maximum possible to obtain a converged solution with that clearance and the specified inlet conditions.

Figure 2-4 shows contours of relative total pressure coefficient, C_{P_t}, at 100% chord for (a) the baseline grid and (b) the fine grid. Differences in the distribution of C_{P_t} are minor. The location and extent of the low energy fluid is roughly the same for the two resolutions examined and the minimum relative total pressure associated with the clearance vortex is approximately the same.

Comparison of integrated quantities

Using the method presented in Chapter 4 trailing edge blockage values were calculated for the baseline and fine grid flow fields. Blockage is defined as blocked area normalized by the total area at the trailing edge station. Both overall blockage and tip region blockage (associated primarily with the tip clearance) are compared in Table 2.2.

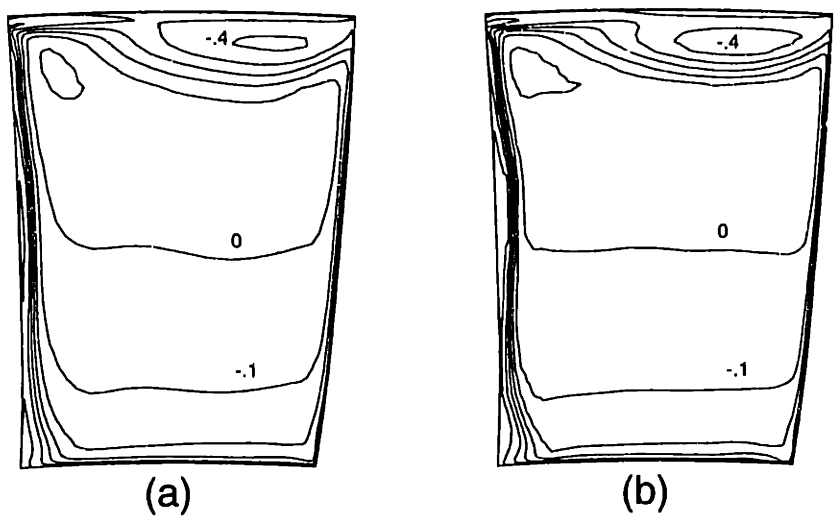

Figure 2-4: C_{P_t} at 100% chord for (a) baseline grid and (b) fine grid

	61x31x31 grid	121x61x61 grid	$\Delta A_b/A_b\%$
Overall A_b/A_{ex}	0.1088	0.1093	+0.4
Tip region A_b/A_{ex}	0.0596	0.0579	-2.9

Table 2.2: Trailing edge blockage comparison between flow fields obtained with baseline and fine grids

The change in blockage associated with grid resolution is only a few percent of the value obtained with the baseline grid. This can be compared with the 8.6% difference in tip region blockage between the maximum exit pressure point (for 3% clearance) and the adjacent operating point on the same characteristic. Also, the difference in tip region blockage between the baseline grid flow field and the 1.4% clearance flow field at roughly the same flow coefficient ($C_x/U = 0.42$) is nearly 100%. Thus, the effect on blockage of doubling the grid resolution in each curvilinear direction is much less than the effect of other changes which are of interest.

Comparison of numerical and turbulent stresses

Doubling the resolution in each of the grid directions resulted in little change in the features associated with the endwall flow. Thus, it would be surprising if there were significant changes in the viscous effects with resolution. One way to confirm grid independence is to compare terms that represent dissipation or viscosity in the equations of motion. There are three sources of dissipation present in the discretized equations: (1) laminar viscosity, (2) turbulent viscosity, and (3) numerical dissipation.

Laminar and turbulent viscosities are present in the physical equations (Reynolds-averaged) and the computational code multiplies a viscosity coefficient with component of the velocity gradient to obtain a shear stress. The shear stress is then multiplied by the cell face area over which it acts to obtain a shear force. The artificial viscosity is only present in the discretized equations and a dissipative operator is used to obtain a force. No "artificial viscosity coefficient" is used with the velocity gradient to obtain a shear force. Thus, the various dissipative effects will be compared by examining the shear force associated with each.

Shear stress contributions themselves are difficult to compare directly since the stress at a point is a tensor quantity. A shear force vector, however, can be obtained for a given computational cell face as the product of the stress tensor and the area normal vector for that face. Summing the shear force vectors corresponding to each

face of the cell yields a resultant shear force vector for that cell. Dividing the shear force vector due to each source of dissipation by the total cell face area yields a shear force per unit area which can be used as a measure of the relative importance of each source of dissipation.

The comparison of the different shear contributions for the baseline and fine grid flow fields can be carried out by plotting the magnitude of the shear force per unit area (due to a given source of dissipation) as if the force acts at cell centers. Since the grid nodes are near cell centers the shear force magnitude per unit area was plotted as if it acts at grid nodes.

In Figure 2-5 the shear force per unit area distributions due to artificial viscosity are compared for the baseline and fine grids. The force magnitude per unit area is normalized by $P_{t,ref} - P_{ref}$ and plotted for the 50% chord axial station. The coarser of the two grids results in peak artificial viscous shear terms in the vortex region which are roughly a factor of 3 greater than those obtained with the fine grid. The regions where contours are absent correspond to low or zero artificial viscosity. The artificial viscosity operator is turned off near solid boundaries.

Figure 2-6 shows the shear force per unit area due to turbulent stresses. The normalization and axial station shown are the same as in Figure 2-5. The turbulent shear stress in the endwall region of the flow field at 50% chord is similar in magnitude and distribution for the baseline and fine grids. For the baseline grid, in the region of peak artificial viscous force magnitude per unit area the turbulent contribution indicated in Figure 2-6a is of similar magnitude. Over much of the in the vortical region the turbulent viscous force per unit area is an order of magnitude or more greater than the artificial viscous force per unit area.

Values of laminar and turbulent viscosity were also compared for the baseline grid flow field. The turbulent viscosity was two to three orders of magnitude greater than the laminar viscosity (which is not a function of grid resolution anyway) in the high loss regions of the clearance vortex at 50% chord.

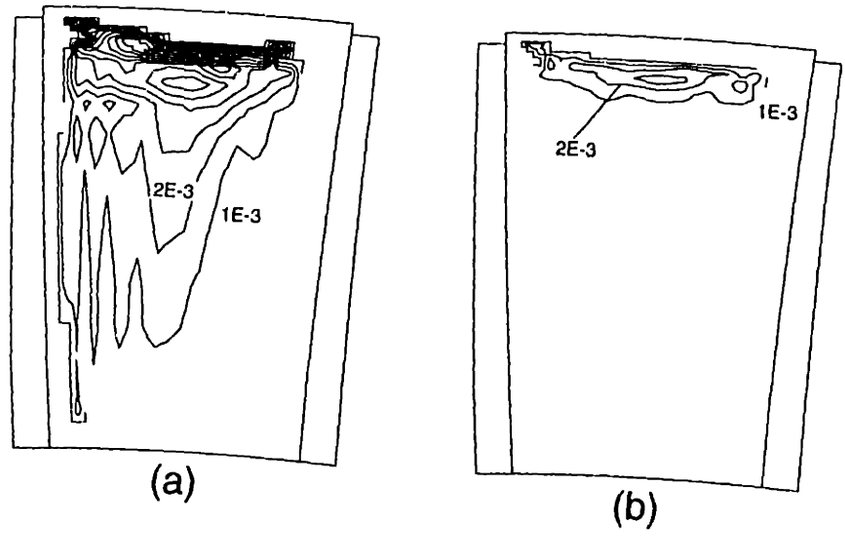

Figure 2-5: Artificial viscous force magnitude per unit area normalized by $P_{t,ref} - P_{ref}$ at 50% chord for (a) baseline grid and (b) fine grid

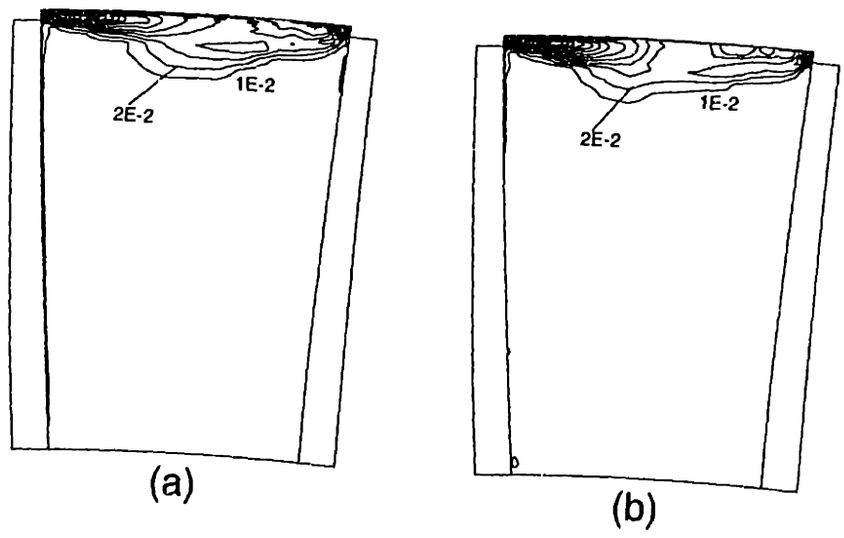

Figure 2-6: Turbulent viscous force magnitude per unit area normalized by $P_{t,ref} - P_{ref}$ 50% chord for (a) baseline grid and (b) fine grid

In summary, over most of the endwall region the shear stress due to turbulent viscosity are at least an order of magnitude greater than stresses due to other sources of dissipation in the computations. The dominance of turbulent dissipation and the similarity of turbulent stress distributions for the flow fields obtained with the two grids confirm that the solution obtained with the baseline grid is grid independent.

2.4.3 Cell aspect ratio

In the course of the investigation a low speed rotor flow field corresponding to a 50% reduction in blade spacing was sought. The grid initially used to obtain a solution was the same as the baseline grid used in the grid study in all respects except that the tangential spacing of radial grid lines was reduced by 50%. Thus, the cell aspect ratio in a given region of the increased solidity grid was different from the cell aspect ratio in a similar region of the baseline grid.

When the reduced spacing grid was used the Navier-Stokes solver would not converge. A new grid was then generated in which the number of cells in the tangential direction was reduced by 50%. Since the number of cells was reduced by a factor of 2/3, the tangential stretching ratio was raised to the power 3/2 to maintain grid similarity, as pointed out in Section 2.4.2. Convergence with this grid was well-behaved. Preserving the cell aspect ratio thus was important to obtain a converged solution.

2.4.4 Inlet boundary condition

The computations are normally carried out by fixing the radial distribution of total pressure at the inlet and the hub static pressure at the exit of the flow domain. The static pressure at the exit boundary is determined by radial equilibrium and the mass flow is determined by the flow solver. Obtaining solutions at lower mass flow rates in the computations involves increasing the specified exit pressure. On the pressure rise versus mass flow characteristic the pressure rise is thus specified and the mass flow is computed.

As the compressor approaches the stall point, the slope of the pressure rise versus mass flow characteristic decreases in magnitude, and the mass flow obtained by the calculation becomes more sensitive to the pressure rise specified. Near the peak of the characteristic two solutions are possible for a given pressure rise: one on the negative-slope side of the characteristic, the other on the positive-slope side.

The objective of the research is to understand the phenomena associated with stall onset so it was desired to obtain computations close to the peak of the compressor characteristic. Thus, the option of running the computations with the mass flow fixed and the pressure rise computed was investigated. Using an inlet boundary condition option in the computational code in which the axial velocity radial distribution is specified, computations were carried with the low speed rotor geometry.

A convergence criterion used was the RMS value (L2 norm) of the time derivatives of the flow variables (residuals) and is defined as

$$q_{rms} = \sqrt{\frac{\sum_{n=1}^{N}\left[\left(\frac{d\rho}{dt}\right)^2+\left(\frac{d\rho v_x}{dt}\right)^2+\left(\frac{d\rho v_r}{dt}\right)^2+\left(\frac{d\rho v_\theta}{dt}\right)^2+\left(\frac{d\rho e_t}{dt}\right)^2\right]}{5N}}$$

where the index n denotes the cell centers within the domain, N is the total number of such locations, and the time-derivatives are computed using their discrete approximations. The variables ρ, v_x, v_r, v_θ, and e_t are the density, axial velocity, radial velocity, tangential velocity, and the total internal energy, respectively (all in the absolute frame).

Figure 2-7 shows the log of the residual convergence criterion plotted against iteration number for a simulation in which the inlet axial velocity profile is specified. The residual is a measure of the magnitude of the time derivatives in the equations of motion. It appears to be dropping over the first several thousand iterations. However, it can then be seen to increase and then decrease over a period of a few thousand iterations. The convergence history indicates that a disturbance was propagating through the flow field over a period of a few thousand iterations.

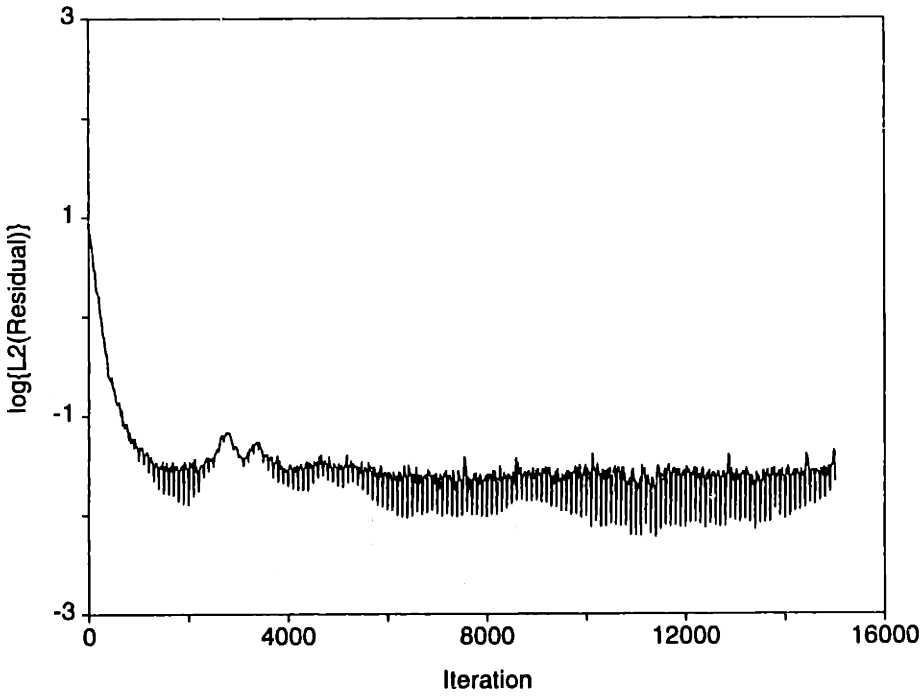

Figure 2-7: log of L2 norm of residual vs. iteration number for computation with fixed inlet velocity profile

Figure 2-8 shows this oscillatory behavior more clearly. The number of grid nodes having negative axial velocity is plotted against iteration number. This quantity should level off as the iteration count increases. However, the variation in the number of negative axial velocity points over a period of a few thousand iterations is a significant fraction (roughly 25%) of the total number of such points.

Figure 2-9 shows C_{P_t} distribution at the trailing edge plane for solutions at (a) 11000 and (b) 13000 iterations. The main difference in the flow fields occurs near the suction surface in the lower half of the blade span. The change in blockage, a quantity of primary interest, is evident from the C_{P_t} contours.

The convergence behavior for a computation with fixed inlet total pressure is noticably different. Figure 2-10 and 2-11 show convergence histories for such a computation in terms of the L2 norm of the residual and the number of negative axial velocity points, respectively. The fixed inlet total pressure computations were obtained by Celestina (1992). Both indicators of convergence show a more asymptotic trend with increasing iteration number. The oscillations in number of negative axial

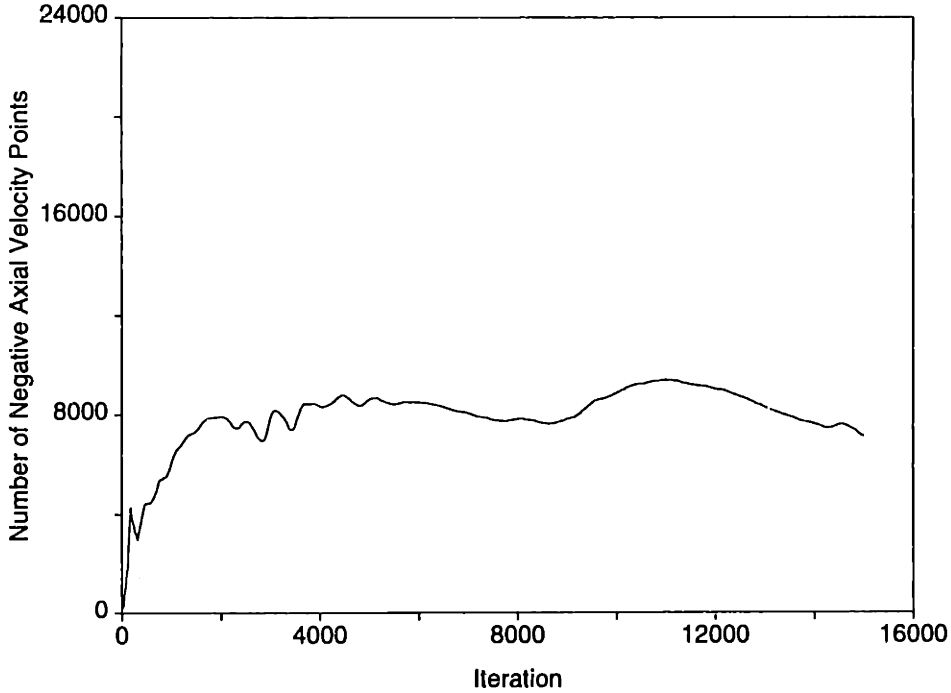

Figure 2-8: Number of negative axial velocity points vs. iteration number for computation with fixed inlet velocity profile

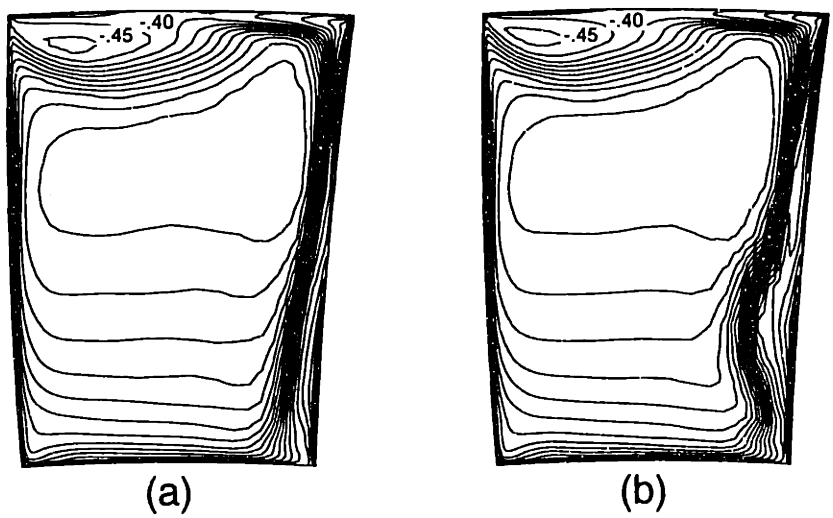

Figure 2-9: C_{P_t} at 100% chord for computation with fixed inlet velocity profile at (a) 11000 iterations and (b) 13000 iterations

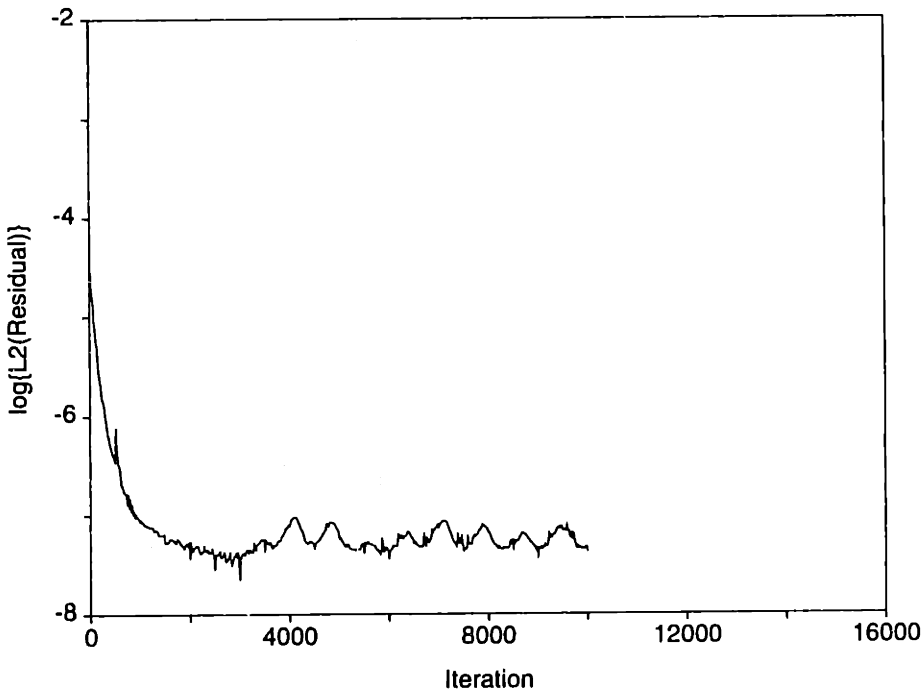

Figure 2-10: log of L2 norm of residual vs. iteration number for computation with fixed inlet total pressure profile

velocity points are roughly 5% of the total number of such points as compared to 25% for the fixed inlet axial velocity condition. Also, there was little change in the relative total pressure distribution over a period of a few thousand iterations.

The difference in scales for the L2 norm of the residual between Figures 2-7 and 2-10 are due to difference in normalization of the residual. The important features of these plots are how many orders of magnitude the residual decreases and the magnitude and period of the oscillations.

Dawes (1992) pointed out that the fluctuations in the solution with increasing iteration number should be expected if the inlet velocity is specified. A boundary of fixed velocity represents a reflective boundary condition. If a disturbance with a velocity increment δu meets a fixed velocity boundary, a wave must be reflected with a velocity increment $-\delta u$ in order to maintain a constant velocity. While fixing the total pressure instead does not eliminate reflection of waves at the boundary, both pressure and velocity at the boundary are allowed to change and this damps out some of the oscillation.

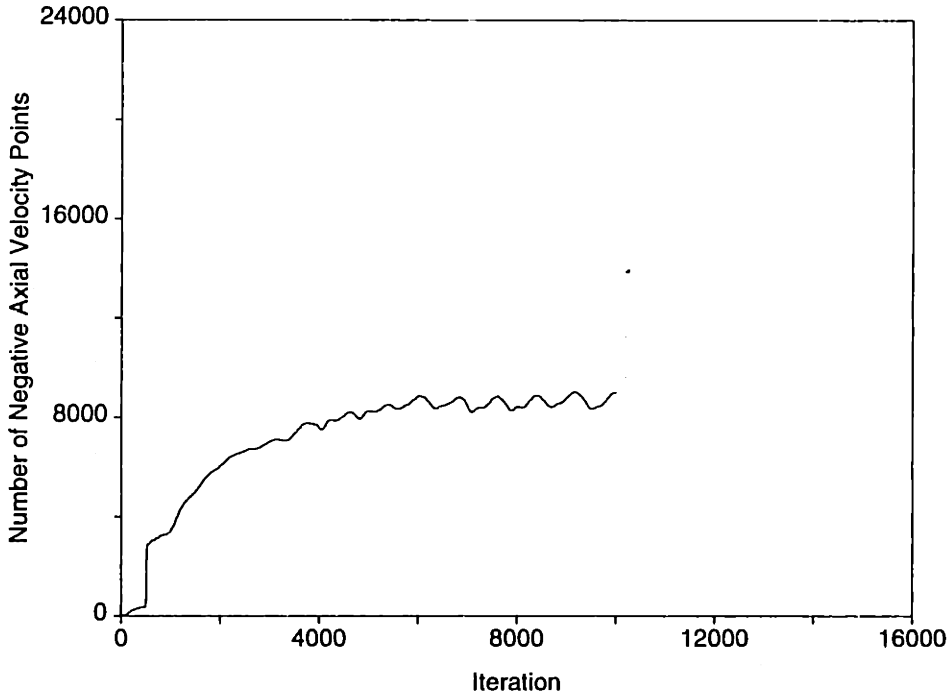

Figure 2-11: Number of negative axial velocity points vs. iteration number for computation with fixed inlet total pressure profile

Specifying the inlet velocity profile made it difficult to obtain a converged solution within reasonable computer run-times for the low speed rotor. Hence, the fixed mass flow inlet boundary condition was not used for the low speed rotor results presented in the remainder of this work. However, the computations with the stator geometry exhibited asymptotic convergence even with the fixed mass flow boundary condition, so that fixed exit mass flow was used for the stator.

2.4.5 Clearance modeling

One method of modeling the tip clearance in the computations is to place a grid in the clearance space. The Navier-Stokes code used in this work was written to compute the flow field over a single H-type grid. Some grid lines which run radially between the hub and the tip are thus required to bend abruptly to extend into the clearance space. This type of clearance modeling was employed by Crook et al. (1993) and will be called the gridded clearance model.

Figure 2-12 shows a constant axial index grid plane at 50% chord for a low speed

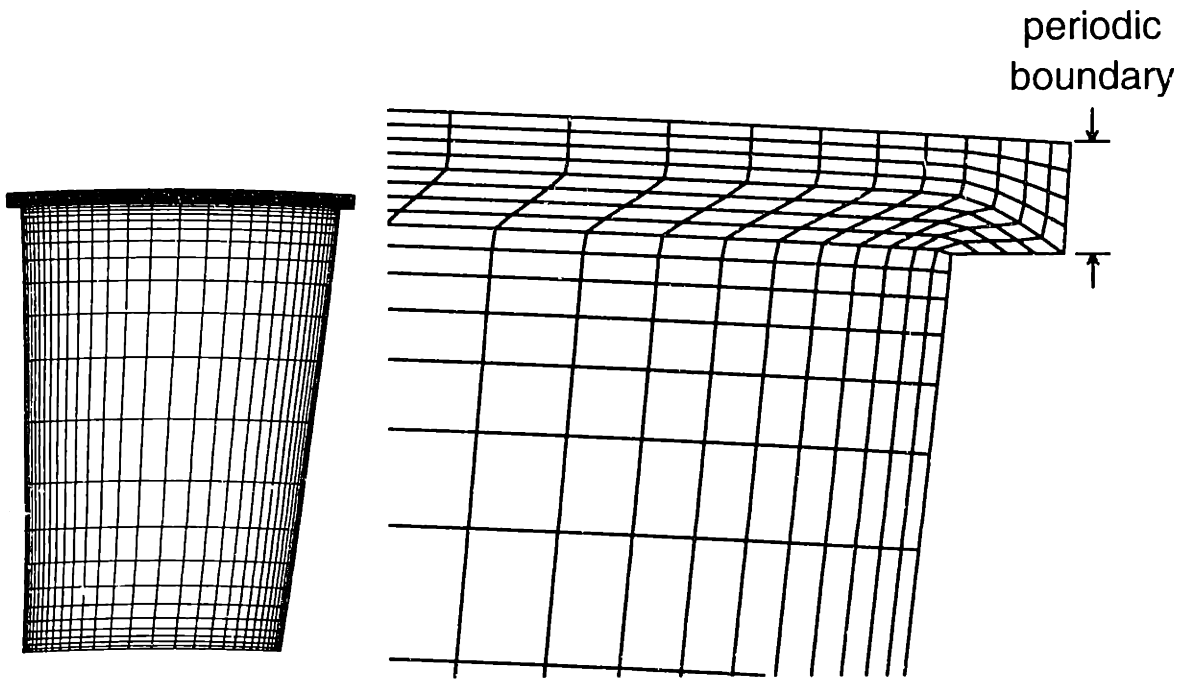

Figure 2-12: Axial plane at 50% chord of low speed rotor grid with gridded clearance model

rotor computation for which the gridded clearance model was used. Four cells span the periodic boundary halfway between the pressure and suction sides of the clearance space from tip to casing. The grid lines which run radially from hub to tip along the blade have a slope discontinuity at the blade tip and there is considerable grid skew.

The crossflow velocity vectors near the entrance to the clearance gap that result from this type of clearance model are shown in Figure 2-13. The vectors are viewed along the stagger. The leakage flow would be expected to separate at the pressure side corner and form a vena contracta (Storer and Cumpsty, 1991). However, the velocity vectors close to the tip surface are similar in magnitude to those halfway between the tip and casing and no vena contracta is evident.

Based on results such as this, the gridded clearance model was judged to be unable to properly resolve the flow within the clearance space. An alternative model, suggested by Kirtley et al. (1990), was used. The blade surfaces are extended from the blade tip to the casing and the region from tip to casing is specified as periodic from pressure to suction side of the passage. Periodicity implies that flow conditions at a node with a given axial and radial location on the pressure side of the passage are

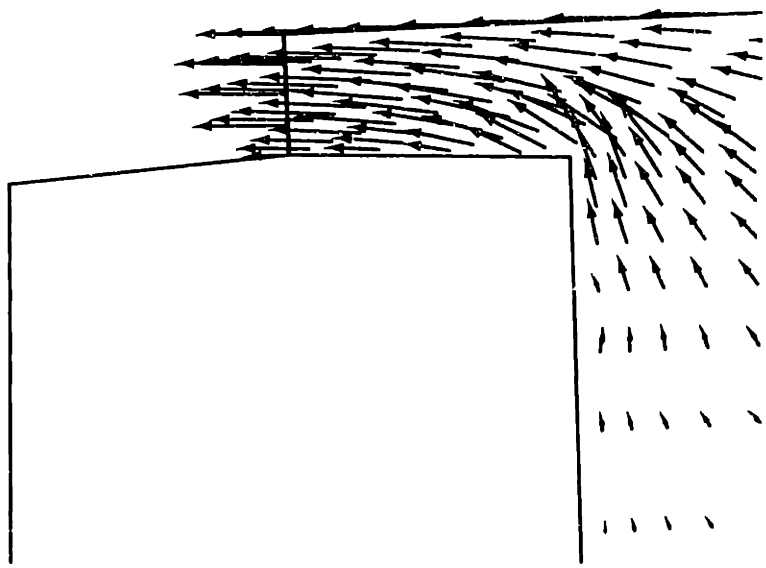

Figure 2-13: Crossflow velocity vectors entering clearance with gridded clearance model

the same as the flow conditions at the node with the same axial and radial location on the suction side of the passage. This will be called the periodic blade clearance model.

Figure 2-14 shows the constant axial index grid plane at 50% chord for a low speed rotor computation for which the periodic blade clearance model was used. As in the gridded clearance example, four cells span the periodic boundary. In this case, however, there is no change in slope of the grid lines from tip to casing. This results in a nearly orthogonal grid, thereby reducing the occurrence of numerical errors. The flow in the clearance space is not modeled. However, experimental investigations imply that compressor blades are generally thin enough such that the details of the flow in the clearance space do not play an important role in the development of the flow in the passage. For example, Storer and Cumpsty (1991) obtained good agreement between Navier-Stokes computations and experiment by narrowing the blade tip to a point with no attempt to model the flow within the clearance space.

Since the cleararance model used in the computations does not include the flow within the clearance space, the question arises as to what physical clearance corre-

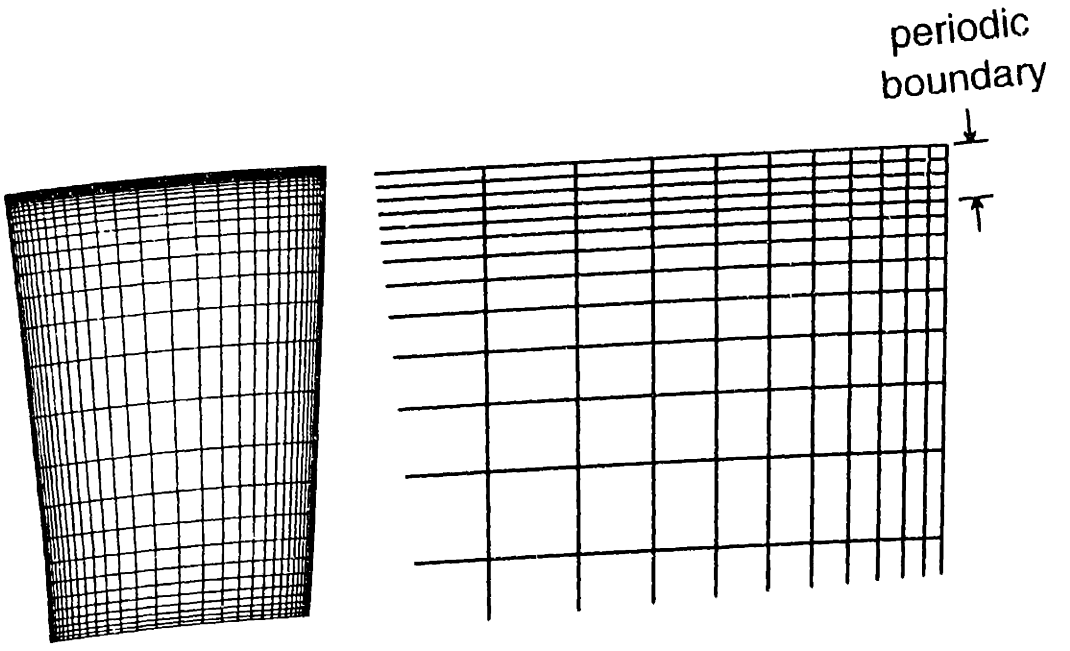

Figure 2-14: Axial plane at 50% chord of low speed rotor grid with periodic blade clearance model

sponds to a specified computational clearance. Thus, the effective clearance corresponding to the periodic blade clearance model is determined below.

Storer and Cumpsty (1991) calculated the discharge coefficient associated with the clearance using the equation

$$C_D = \frac{\dot{m}_{clr}}{\int_{LE}^{TE} \rho v_{n,i} \tau dl}, \tag{2.1}$$

where $\dot{m}_{clr}$ is the clearance mass flow rate, ρ is the fluid density, $v_{n,i}$ is the ideal leakage velocity normal to the blade, τ is the clearance height, and dl is the elemental chordwise length along the blade. The limits LE and TE designate the leading and trailing edge of the blade, respectively. The denominator in Equation 2.1 thus represents the ideal leakage mass flow for the clearance area.

Using Rains' (1953) model Storer and Cumpsty defined $v_{n,i}$ as

$$v_{n,i} = \sqrt{\frac{2(P_p - P_s)}{\rho}}. \tag{2.2}$$

The subscripts p and s refer to locations on the pressure and suction sides of the blade at a given axial station outside the influence of streamline curvature associated with the leakage flow.

Using Equations 2.1 and 2.2 Storer and Cumpsty (1991) obtained values for C_D of roughly 0.8, the departure from unity being due to the formation of a vena contracta within the clearance space. In the present low speed stator and rotor computations values for C_D were 0.6 to 0.7, in close agreement with the theoretical value for a sharp-edged orifice. The radial location used for p and s was 2τ inboard of the tip, far enough from the leakage flow to be outside the pressure variations associated with streamline curvature.

The agreement of the leakage distribution obtained using the blade pressure difference and discharge coefficient and leakage distribution obtained using the clearance velocity is shown in Figure 2-15 for the 3.0% clearance low speed rotor computation with $C_x/U = 0.42$. The solid curve represents the leakage distribution (as a percent of $\rho C_x c$) obtained from the Navier-Stokes clearance velocity plotted against percent chord location along the clearance. The dashed curve represents the leakage distribution obtained by using the ideal leakage velocity of Equation 2.2 and multiplied by C_D.

Clearance discharge coefficients near the theoretical sharp-edged orifice value (of 0.61) are obtained with the periodic blade clearance model because this model corresponds to assuming that the blades are infinitesimally thin at the tip, as illustrated in Figure 2-16. There is no clearance space in which the vena contracta can form, but a vena contracta does form within the passage near the clearance exit boundary. The vena contracta is evident in Figure 2-17 which shows C_P in a portion of the crossflow plane intersecting 50% chord on the suction surface for the 3.0% clearance low speed rotor with $C_x/U = 0.42$. There is a radial gradient in static presssure from the suction surface corner of the blade tip to the endwall.

The discharge coefficients obtained for the low speed Navier-Stokes computations

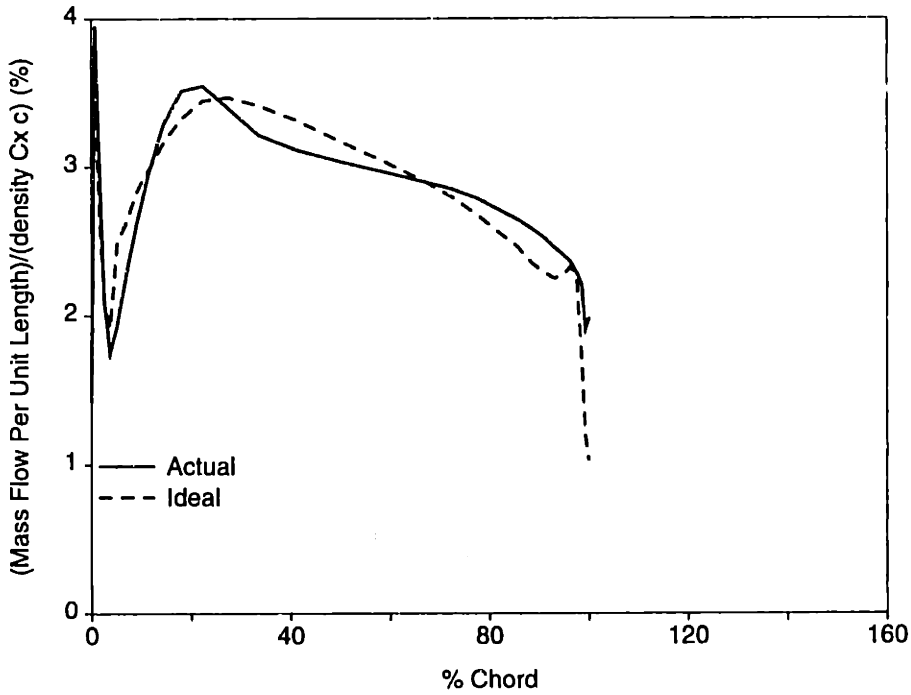

Figure 2-15: Actual and ideal leakage flow distributions for 3.0% clearance low speed rotor with $C_x/U = 0.42$

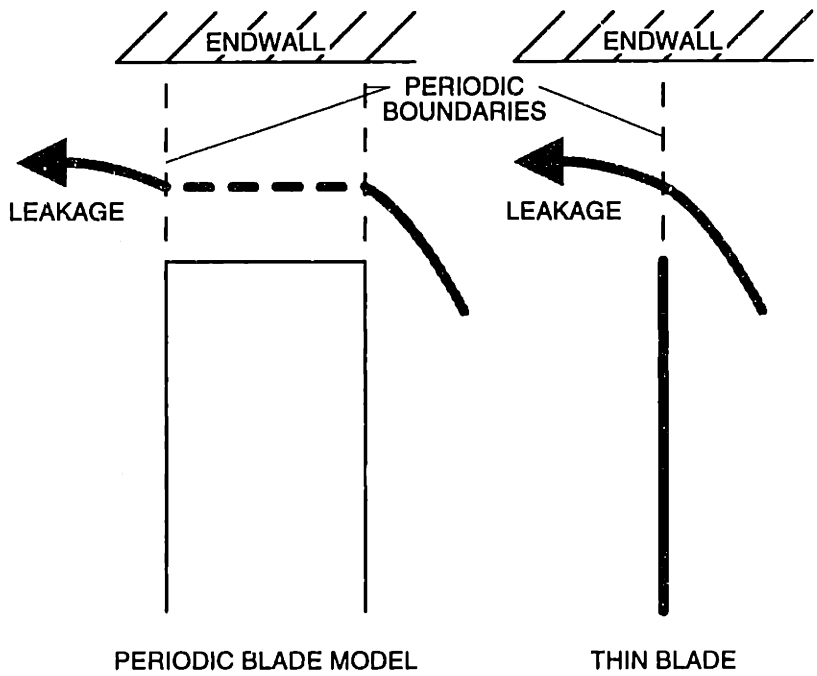

Figure 2-16: Illustration of periodic blade clearance model and thin blade approximation

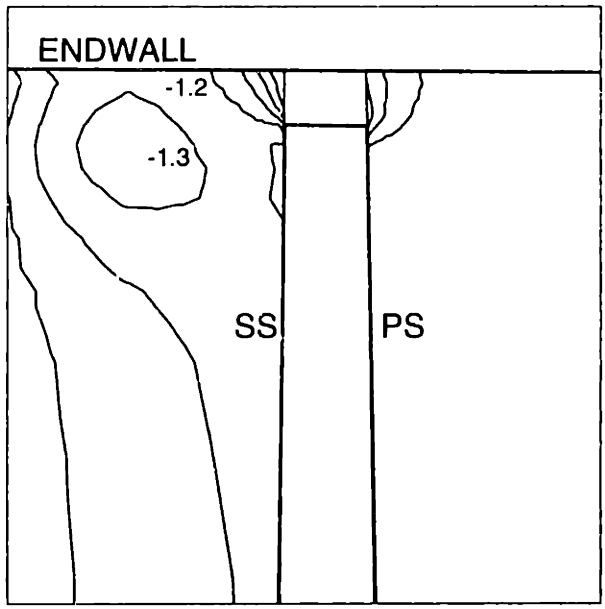

Figure 2-17: C_P near tip in crossflow plane intersecting 50% chord on suction surface for 3.0% clearance low speed rotor with $C_x/U = 0.42$; SS and PS denote suction and pressure surfaces, respectively

are within 25% of the experimental values obtained by Storer and Cumpsty (1991). Thus, the clearance height used in the periodic blade clearance model corresponds closely to the physical clearance height. To match physical clearance the computational clearance could then be specified to be 25% greater than the physical clearance.

For the Rotor 67 transonic fan Adamczyk et al. (1993) used a computational clearance which was less (one-half of) the actual clearance. This was done to match the computed peak pressure rise with experiment for a clearance of 0.5% of chord. Simulating half the clearance height may have produced better agreement with experiment than the full height, but this may be primarily due to the minor role of leakage for such a tight clearance. Based on the values of C_D obtained for the computations and the experimental values reported by Storer and Cumpsty (1991) this value appears too low.

2.4.6 Turbulence modeling

One of the most uncertain aspects of the computational model involves specification of the turbulent viscosity. The Reynolds-averaged Navier-Stokes solver used in this investigation employs the Baldwin-Lomax model which is appropriate for wall bounded flows. The flow features of primary interest are near the endwall, so using the Baldwin-Lomax model has some justification, but the Baldwin-Lomax model is tailored for boundary layers and wall jets, not three-dimensional vortical flows. Thus, the ability of the model to produce roughly the correct values of turbulent viscosity in this region needs to be assessed.

O'Sullivan (1993) examined the dependence of turbulent viscosity on flow Reynolds number for a unidirectional shear layer with a velocity ratio of approximately 0.5. The turbulent viscosity was a function of flow Reynolds number in which the characteristic length was distance downstream from the unmixed location. For a Reynolds number of 3.5×10^5, the turbulent viscosity was calculated to be 100 times the laminar viscosity.

The shear layer formed as a result of the leakage flow in the passage is not unidirectional. Also, the ratio of velocity magnitudes across the shear layer is essentially unity rather than 0.5. However, the ratio of the passage velocity to the leakage velocity resolved into the passage flow direction is roughly 0.5. Thus, the results reported by O'Sullivan (1993) should be representative of the endwall region. In the vortical region at the blade passage trailing edge of the computed flow field the turbulent viscosity calculated by the Navier-Stokes code was two to three orders of magnitude greater than the laminar viscosity. Given that the experimental Reynolds number was 3.5×10^5, the computational results are consistent with the results for a two-dimensional shear layer.

Another method to examine the validity of the turbulence model is to compare flow features which depend on the turbulence model with experimental results. The effect of the turbulence model on the clearance vortex is appropriate to examine since

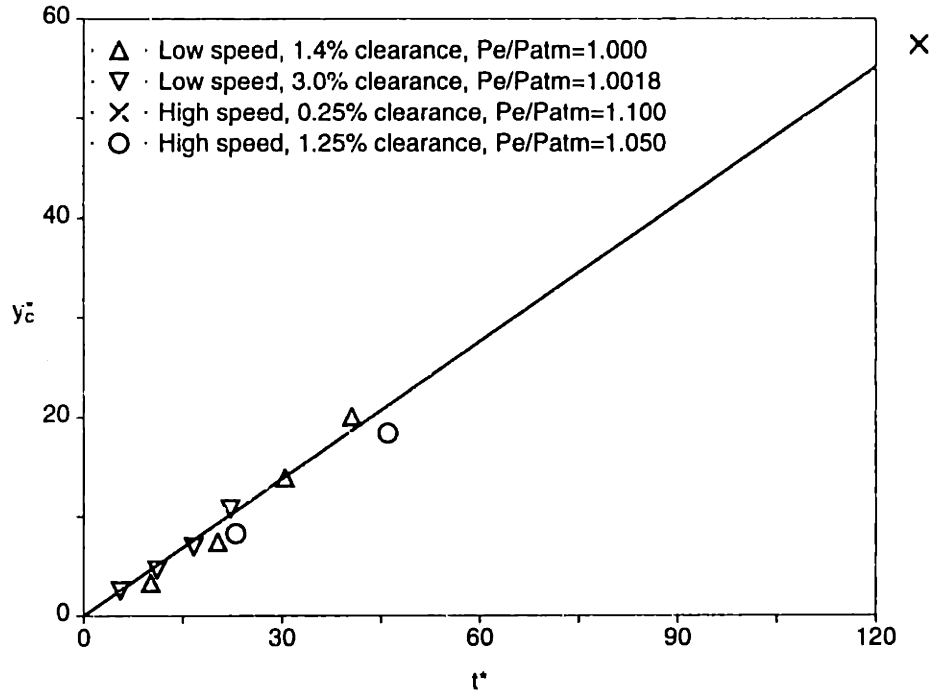

Figure 2-18: Predicted vortex trajectories for Navier-Stokes computations and theory of Chen et al. (1991)

Brookfield (1993) found that its trajectory depended on the turbulence and it is the the primary endwall flow structure of interest.

Clearance vortex trajectories for several Navier-Stokes computations are plotted in terms of the normalized coordinates of Chen et al. (1993) in Figure 2-18. The abscissa is the non-dimensional similarity parameter corresponding to streamwise distance, t^*, and the ordinate is the non-dimensional distance of the vortex center from the suction surface, y_c^*. Both distances are normalized by the clearance height. The midspan velocity triangles were used to calcuate t^*. The line indicates the theory of Chen et al. (1991) which was found to be in good agreement with a large array of compressor data. The computations are in good agreement with theory.

A computation was carried out in which the turbulent viscosity obtained by the turbulence model was multiplied by a factor of 10. The mass averaged loss over the clearance-related defect region at the trailing edge plane increased by roughly 15%, while the blockage (defined in Chapter 4) decreased by 50%.

The effect of turbulent viscosity on endwall flow field structure is illustrated in

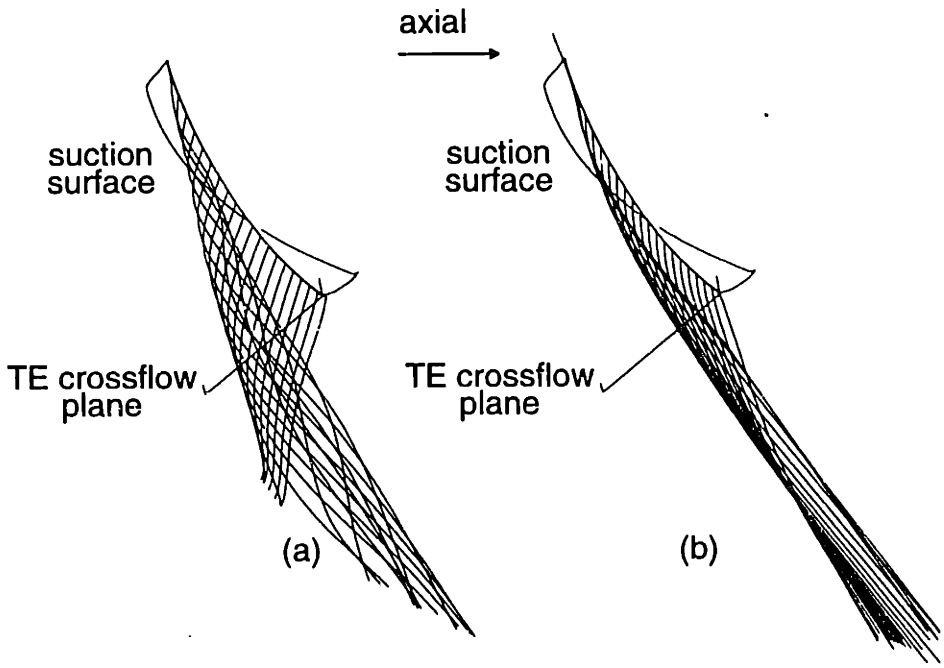

Figure 2-19: Vortex streamlines obtained using (a) Baldwin-Lomax turbulence model as coded in the Navier-Stokes solver and (b) turbulent viscosity increased by a factor of 10

Figure 2-19 which shows streamlines originating near the blade tip for (a) the turbulent viscosity values calculated by the model and (b) the ten-times increased turbulent viscosity computation. The blade suction surface and axial direction are indicated, as is a crossflow plane at the trailing edge of the passage. The intersection of the vortex with the crossflow plane indicates the distance of the vortex from the suction surface. The clearance vortex in the increased turbulence solution is less helical and closer to the suction surface.

Figure 2-20 shows vortex trajectories in terms of the theory of Chen et al. (1991). The trajectories obtained using the turbulence model with the baseline and fine grids used in the grid study (square and triangle symbols, respectively) are in good agreement with the theory. The trajectory obtained with the ten-times increased turbulent viscosity (indicated by the circle symbol) is different from the theory and experimental data by more than a factor of two. This result indicates that turbulent viscosity of the right order of magnitude is required to obtain the correct vortex trajectory. The Baldwin-Lomax model implemented in the code thus does yield the correct order of

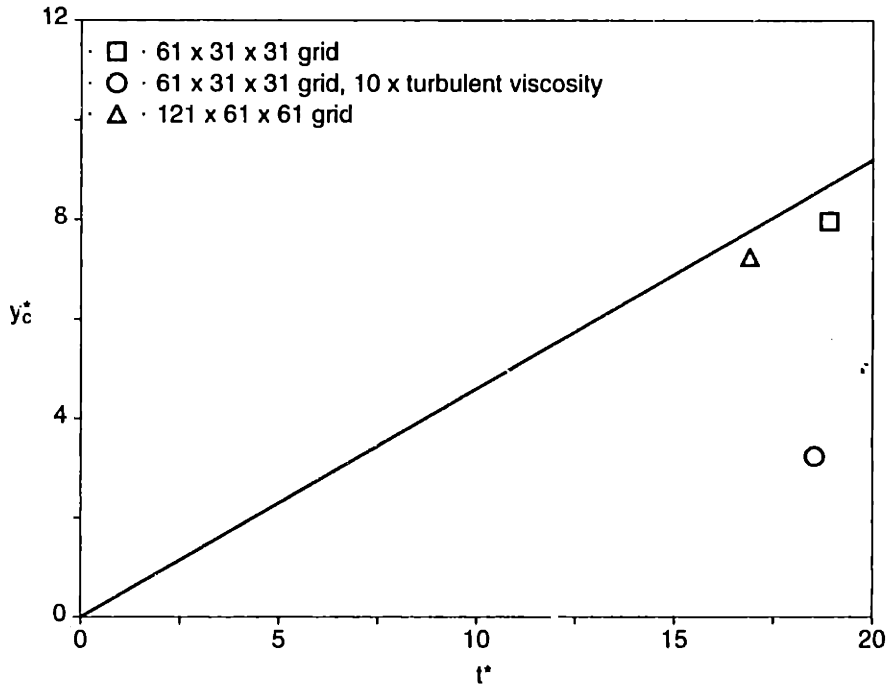

Figure 2-20: Predicted vortex trajectories for Navier-Stokes computations with Baldwin-Lomax turbulence model and increased turbulent viscosity compared with theory of Chen et al. (1991)

magnitude for turbulent viscosity.

2.5 Conclusions

The issues which were examined to assess the utility of the computations to examine tip clearance flows are summarized below.

A grid study was performed in order to verify that the flow fields subsequently obtained in the investigation were grid independent. Thirty cells in each curvilinear direction within the passage with stretching ratios of 1.2 to 1.3 were found to be sufficient to capture the flow features, integral quantities, and viscous terms which are included in the equations. In the course of the grid study a sensitivity to cell Reynolds number was found for the low speed computations. This problem was addressed by increasing the Reynolds number in the computations to be appropriate for the range of applicability of the computational code.

The importance of cell aspect ratio was demonstrated by the failure of the com-

putations to converge for an increased solidity blade row using a grid with the same dimensions as the original solidity blade row. Reducing the number of cells in the blade to blade direction resulted in computations which converged.

Because of the desirability of obtaining computed flow fields at operating near the peak of the compressor characteristic, running the computations with a fixed inlet velocity profile boundary condition was examined. Stator computations were obtained using this type of boundary conditon, but it was found that there is a potential for oscillations in the solution due reflections from the boundary when this condition was used. The rotor computations were thus carried out using a fixed total pressure profile inlet boundary condition.

A periodic blade clearance model was used in the computations. The computational clearance using this model was shown to correspond to roughly the same physical clearance height.

The effect of changes in the turbulence model was examined by increasing the calculated turbulent viscosity by a factor of 10. The clearance vortex trajectory was shown to be strongly affected by this change. The vortex trajectories predicted by the turbulence model employed in the computations, however, were in good agreement with experimental data, indicating that the turbulent viscosity values that are used are of the right order of magnitude.

As a result of addressing the above issues, the effects of clearance obtained in the investigation can be regarded as representative of physical machines. While the flow solver used in this investigation is not suitable to examine all flow phenomena associated with an axial compressor blade passage (for example, boundary layer separation), it has been shown to be capable of capturing the flow phenomena associated with tip clearance and it is useful for addressing the research questions raised in Section 1.4. In addition to clarifying the conditions under which the computations should be used in the present work, the issues raised in this chapter serve to alert other researchers to the limitations associated with numerical investigations of fluid

dynamic phenomena.

Chapter 3

Quantification of Blockage

3.1 Introduction

The term "blockage" is widely used in discussions regarding axial compressors. It generally refers to the reduction in effective freestream or core flow area due to local velocity defects, analagous to the displacement thickness associated with boundary layers. Blockage is important because the effective flow area determines the pressure rise. Tip clearance has been shown to have a strong effect on stalling pressure rise (Smith, 1970 and Koch, 1981) and it is reasonable to link the growth of clearance-related blockage to stall.

In spite of its importance assessments of blockage have, for the most part, been limited to qualitative descriptions regarding the size and severity of the apparent nonuniformity or velocity defect present in the flow, e.g., Smith and Cumpsty (1984) and Crook et al. (1993). Some techniques to quantify blockage or displacement thickness for axial compressors have been suggested, e.g., Smith (1970) and Dring (1984), but none have linked the nonuniformity in the local defect region to the core region velocity (and thus, the pressure rise) in a rigorous fluid dynamic manner.

To identify trends in clearance-related blockage as well as to help in understanding its mechanisms, a quantitative assessment of blockage is required. In this chapter, we

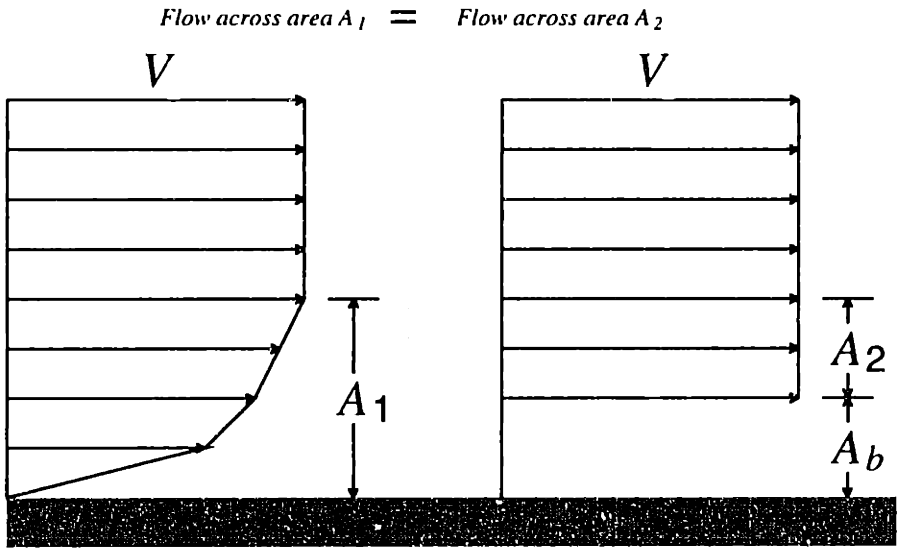

Figure 3-1: Concept of blockage

define a method for quantifying blockage in axial compressors and apply the method to the computed flow fields of the low speed rotor and the transonic fan. The resulting blockage values are used to illustrate the role of clearance in blockage growth.

3.2 Preparatory Remarks

3.2.1 Importance of blockage

Before addressing blockage in a three-dimensional flow, we examine a simpler situation to see why blockage is useful. Consider a unidirectional incompressible flow with a uniform core and a region of reduced velocity (e.g., a boundary layer). The actual flow is translated into equivalent areas of core flow and blocked area (zero flow) as illustrated in Figure 3-1. For a given mass flow and total area, an increase in blocked area results in an increase in core velocity. The blockage concept thus allows the flow to be characterized in terms of an associated effective area. If the core region is inviscid the pressure rise is directly related to the change in core region velocity, and hence the blockage, via Bernoulli's equation.

In a three-dimensional flow the same idea holds, at least conceptually. However, in such a flow a reduction in effective throughflow area can result from variations in flow direction as well as velocity magnitude. Increases in relative flow angle (measured from the axial direction), reduce the effective flow area.

To see the impact of changes in effective flow area on rotor pressure rise capability, consider the consequences of assuming that the exit flow is uniform and the angle does not change with clearance. Under these conditions two flow fields with the same mass flow would have the same relative exit velocity. For two such flow fields, denoted by subscripts 1 and 2, the difference in exit static pressure would equal the difference in exit relative total pressure. That is,

$$P_2 - P_1 = P_{t,2} - P_{t,1},$$

where P and P_t are the exit values of static pressure and relative total pressure, respectively. Adding the relative total pressure loss to the pressure rise for flows corresponding to different clearances would collapse the pressure rise versus mass flow characteristics.

To examine the applicability of such a picture, Figure 3-2 shows two pairs of computed low speed rotor pressure rise characteristics. The solid curves represent pressure rise versus flow coefficient characteristics. Square and circle symbols represent 1.4 and 3.0% clearance, respectively. The dashed curves represent the sum of the pressure rise and relative total pressure loss for each flow field. The pressure rise and total pressure loss were obtained by calculating mass averages of the static and relative total pressures upstream of the blade row and at the passage exit.[1] The dashed curves are closer together than the solid curves, but the difference between

[1]The area average might be more appropriate to use for static pressure since this comes into in the momentum equation for a control volume for the passage. Mass averages were used here so that the averaging procedure would be the same as for the relative total pressure. The static pressure is fairly uniform at passage exit (see Figure 4-5) so there is little difference between the area and mass averages anyway.

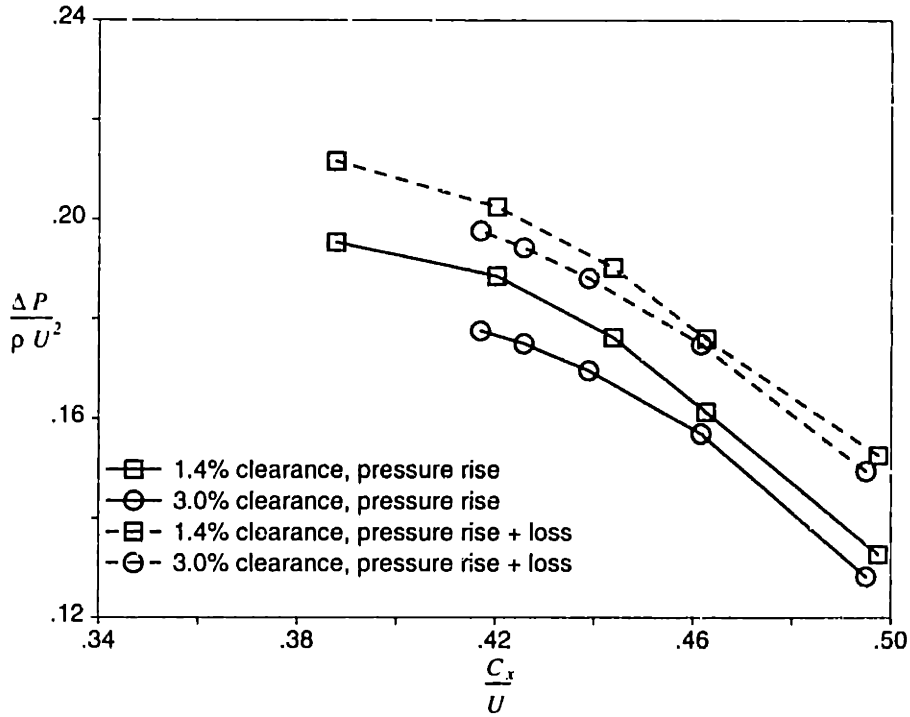

Figure 3-2: Effect of adding passage loss to pressure rise for low speed rotor

the dashed curves is still a considerable fraction of the difference between the original characteristics (solid curves).

Because the characteristics do not collapse when the loss is added to the pressure rise, differences in effective exit flow area must also be important in setting the differences between the two characteristics. Further, the slopes of the pressure rise characteristics change little with the addition of the relative total pressure loss, indicating that loss changes little with loading compared to the pressure rise. Thus, the reduction in the magnitude of the slope of each characteristic with reduced flow coefficient is due to decreasing effective area. The assumptions of uniform flow and constant relative exit angle are thus inappropriate for the purpose of explaining the limitations on pressure rise due to clearance and loading. Also, changes in deviation (with clearance) were found to have a small effect on pressure rise compared to the differences shown, so the distance between the dashed characteristics in Figure 3-2 is mainly due to blockage.

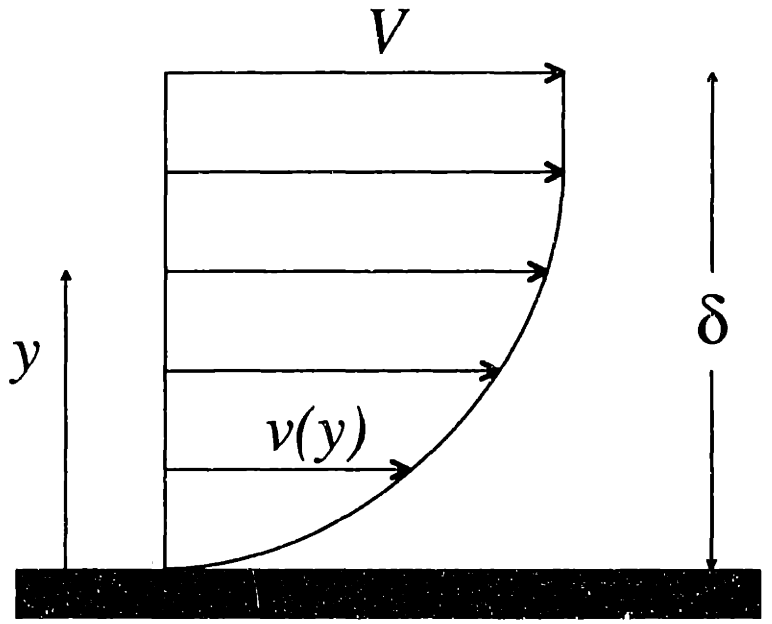

Figure 3-3: Definitions required to calculate displacement thickness

3.2.2 Aspects of blockage in axial compressors

For a two-dimensional boundary layer the expression for displacement thickness is given as

$$\delta^* = \int_0^\delta \left(1 - \frac{v(y)}{V}\right) dy, \tag{3.1}$$

where the variables are as indicated in Figure 3-3.

An equation of similar form is sought as a means to calculate blockage for a more general flow. In a turbomachine the flow is three-dimensional and the freestream or, core region, is nonuniform. Two questions thus arise: (1) What component of velocity (corresponding to $v(y)$) should one use? and (2) How does one choose the edge of the defect?

Although the flow in axial compressors is complex, some features are shared by many situations. First, the freestream or core flow has an identifiable direction which may be called the throughflow or *mainflow* direction. We will see that this mainflow direction can be used to select the velocity component to use in the blockage definition.

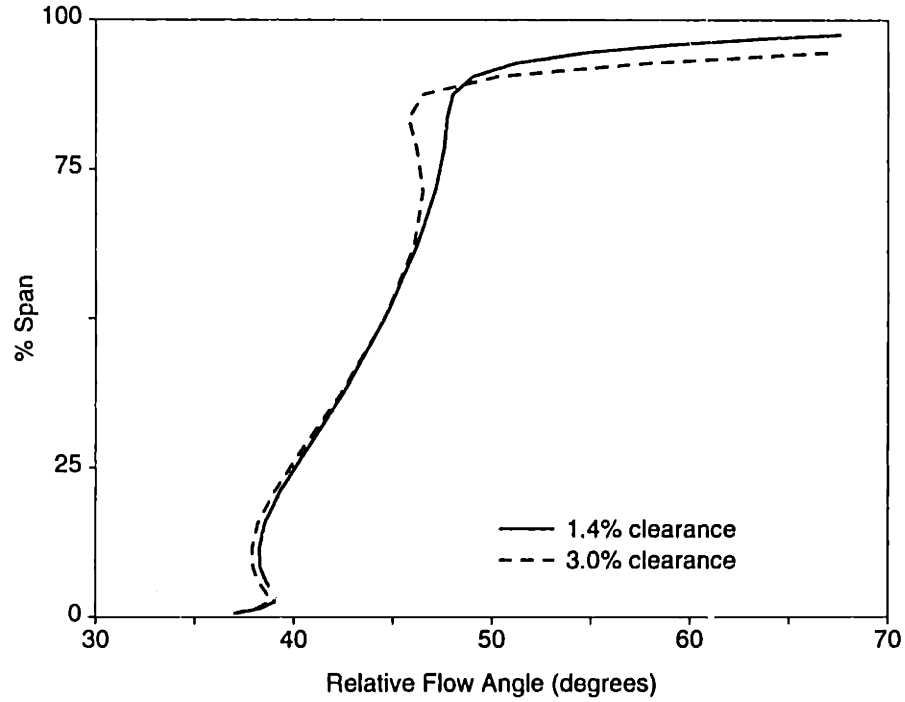

Figure 3-4: Relative exit flow angle at trailing edge midpitch location at $C_x/U = 0.42$ for 1.4 and 3.0% clearance

Second, although the core flow may be nonuniform, it is still useful to distinguish between this region and that existing near the walls or blades because the gradients in the latter are significantly greater than those in the former. This aspect will be used to identify the edge of the defect region.

A further attribute of the core region is that increases in the blockage which accompany increased clearance and loading produce increases in core velocity, but little change in core flow angle. This is illustrated in Figure 3-4 which shows radial profiles of relative exit flow angle at the midpitch and trailing edge location for low speed rotor flow fields for two clearance and with $C_x/U = 0.42$. The solid and dashed curves correspond to 1.4 and 3.0% clearance, respectively. If the core angle variation is not large, minor changes in core flow angle with blockage imply that the average core velocity reflects changes in blockage.

3.3 Proposed Blockage Definition

3.3.1 Appropriate velocity component

To determine which velocity component one should use to quantify blockage, we first consider a two-dimensional profile which is unidirectional with a uniform core. Successive levels of complexity will then be discussed leading up to the axial compressor flow field.

For the two-dimensional profile shown in Figure 3-5a, the displacement thickness associated with the defect regions, d_1 and d_2, can be calculated using Equation 3.1 written in terms of the variables indicated in Figure 3-5a:

$$\begin{aligned} \delta^* &= \delta_1^* + \delta_2^* \\ &= \sum_{n=1}^{2} \int_{d_n} \left(1 - \frac{v(y)}{V}\right) dy. \end{aligned}$$

where $v(y)$ describes the velocity over the entire profile and V is the core velocity. There is only one velocity direction and no question about which velocity component to use.

Figure 3-5b shows a velocity profile in which the defect regions are not unidirectional. The velocity resolved into the direction of the mainflow, v_m, is indicated by the dashed curve. The reduction in core flow area is quantified by integrating the velocity component in the core flow direction (i.e., v_m) over the defect regions. The resulting displacement thickness is greater than if the velocity magnitude were integrated over the defect regions. Thus,

$$\delta^* = \sum_{n=1}^{2} \int_{d_n} \left(1 - \frac{v_m(y)}{V}\right) dy.$$

Even if the flow angle in the core region is not uniform, it is often possible to define a mainflow direction. Figure 3-5c shows a flow angle profile indicated by the

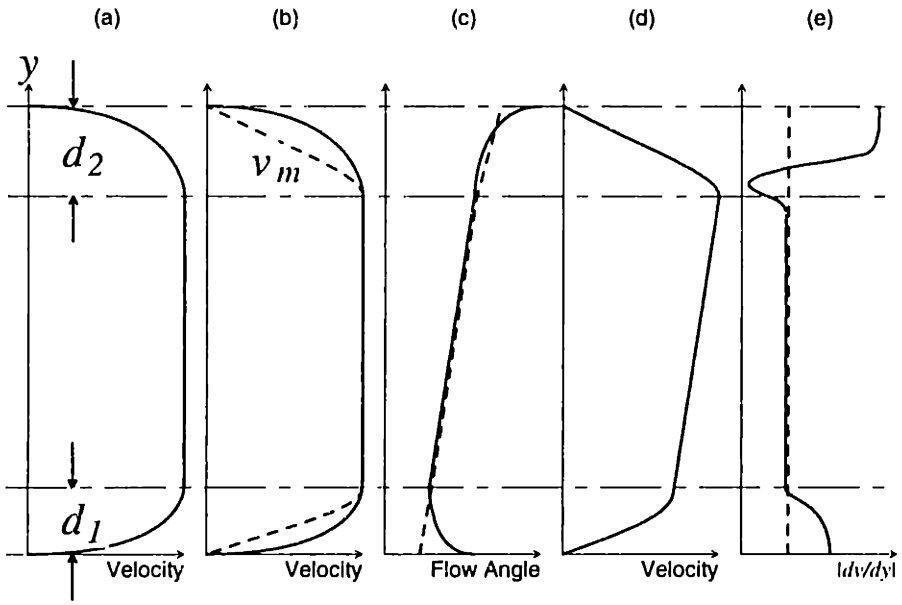

Figure 3-5: Profiles illustrating basis for appropriate velocity component and edge criterion

solid curve. The dashed curve shows how the mainflow direction in the defect regions might be extrapolated. The mainflow direction in the core region can be defined for any radius even if the flow angle varies. Velocity components other than the mainflow component are regarded as crossflow. Note that differences in the extrapolation are likely to produce only minor changes in blocked area results because the velocity component used to calculate the blocked area varies with the cosine of the angle between the velocity vector and the mainflow direction. For example, a difference in mainflow angle of 10 degrees changes the mainflow velocity component by 1.5%

Generally, there is a variation in velocity magnitude in the core region, as shown in Figure 3-5d. In this case the displacement thickness associated with each defect region should be calculated using the core region velocity at the edge of each defect region which will be referred to as the edge velocity, V_e. The total displacement thickness associated with the two defect regions, allowing for crossflow in the defect

regions and nonuniformity in the core region, is

$$\delta^* = \sum_{n=1}^{2} \int_{d_n} \left(1 - \frac{v_m(y)}{V_{e_n}}\right) dy.$$

The subscript n in V_{e_n} indicates that the edge velocity corresponding to each defect region is obtained from the core region neighboring the defect region.

Density variations across the profiles of Figure 3-5 are incorporated in the same manner for compressible boundary layers. Instead of the velocity, the product of density and velocity is used:

$$\delta^* = \sum_{n=1}^{2} \int_{d_n} \left(1 - \frac{\rho v_m(y)}{\rho_{e_n} V_{e_n}}\right) dy$$

So far, the implications of crossflow, core nonuniformity, and density variations on displacement thickness have been discussed. To calculate a blocked area, the displacement thicknesses in a plane must be integrated. This integration step is discussed next.

Consider a straight rectangular duct shown in Figure 3-6. A defect region exists along the bottom wall, with the freestream, or core region, along the top surface. The x-axis is aligned in the mainflow direction, the y-axis is oriented vertically, and the z-axis cuts across the duct normal to the x and y axes. Three stations of constant y-coordinate are indicated on the top wall, labeled 1, 2, and 3. In general, there can be crossflow in the defect regions and the displacement thickness at each station would be calculated using the component velocity in the mainflow direction, x.

Stations 1 and 2 are in a plane normal to the mainflow direction. To calculate the blocked area in this plane, one would integrate the displacement thickness at each constant y-station over z. Thus, the blocked area in the plane containing stations 1 and 2 is

$$A_{b,12} = \int_z \delta^* dz$$

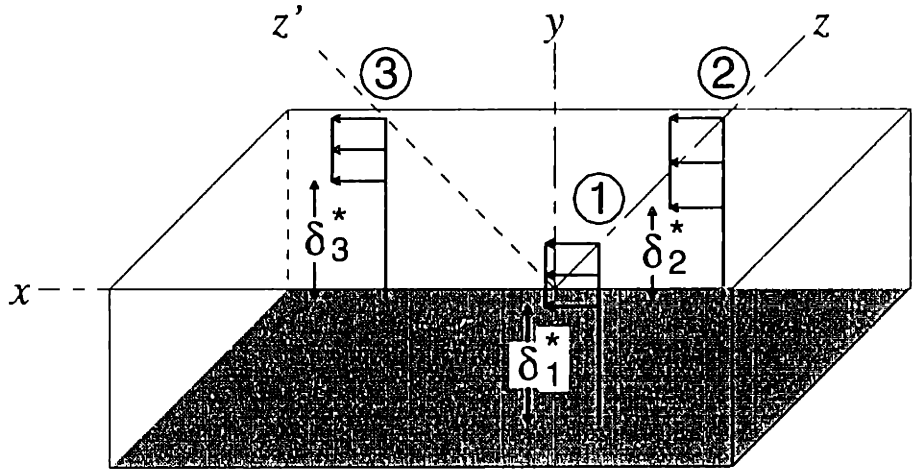

Figure 3-6: Integrating displacement thickness to get blocked area

$$= \int_z \int_y \left(1 - \frac{\rho v_m}{\rho_e V_e}\right) dydz$$
$$= \int_{A_{12}} \left(1 - \frac{\rho v_m}{\rho_e V_e}\right) dA,$$

where $v_m = v_x$ in this case.

Stations 1 and 3 are in a plane which is at an angle to the main flow. To calculate the blocked area in this plane, one would integrate the displacement thickness at each constant y-station in the z'-direction. The fact that the plane corresponding to stations 1 and 3 is not normal to the flow does not change how the displacement thickness at each constant y-station is evaluated — v_x is still the velocity component which is used. Thus, the blocked area in the plane containing stations 1 and 3 is

$$\begin{aligned} A_{b,13} &= \int_{z'} \delta^* dz' \\ &= \int_{z'} \int_y \left(1 - \frac{\rho v_m}{\rho_e V_e}\right) dydz' \\ &= \int_{A_{13}} \left(1 - \frac{\rho v_m}{\rho_e V_e}\right) dA. \end{aligned} \tag{3.2}$$

In summary, the displacement thickness at any station in the flow field is obtained by resolving the velocity in the defect region into the nearby core flow direction. The orientation of the plane in which one evaluates the blocked area has no bearing on which velocity component should be integrated.

3.3.2 Identifying the edge of the defect region

In determining the appropriate velocity component to use in a blockage definition, it was presumed that the extent of the defect region was known. It is also necessary to establish a criterion by which one identifies the edge of the defect region.

Consider the shear profile shown in Figure 3-5d. Although there is no region of uniform flow, the velocity defect regions due to the boundary layers are clear. The reason for this is that, when one visually distinguishes between the defect and core regions, one looks for a change in slope of the velocity profile. There is a substantial increase in the magnitude of the velocity gradient in the defect regions. In fact, in most flows in which it makes sense to distinguish between core and defect regions, the magnitude of the velocity gradient in the defect regions is much greater than in the core region, and this aspect is utilized here. A sketch of gradient magnitude, $|dv_m/dy|$, as a function of y for the velocity profile of Figure 3-5d is shown in Figure 3-5e, where the defect region corresponds to $|dv_m/dy|$ greater than the value indicated by the dashed line.

In a three-dimensional flow there are three components of the gradient of a scalar, not just one. Thus, one needs to be concerned about which components of the gradient should make up the gradient magnitude used to identify the defect region. For a unidirectional shear flow, the streamwise component of the velocity gradient does not provide any measure of the velocity nonuniformity at the streamwise station. Similarly, to identify the defect region in a plane in a three-dimensional flow, gradients in velocity *normal* to the plane are irrelevant if one is interested in identifying the defect region *in* that plane. The appropriate scalar to use to identify the edge of the

defect region is thus the magnitude calculated from the two components (i.e., the square root of the sum of the squares of the two components) of $\nabla[\rho v_m]$ which lie in the plane for which the blockage is to be obtained. If the blocked area is to be calculated in an axial (constant x) plane, the radial and tangential components of the gradient are used to obtain the gradient magnitude, written compactly as $|\nabla[\rho v_m]|_{r,\theta}$. Using r and θ to indicate radial and tangential components, respectively,

$$|\nabla[\rho v_m]|_{r,\theta} = \sqrt{(\nabla_r[\rho v_m])^2 + (\nabla_\theta[\rho v_m])^2}.$$

The gradient magnitude contour used to define the edge of the defect region depends on the gradient in the core region. Increased core region nonuniformity requires an increased gradient magnitude value to specify the edge. Choosing a nonzero gradient magnitude can result in some of the defect region near the defect edge being excluded from the remainder of the defect region. In Figure 3-5d there is a reduction in the gradient in the y-direction from the core region to the defect region at the top of the profile. As a result, the low-gradient portion of the defect region near the defect edge is omitted from the calculation of blockage. However, since the region near the core has the least contribution per unit area to the blockage, errors of this sort should be small.

An additional consideration relating to the use of the gradient magnitude concerns local minimums in velocity in the defect region. If such minimums occur the gradient magnitude near that location may be less than the value chosen to specify the edge. This may cause inaccuracies in a blockage calculation routine which uses the local gradient magnitude to find the edge values and as a toggle to select the area over which to integrate. One way to resolve the issue is to replace the gradient values at grid nodes in local minimum regions with values slightly greater than the gradient value used to specify the edge of the defect before passing the information to the routine which finds the edge values and performs the integration.

3.3.3 Summary of blockage definition development and the mathematical expression

The expression for blocked area is

$$A_b = \int_d \left(1 - \frac{\rho v_m}{\rho_e V_e}\right) dA. \tag{3.3}$$

The ability to evaluate this integral depends on two simplifying aspects that are typically present in axial compressors: (1) an identifiable mainflow direction, and (2) a substantially greater nonuniformity in the defect region than the core region. The mainflow direction in the defect region is determined by extrapolating the core region flow angle radial profile at midpitch. The edge criterion is based on the magnitude of the components of $\nabla[\rho v_m]$ which lie in the plane being considered. The gradient magnitude used as the edge criterion is selected to be the minimum value not present in the core region. The edge velocity and density (Ve and ρ_e, respectively) in the Equation 3.3 are the values along the edge nearest to dA.

3.4 Blockage Calculation Procedure

3.4.1 Outline

The steps in the blockage quantification method presented can be summarized as follows.

1. Acquire adequate flow data
2. Identify mainflow direction
3. Calculate $|\nabla[\rho v_m]|_{r,\theta}$ for cutoff function
4. Choose cutoff value which defines defect region
5. Reset any low cutoff function locations within defect region

6. Find edge locations and $\rho_e V_e$

7. Calculate $\rho v_m/(\rho_e V_e)$

8. Find set of dA corresponding to defect region

9. Numerically integrate blocked area

To illustrate the calculation of a blocked area for a compressible flow field with a nonuniform core region, the Rotor 67 transonic fan flow field will be used as an example. The clearance is 1.4% and the conditions are near the design. The total blocked area at the trailing edge station as well as the blocked area due to the clearance flow will be calculated.

3.4.2 Illustrative example

Step 1: Acquire adequate flow data

To calculate the blocked area in a plane of an axial compressor flow field using the definition given by Equation 3.3, the three-dimensional velocity field in the plane is required. The grid representing the discrete locations where the velocity is known must be sufficiently resolved so that the nonuniformity, density as well as velocity, associated with the defect region is captured. The grid used in the present example has 31 points from blade to blade with a stretching ratio of 1.2 and similar resolution in the radial direction.

Step 2: Identify mainflow direction

The radial distribution of tangential flow angle at the trailing edge midpitch location is shown as the solid curve in Figure 3-7. A curve fit used to specify the mainflow direction in the defect regions is indicated by the dashed curve. At each radial location there is a direction in which to resolve the velocity field in order to obtain the mainflow velocity field.

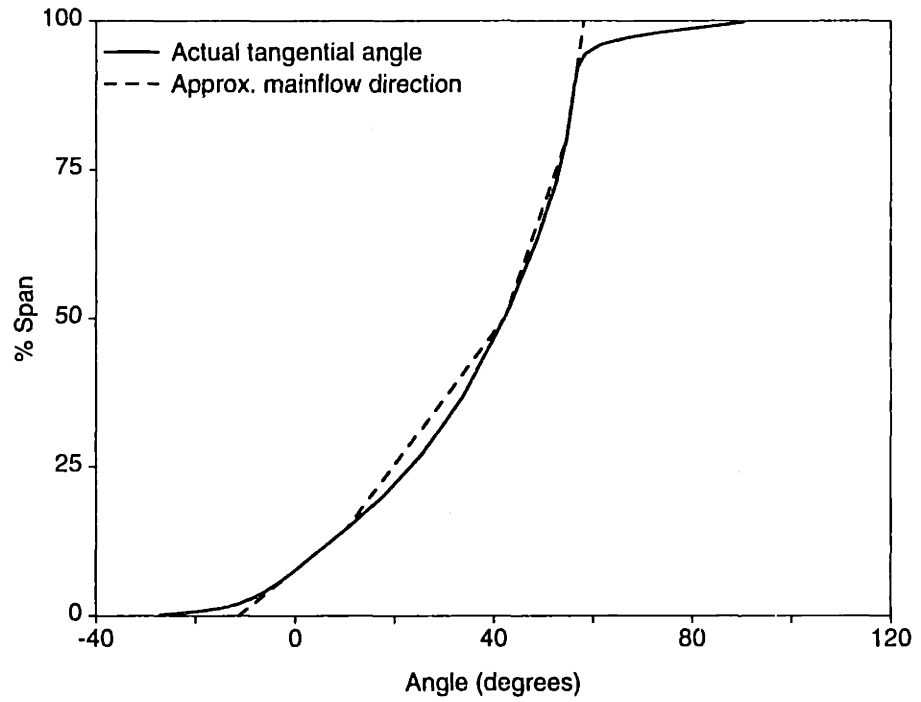

Figure 3-7: Radial profile of trailing edge midpitch flow angle for 1.25% clearance high speed fan at near-design loading

Step 3: Calculate $|\nabla[\rho v_m]|_{r,\theta}$ for cutoff function

Contours of the mainflow velocity component for this example are shown in Figure 3-8a. To identify the defect region a discrete approximation to $\nabla[\rho v_m]$ is first calculated over the grid. Then the magnitude of the vector formed by the two components of the gradient which lie in the surface is calculated. For a plane which is roughly axial, the magnitude of the radial and tangential components can be used. Contours of $|\nabla[\rho v_m]|_{r,\theta}$ normalized by $\rho_{av} C_x / c$ are shown in Figure 3-8b. Since this scalar will be used to specify the region over which the blocked area will be integrated, it is called the *cutoff function.*

Step 4: Choose cutoff value which defines defect region

Although there is a large velocity change in the core region, the magnitude of the core region gradient is nearly uniform compared to the magnitude of the gradient in the defect region. The core region roughly corresponds to the region where $|\nabla[\rho v_m]|_{r,\theta} / (\rho_{av} C_x / c) < 2$. A cutoff function value of 2.0 can thus be used to define the edge of the defect region. This value is be called the *cutoff*

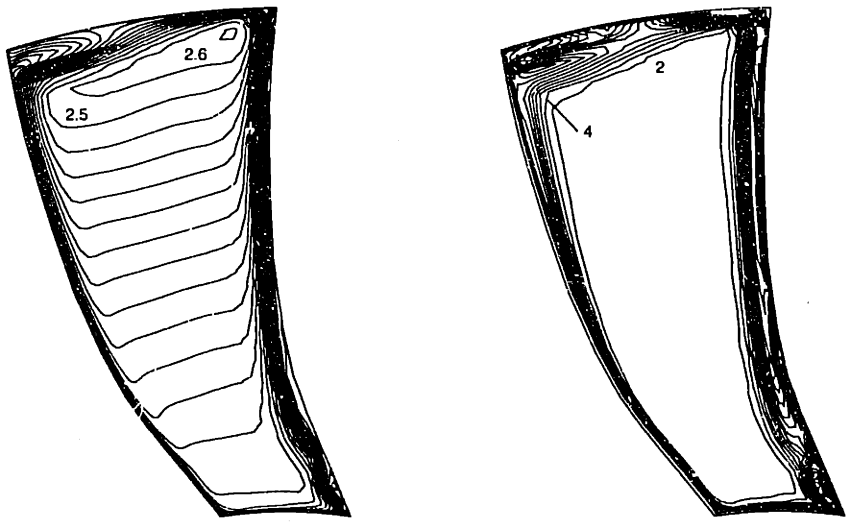

Figure 3-8: (a) $\rho v_m/(\rho_{av}C_x)$, and (b) $|\nabla[\rho v_m]|_{r,\theta}/(\rho_{av}C_x/c)$ at trailing edge for 1.25% clearance high speed fan at near-design loading

value.

Step 5: Reset any low cutoff function locations within defect region

The contour of the scalar $|\nabla[\rho v_m]|_{r,\theta}/(\rho_{av}C_x/c) = 2$ is shown in Figure 3-9a. The "islands" of low gradient magnitude within the defect region are eliminated by manually setting the cutoff function in these regions to a value slightly greater than 2, e.g., 2.1. This is important for two reasons: (1) the low gradient regions should be included in the blocked area calculation, and (2) ρv values along the cutoff function contour which lies within the defect region should not be included in the set of $\rho_e V_e$.

Step 6: Find edge locations and $\rho_e V_e$

A computer routine is used to interpolate locations on the grid where the cutoff function equals the cutoff value selected. These locations are shown for the present example in Figure 3-9b. The routine also stores the ρv corresponding to each location, which form the set of $\rho_e V_e$.

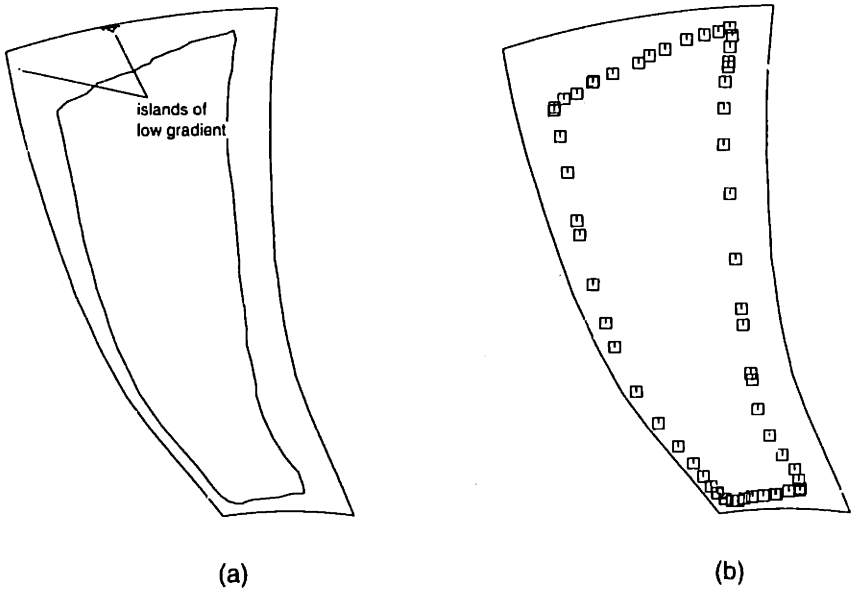

Figure 3-9: (a) $|\nabla[\rho v_m]|_{r,\theta}/(\rho_{av}C_x/c) = 2$, and (b) defect edge locations at trailing edge for 1.25% clearance high speed fan at near-design loading

Step 7: Calculate $\rho v_m/(\rho_e V_e)$

Once the edge values and locations are known, $\rho v_m/(\rho_e V_e)$ can be calculated for each node in the grid. The value of $\rho_e V_e$ to use for each node is determined by searching through the set of edge locations for the one closest to the node.

Step 8: Find set of dA corresponding to defect region

The axial station at which blockage is being quantified corresponds to the set of computational grid nodes in the trailing edge plane of the passage. For such a subset of the computational grid the nodes are found for which the cutoff function is greater than or equal to the cutoff value. If the cutoff function is greater than the cutoff value for four adjacent nodes forming a computational cell face then the cell face (a topological rectangle) is an elemental area, dA. If the cutoff function at some, but not all, of the four adjacent nodes is greater than the cutoff value, locations corresponding to the cutoff value are interpolated between nodes. The interpolated locations constitute vertices of a polygon used as the elemental area; $\rho v/(\rho_e V_e)$ must also be interpolated between grid nodes so

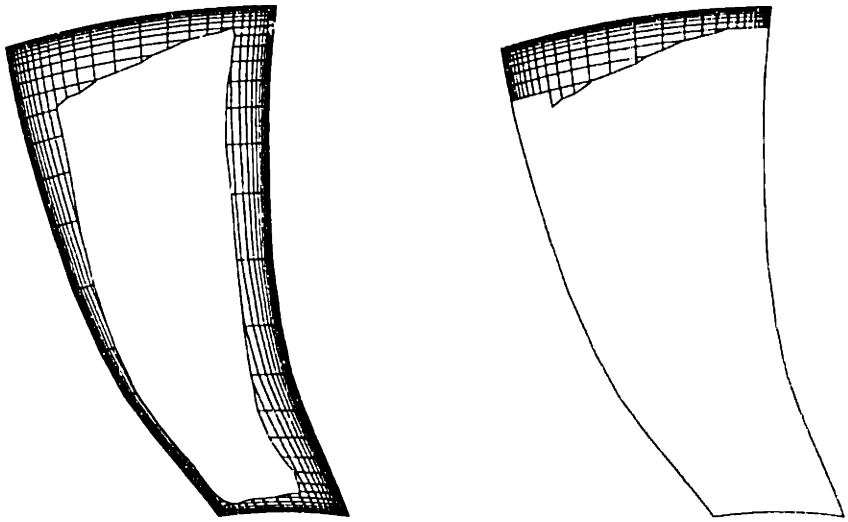

Figure 3-10: Trailing edge (a) total defect region and (b) clearance-related defect region for 1.25% clearance high speed fan at near-design loading

that the integration of this quantity over the area can be performed. Figure 3-10a shows the set of elemental areas obtained for the trailing edge station of the present example.

Step 9: Numerically integrate blocked area

Once $\rho v_m/(\rho_e V_e)$ is known for each vertex of all elemental areas in the defect region, Equation 3.3 can be numerically integrated to obtain the blocked area.

If the blocked area in a certain region of the flow, e.g. the tip region, is desired the procedure does not differ materially but the domain of integration is restricted to exclude areas outside the region of interest. Figure 3-10b shows the region over which tip region blockage was calculated for the fan example illustrated above. From Figure 3-8b it can be seen that the region indicated in Figure 3-10b corresponds to the flow nonuniformity associated primarily with leakage flow rather than blade boundary layers.

The ability of the gradient criterion to identify the clearance-related defect region is most apparent with the large clearance (3.0%) low speed rotor flow

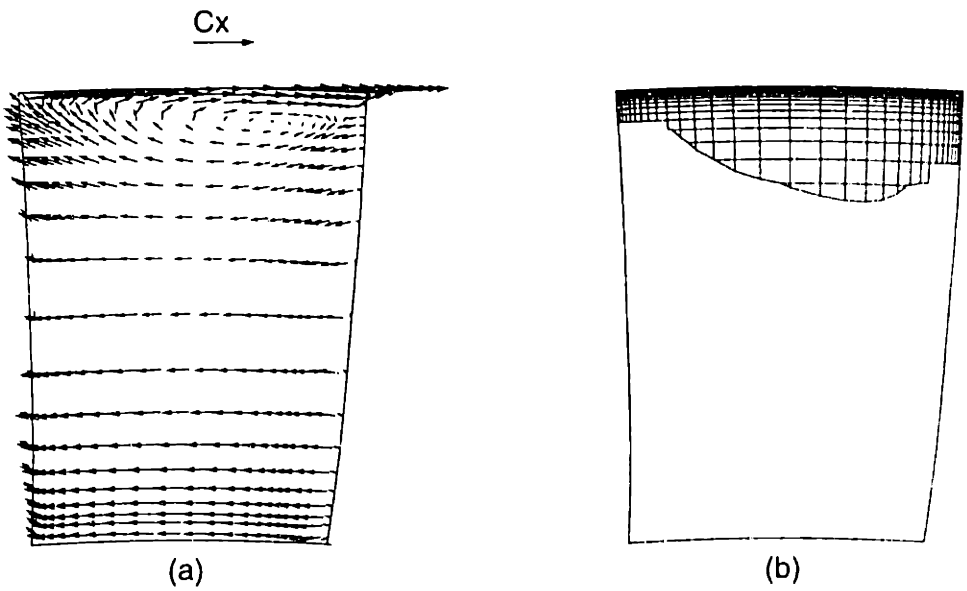

Figure 3-11: (a) Velocity vectors viewed along blade stagger, and (b) clearance-related defect region at trailing edge for computed low speed rotor flow field

fields as in Figure 3-11a. The figure shows velocity vectors viewed along the blade stagger (and hence approximately crossflow vectors) with 3.0% clearance and $C_x/U = 0.42$. The velocity vectors give a rough indication of the location and extent of the clearance vortex. The portion of the computational grid over which the clearance-related blockage is calculated is shown in Figure 3-11b. The near-tip defect region obtained using the gradient criterion as the cutoff function agrees well with the region occupied by the clearance vortex.

3.5 Link Between Mainflow Velocity Component and Core Velocity

3.5.1 Motivation and approach

In Section 3.3.1 it is argued that the velocity in the mainflow direction is the appropriate component to quantify blockage. In this section the choice of the velocity component is evaluated by examining the relationship between flow in the defect region

and core flow. We start with the observation that, if the core region nonuniformity does not vary with blockage an area average of the core velocity and appropriate defect velocity component should scale exactly with mass flow for incompressible and unidirectional flow, and approximately with mass flow for flows in which the density and flow angle variations are minor. The defect velocity component which satisfies this condition is the component that affects the core flow velocity and is thus the proper component for quantifying blockage.

A unidirectional, constant density velocity distribution is shown in Figure 3-12 where defect and core regions are indicated. The area averaged velocity is defined as

$$\begin{aligned} \overline{v} &= \frac{\overline{V}A_c + \overline{v}_d A_d}{A_c + A_d} \\ &\equiv V_i \end{aligned} \tag{3.4}$$

The area averaged velocity, $\overline{v}$, is the velocity that would occur if the flow were unidirectional and uniform and can be called the "ideal core velocity," V_i. For a given mass flow and flow area, independent of the area or velocity distribution of the defect region, V_i is constant. Stated another way, increases in blockage result in increases in average core velocity such that the ideal core velocity is constant.

When the flow is unidirectional there is no question about the proper velocity component to evaluate for each contribution in Equation 3.4 to obtain the ideal average core velocity. With a multidirectional flow, however, a question is whether there is an analogous ideal core velocity. An expression for the ideal core velocity analogous to that of Equation 3.4 is

$$V_i \equiv \frac{\overline{V}A_c + \overline{v}_{?,d}A_d}{A_c + A_d}, \tag{3.5}$$

where A_c and A_d are the areas of the core and defect regions, respectively; and $\overline{V}$ and $\overline{v}_{?,d}$ are the area averaged core velocity magnitude and defect velocity component, respectively. Since Equation 3.5 is for a multidirectional flow, the appropriate velocity

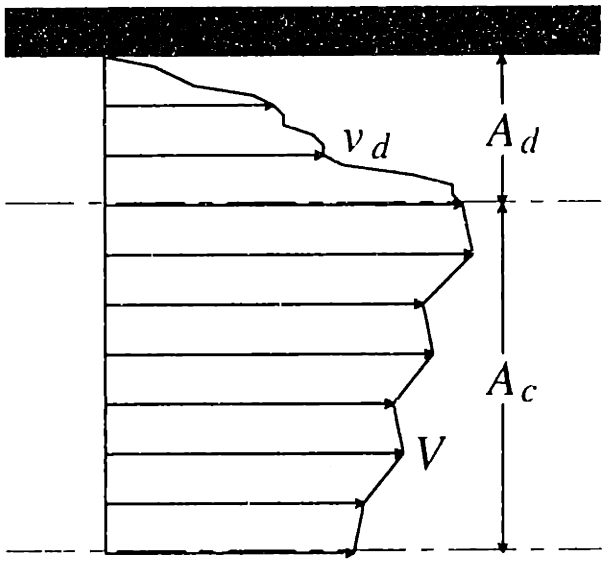

Figure 3-12: Incompressible and unidirectional profile with core and defect regions

component is yet to be determined and is indicated by the subscript "?".

As shown in Section 3.2.2 the main change in core region velocity with blockage for the low speed rotor was in magnitude. If the appropriate velocity component for quantifying blockage is used for $v_{?,d}$ in Equation 3.5, the ideal core velocity should be approximately fixed by the mass flow. This amounts to assuming that the average core velocity behaves as if the core flow is unidirectional. This becomes a poor assumption as the cosine of the core flow angle variation becomes significantly less than 1, so Equation 3.5 is only useful for core flow angle variations of roughly 20 degrees or less. The following options for $v_{?,d}$ will be examined: (1) axial velocity, (2) velocity magnitude, and (3) mainflow velocity component.

3.5.2 Evaluating options for defect velocity component

The effect of using each the three options for the defect contribution in Equation 3.5 is examined below using the computations of the low speed rotor with two different clearances. The edge of the defect region at the exit plane was specified using $|\nabla[v_m]|_{r,\theta}/(C_x/c) = 1$ regardless of which velocity component was integrated over the

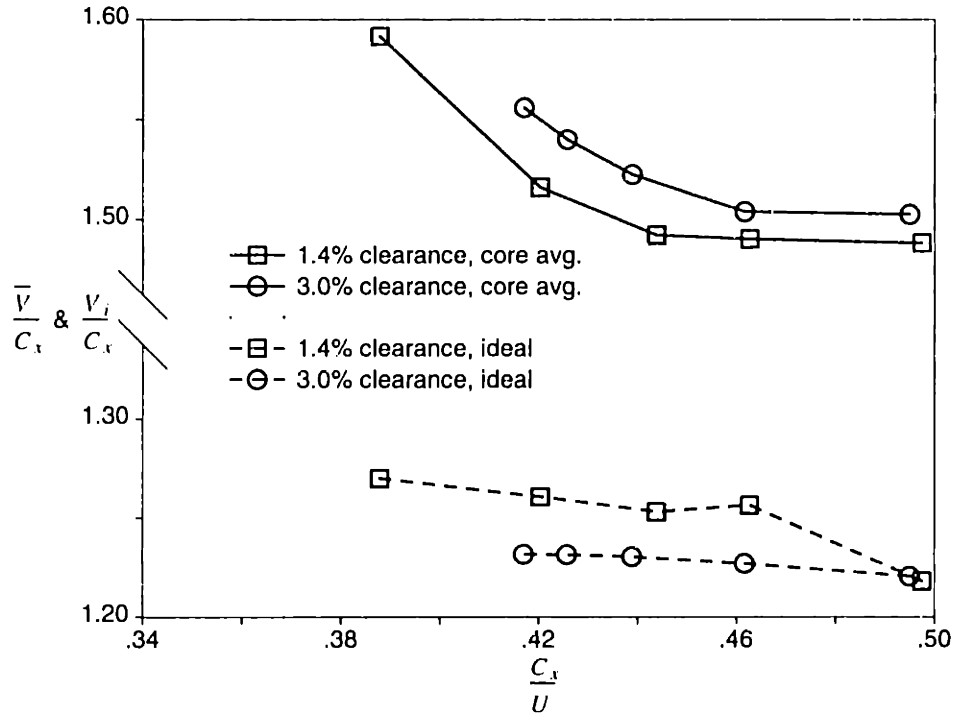

Figure 3-13: $\overline{V}/C_x$ and V_i/C_x using v_x vs. C_x/U at trailing edge for low speed rotor

defect region. The flow angle varies by roughly 10 degrees in the core for these flow fields.

Figure 3-13 shows $\overline{V}/C_x$ (solid curves) and V_i/C_x (dashed curves) as a function of C_x/U for the low speed rotor at two clearances, using v_x for $v_?$ in Equation 3.5. The square and circle symbols indicate 1.4 and 3.0% clearance, respectively. The effect of increasing clearance can be seen as an increase in the average core velocity magnitude. The ordinate axis is split so that the average velocity values with and without the defect contribution fit on the same plot without reducing the ordinate scale. The important point is that the dashed curves are no closer together than the solid curves. In other words, using v_x for $v_?$ in Equation 3.5 does not yield a core velocity that scales with mass flow. The discrepancy between dashed curves in Figure 3-13 indicates that axial velocity in the defect region does not set the average core velocity and is thus inappropriate to quantify blockage.

Note that the core velocity magnitude is used in Equation 3.5, not the core axial velocity. If the axial velocity were used, the resulting quantity would collapse as a function of mass flow since the mass flow is fixed by the average axial velocity at any

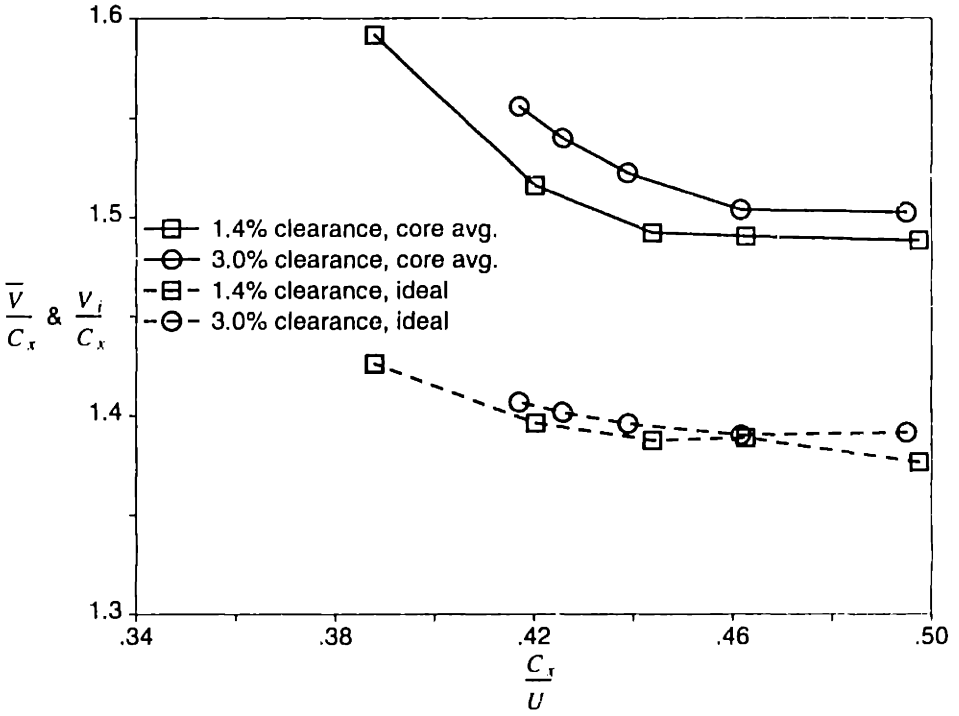

Figure 3-14: $\overline{V}/C_x$ and V_i/C_x using v vs. C_x/U at trailing edge for low speed rotor

axial station. It is the core velocity magnitude that is of interest because of its link with passage pressure rise and blockage.

The dashed curves in Figure 3-14 show the result of using velocity magnitude, v, for $v_?$ in Equation 3.5. The solid curves and axes scaling are the same as for Figure 3-13. The dashed curves are considerably closer together than the solid curves indicating that velocity magnitude in the defect region is largely responsible for setting the average core velocity. However, neglecting the effect of flow direction in the defect region still leaves some difference in the ideal core velocity obtained using Equation 3.5.

The dashed curves in Figure 3-15 result from using v_m for $v_?$ in Equation 3.5. Again, the solid curves and axes scaling are the same as for Figure 3-13. The resulting V_i/C_x roughly scales with mass flow, and the (dashed) curves for the two clearances are almost fully collapsed. This indicates that changes in the the area integral of the mainflow velocity component in the defect region are essentially responsible for changes in the average core velocity. On this basis v_m is the appropriate velocity to use in the blockage definition.

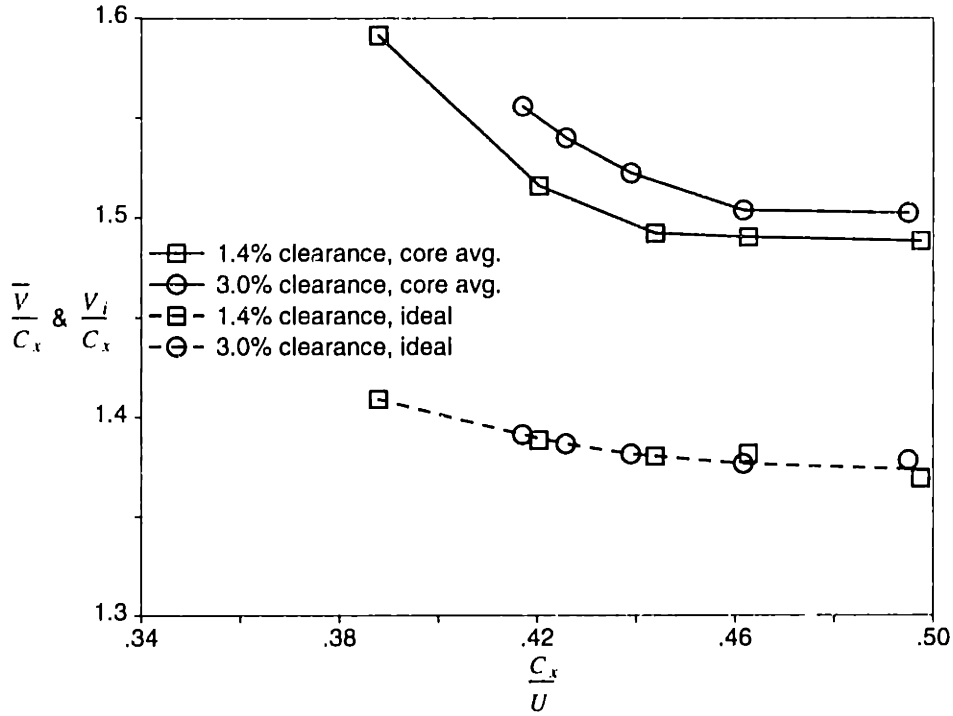

Figure 3-15: $\overline{V}/C_x$ and V_i/C_x using v_m vs. C_x/U at trailing edge for low speed rotor

The core flow angle variation for the transonic fan was large enough so that collapsing the ideal core velocity magnitude could not be achieved. The results of using Equation 3.5 with the transonic fan is presented in Appendix C.

3.6 Results Using Proposed Blockage Definition

3.6.1 Overview of results to be presented

In this section the results obtained with the proposed blockage quantification method are presented for the low speed rotor and the transonic fan, each with two clearances. The blocked areas were obtained at the trailing edge station. Blocked area for the total trailing edge area as well as blocked area due to the clearance flow were calculated. The clearance-related blocked area was obtained by limiting the domain of integration to include the clearance vortex and exclude the blade boundary layers. The *blockage* is defined as blocked area normalized by total area at the trailing edge (i.e., at 100% chord), A_{ex}.

For the low speed cases $|\nabla[\rho v_m]|_{r,\theta}/(\rho_{av}C_x/c) = 1$ was used as the edge cri-

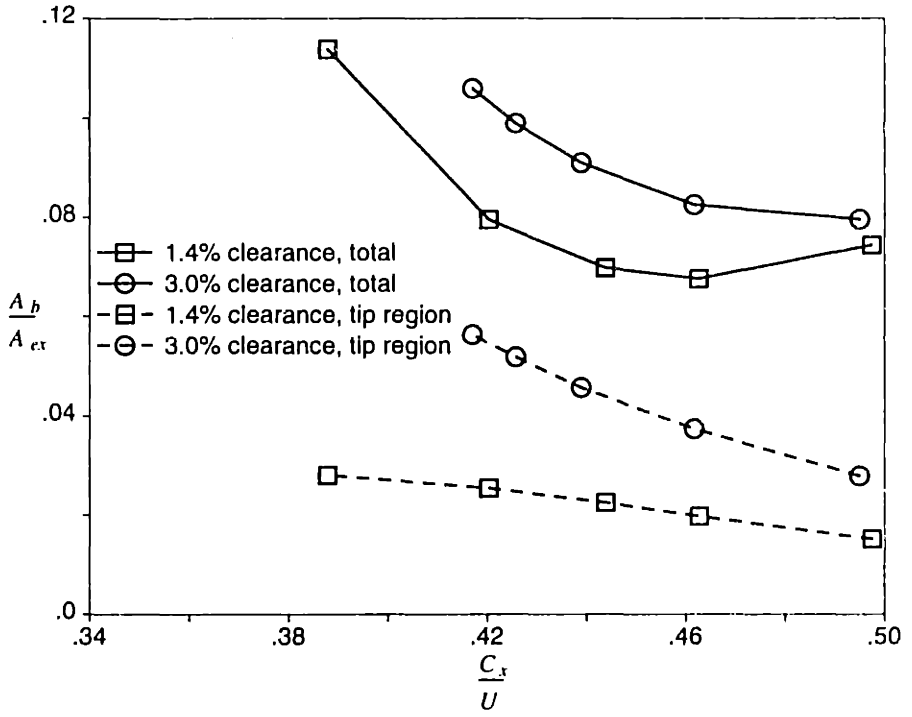

Figure 3-16: Blockage values for low speed rotor

terion. The core region nonuniformity was greater for the high speed cases and $|\nabla[\rho v_m]|_{r,\theta}/(\rho_{av}C_x/c) = 2$ was used for those. The method was not sensitive to the choice of edge criterion value: doubling the gradient magnitude used as the edge criterion decreased the blockage obtained by less than 10%.

3.6.2 Low speed results

Trailing edge blockage obtained for the low speed rotor is plotted against flow coefficient in Figure 3-16. The square and circle symbols correspond to 1.4 and 3.0% clearance, respectively. The solid curves represent blockage calculated over the full span and the dashed curves represent the blockage contribution in the tip region.

Comparison of total blockage and clearance-related blockage for the smaller clearance indicates that little of the computed blockage growth with increased loading is due to clearance flow. The blockage increase with loading is primarily due to growth of the suction surface boundary layer and the development of corner separation as the flow coefficient was reduced.

For the larger clearance, the total blockage and the clearance-related blockage

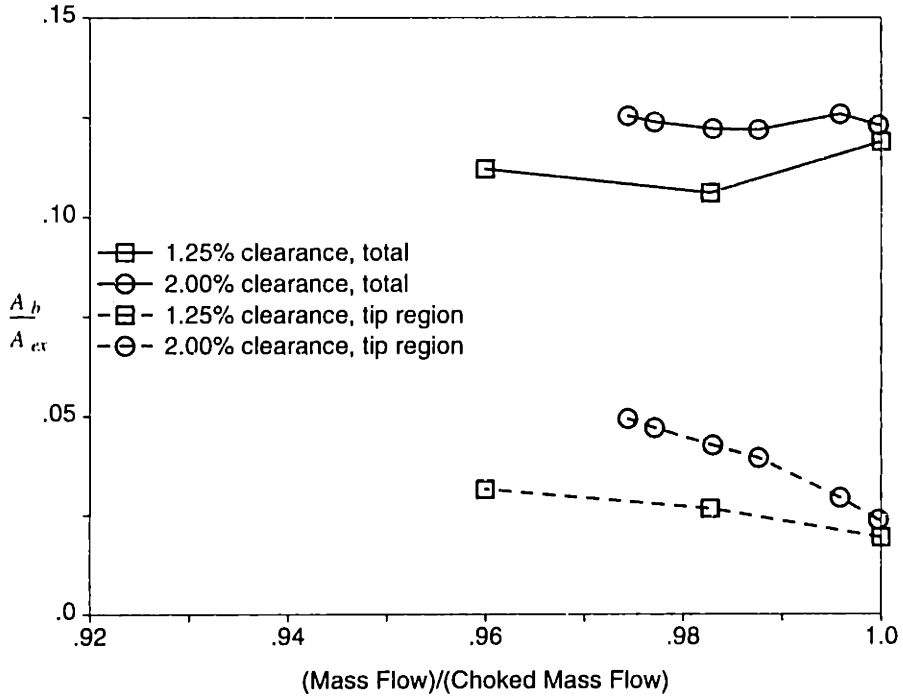

Figure 3-17: Blockage values for high speed fan

are larger than for the smaller clearance. Further, the difference in clearance-related blockage largely accounts for the difference between the solid curves. With 3.0% clearance the growth in clearance-related blockage with loading is almost entirely responsible for the growth in total blockage. In terms of limiting pressure rise increasing the clearance changes the critical region of the flow from the suction surface and hub corner to the tip region.

3.6.3 High speed results

Trailing edge blockage obtained for the high speed rotor cases is plotted against normalized mass flow in Figure 3-17. The square and circle symbols correspond to 1.25 and 2.0% clearance, respectively. The blockage values for 0.25% clearance are not included here because, for this tight clearance, there was no clear clearance vortex at the trailing edge, and it was not possible to identify a defect region due primarily to the effects of clearance. Again, the solid curves represent blockage calculated over the full span while the dashed curves represent the blockage contribution in the tip region.

As with the low speed flow fields, the clearance-related blockage largely accounts for the difference in total blockage between the smaller and larger clearances. Also, larger clearance results in greater clearance-related blockage growth with loading.

3.7 Conclusions

A method for quantifying blockage in axial compressors has been proposed. The blockage definition can be applied to a three-dimensional flow in a manner analogous to displacement thickness for boundary layers. Two issues were resolved in order to obtain an expression for blockage: (1) which velocity component to integrate over the defect region, and (2) what criterion to use for determining the edge of the defect region. The resolution of these issues depends on the fact that there is typically an identifiable mainflow direction and core region in axial compressors.

The velocity component in the mainflow direction is the appropriate component to integrate over the defect region. A good estimate of the mainflow direction at any radius can be obtained by extrapolating the core flow angle at midpitch to the defect regions. The defect region is identified using the gradient of the mainflow component of velocity. The reference velocity used in the expression of blocked area is the core edge velocity nearest to the location being integrated. Using the mainflow velocity in the blockage definition was validated by demonstrating that it is this component which is responsible for changes in the core region velocity magnitude.

The vortical structure associated with the leakage flow was a major factor in enabling the clearance-related defect region to be identified and the corresponding contribution to trailing edge blockage to be quantified. For the flow fields with tight clearance (0.25% of chord) such a vortical structure was not apparent in the trailing edge plane and clearance-related blockage could not be obtained. To quantify the blockage associated with tip clearance, therefore, the clearance-related defect must be distinguishable from the endwall boundary layer.

The blockage method was implemented using three-dimensional Navier-Stokes computations of a low speed compressor rotor and a transonic fan. Overall passage exit blocked area and blocked area associated with leakage flow were presented for two clearances. The level of clearance determines which region of the passage gives the main contribution to blockage growth with increased loading; as clearance is increased the tip region becomes more influential in blockage growth.

Chapter 4

Mechanisms of Clearance-related Blockage Generation

4.1 Introduction

In this chapter the principal mechanisms by which tip clearance contributes to blockage are explained using the Navier-Stokes solutions to (1) examine the flow in the clearance vortex, (2) establish the parametric dependence of blocked area, and (3) develop a fluid dynamic model for clearance-related blockage.

4.2 Role of Leakage Flow Vortical Structure

In Section 3.6 the vortical pattern associated with the clearance flow was seen to be important in identifying the region to be used in quantifying the clearance-related blockage. The quantitative importance of the vortical structure on blockage development, however, was not determined. To assess this the following aspects will be addressed: (1) the relationship between flow properties in the vortex core, (2) the importance of swirl ratio in the growth of the vortex, and (3) the contribution of flow angularity to blockage.

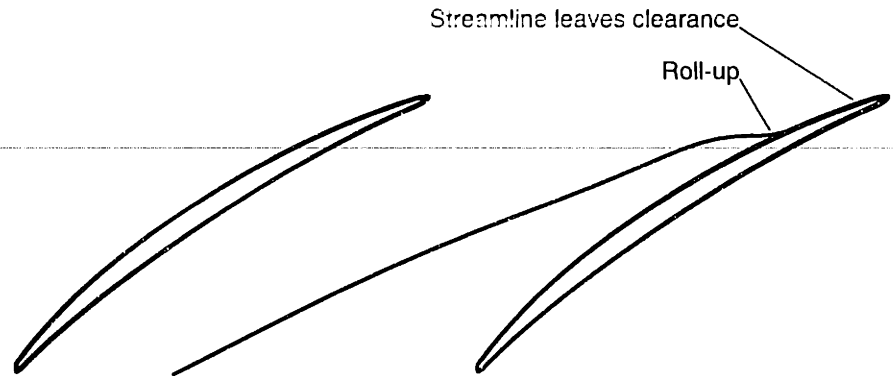

Figure 4-1: Radial view of vortex center streamline for low speed rotor with 3.0% clearance and $C_x/U = 0.42$

4.2.1 Flow in the vortex core

In computations of a cantilevered stator Crook et al. (1993) observed that the region of minimum total pressure roughly corresponded to the center of the clearance vortex, and it was suggested that the clearance vortex core is a significant source of endwall blockage. Examining the relationship between velocity and pressure along a clearance vortex centerline thus gives some insight into the factors that determine the blockage. Flow visualization software (Haimes and Giles, 1991) enabled fluid properties along individual streamlines to be examined.

Figure 4-1 shows a radial view of the vortex center streamline for the low speed rotor flow field with clearance of 3.0% and $C_x/U = 0.42$. The streamline leaves the clearance gap near the blade tip and leading edge. It remains near the suction surface until it reaches the vortex roll-up location near 20% chord and then follows a trajectory somewhat greater than the the blade stagger direction.

Figure 4-2 shows the static pressure coefficient, C_P, and the normalized velocity magnitude, v/C_x, plotted against distance along the streamline from the location

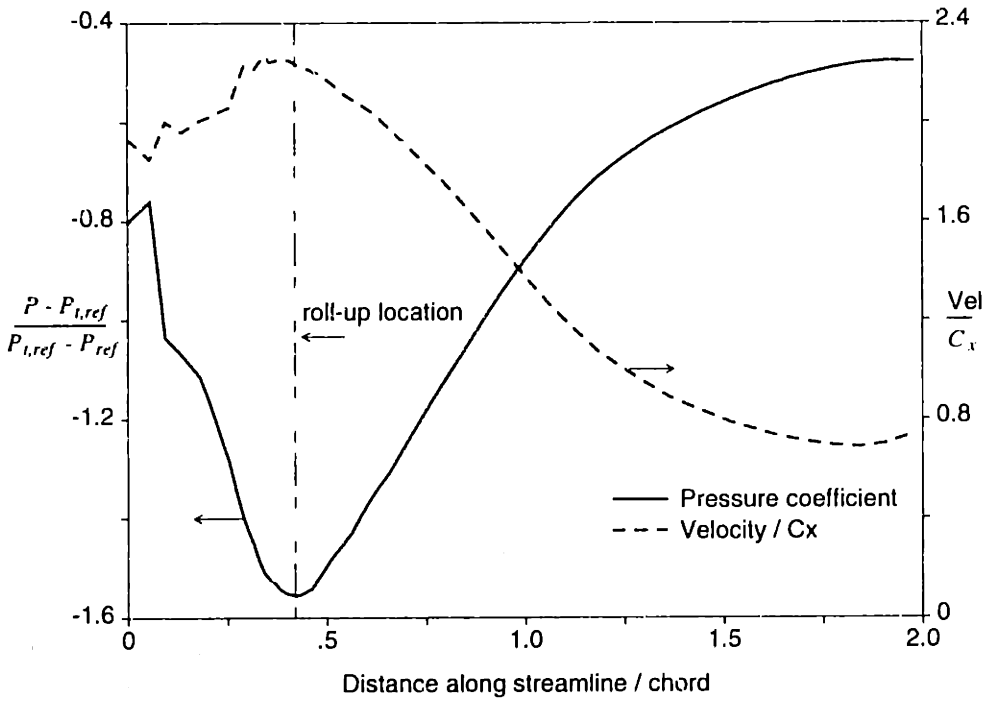

Figure 4-2: C_P and v/C_x along vortex center for low speed rotor with 3.0% clearance and $C_x/U = 0.42$

at which the streamline leaves the clearance. The distance is normalized by the blade chord length. (Note that the abscissa indicates normalized distance along the streamline, not chordwise location within the passage.) The point at which the vortex rolls up and leaves the suction surface roughly corresponds to the location of minimum pressure and maximum velocity. Before the point of roll-up there is a large drop in pressure with little change in the velocity. Downstream of that point there is a relatively large reduction in velocity corresponding to the rise in pressure. The difference in relationship between velocity and pressure for the two regions of this streamline indicates two distinct phenomena.

The solid curve in Figure 4-3 shows C_{P_t} along the same streamline shown in Figure 4-1. The relative total pressure drops sharply upstream of the roll-up location where the streamline remains near the clearance exit. Storer (1991) identified the region near the clearance exit as a region of intense loss. Downstream of the roll-up point there is little further reduction in C_{P_t}. From mid-passage to the trailing edge there is a gradual increase in C_{P_t} due to the energizing of the vortex core fluid by

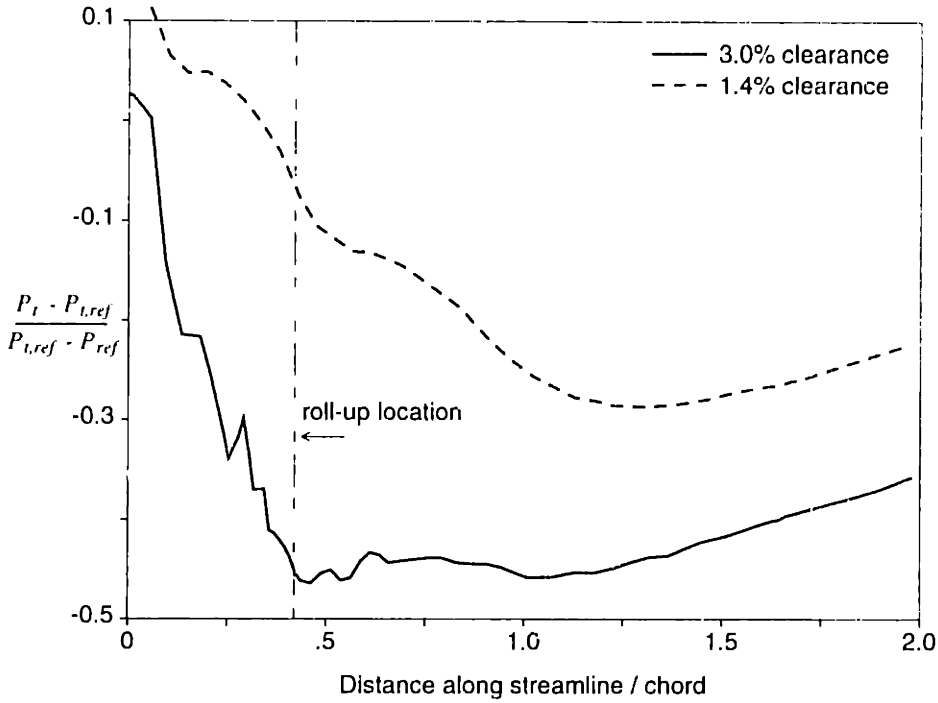

Figure 4-3: C_{P_t} along vortex center for low speed rotor at $C_x/U = 0.42$ for 3.0% and 1.4% clearance

mixing with the surrounding flow. Comparing Figure 4-3 with Figure 4-2 one can see that the increase in total pressure in the vortex core in the aft half of passage is much less than the pressure rise over the same region.

The dashed curve in Figure 4-3 shows C_{P_t} along the vortex center streamline for the 1.4% clearance low speed rotor at the same flow coefficient. The roll-up location (determined as the location of minimum static pressure) is at roughly the same distance along the streamline as for the 3.0% clearance streamline. The total pressure loss occurs more gradually than for the larger clearance and the loss continues downstream of the roll-up point, so there is some reduction in relative total pressure in the vortex core even after the vortex rolls up. However, there is also energizing of the vortex core in the aft half of the passage, so the net change in total pressure between roll-up and passage exit (0.1 of the inlet dynamic pressure) was substantially less than the corresponding static pressure rise (approximately equal to one dynamic pressure).

An assessment of the importance of mixing in the vortex core can be made by comparing the changes along the vortex core to those that would occur if the flow

$\tau/c\%$	$\frac{C_x}{U}$	$\lvert v_1\rvert/U$	$\lvert v_2\rvert/U$	$\frac{\Delta P}{\rho U^2}$	$\frac{\Delta P_i}{\rho U^2}$	$\%\Delta$
1.4	.46	.956	.489	.339	.337	-1
	.42	.957	.427	.403	.366	-9
3.0	.46	.947	.437	.394	.353	-10
	.42	.938	.310	.415	.392	-5

Table 4.1: Comparison of vortex core pressure rise with pressure rise obtained with Bernoulli's equation for low speed rotor

were inviscid. Table 4.1 compares the pressure rise along the vortex centerline in the Navier-Stokes solution with the pressure rise obtained from Bernoulli's equation for the same velocity change. Station 1 corresponds to the roll-up location. Station 2 corresponds to point where the vortex center crosses the passage exit plane. Each row in the table corresponds to a flow field with a particular clearance and flow coefficient for the low speed rotor. The normalized velocity magnitude on the core centerline is indicated for both stations for each flow field. Also shown are normalized pressure rise from the Navier-Stokes computations and the "ideal" pressure rise obtained from Bernoulli's equation using the velocity change from stations 1 to 2. The percent difference between the vortex centerline pressure rise and the ideal pressure rise is tabulated in the last column.

Bernoulli's equation only slightly underpredicts the pressure rise in the vortex core, indicating that the net change in relative total pressure between the roll-up location and passage exit is small compared to the change in static pressure. The compensating effects of loss and mixing account for this observation for the flow field with the 1.4% clearance. Increasing the clearance reduces both the loss and the mixing within the vortex core downstream of the roll-up location. The common result for both of the clearances examined is that the vortex core relative total pressure at the roll-up location largely determines its deceleration in the adverse pressure gradient.

From Figure 2-19a it can be seen that fluid leaving the clearance from the leading

half of the blade near the tip forms the core of the vortex, while fluid from increasingly aft axial locations and further from the tip follows a wider helical trajectory around the vortex core. Fluid particles from the outer radii of the vortex and from outside the vortex do not migrate towards the center of the vortex. These observations, and the tracking of loss along the vortex centerline just discussed, indicate that the low relative total pressure fluid which has been noted by several researchers (e.g., Smith and Cumpsty, 1984 and Crook et al., 1993) to comprise the vortex core is not due to a redistribution of the blade or endwall boundary layer fluid. Rather, it results from loss that occurs as the leakage flow interacts with the passage throughflow.

4.2.2 Effect of swirl ratio on vortex growth

Brookfield (1993) showed that for a Rankine vortex (solid body rotation core and free vortex outer flow) in a pressure gradient there is a critical value of local swirl ratio at which the vortex expands greatly. Swirl ratio is defined as the swirl velocity at the edge of the vortex core divided by the velocity along the axis of the vortex. At a value of swirl ratio near $\sqrt{2}$ the divergence of the vortex in an adverse pressure gradient was greatly increased compared to an axial flow with the same total pressure distribution in the core. Smaller swirl ratios resulted in little difference in vortex core growth between the swirling flow and the nonswirling flow.

Figure 4-4a shows relative velocity vectors at the trailing edge plane of the low speed rotor with 3.0% clearance and $C_x/U = 0.42$. The velocity vectors are viewed along the blade stagger to show the crossflow associated with the vortex. (The blade stagger angle was used since it was roughly the same as the angle that the vortex center made with respect to the axial direction.) The reference vector shown above the vector field indicates the magnitude of the inlet average axial velocity, C_x. Except very near the wall, where the crossflow velocity is high due to the wall motion relative to the blade, the crossflow is considerably less than C_x.

Figure 4-4b shows contours of the magnitude of the relative velocity component

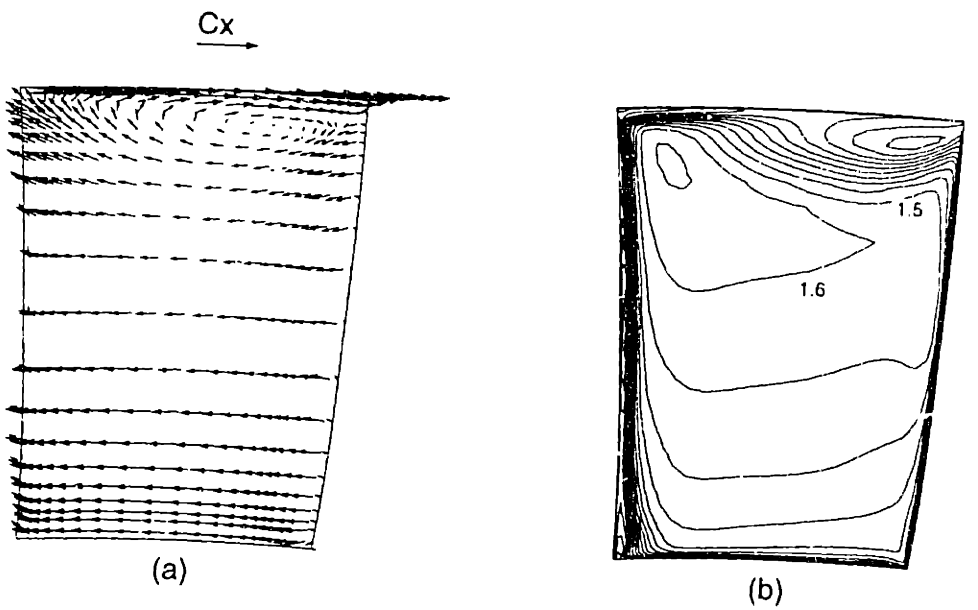

Figure 4-4: Velocity viewed along vortex axis for low speed rotor with 3.0% clearance and $C_x/U = 0.42$: (a) vectors perpendicular to the stagger direction compared to C_x and (b) velocity along the stagger direction normalized by C_x

resolved along the stagger direction, which is roughly along the vortex axis, normalized by C_x. The component of velocity along the stagger is somewhat larger than C_x and the swirl ratio is considerably less than $\sqrt{2}$. The maximum value of swirl ratio associated with the vortical flow is roughly 0.5 for this rather large clearance (3.0% of chord) flow field. For all the flow fields examined, decreasing the clearance decreased the swirl ratio. The low swirl ratios imply that swirl does not play a significant part in vortex growth for these flow fields.

The circulation shed into the clearance vortex and thus vortex swirl can increase with increased clearance as is shown in Appendix A. Further, "aggressive" blading, with higher blade bound circulation than for the flow fields examined here, would tend to result in greater vortex swirl. However, as explained in Appendix B, the measured vortex circulation is also influenced by diffusion of vorticity and the proximity of the endwall results in vortex circulation values which are significantly less than the circulation shed from the blade tip. It is therefore reasonable to expect that role of swirl is minor even in situations in which the blade loading near the tip is higher than

Blade	$\tau/c\%$	Load.	A_b w/ CF	A_b w/o CF	$\%\Delta$
Stator	1.75	min	.0171	.0155	-9
Stator	3.5	max	.0350	.0319	-9
LSR	1.4	min	.0198	.0164	-17
LSR	3.0	max	.0563	.0484	-14
Fan	1.25	min	.0194	.0153	-21
Fan	2.0	max	.0494	.0459	-7

Table 4.2: Comparison of clearance-related blockage obtained with and without the crossflow contribution

for the cases examined here.

4.2.3 Effect of flow angularity on endwall blockage

For a given relative total pressure and static pressure in the vortex, increasing the crossflow components of velocity reduces the the mainflow component and increases blockage. If a considerable portion of the blockage associated with tip clearance is due to the departure of the flow from the mainflow direction, both relative total pressure and direction will have to be considered. On the other hand if the flow direction makes only a minor contribution to the blockage, it is the relative total pressure distribution and the exit pressure which determine the blockage.

A simple way to assess the importance of flow direction is to calculate clearance-related blockage as if the direction did not matter, and then compare the result to that obtained using the blockage definition given in Section 3.3.3. Neglecting the contribution of the crossflow is the same as substituting velocity magnitude for mainflow velocity component in the blockage definition. Clearance-related blockage values obtained in this manner were obtained for flow fields with clearances ranging from 1.25 to 3.5% of chord. These values are compared with the blockage obtained previously (including the effect of crossflow) in Table 4.2.

The terms "min" and "max" refer to the minimum and maximum loading points on the computed speedline corresponding to the geometry and clearance indicated

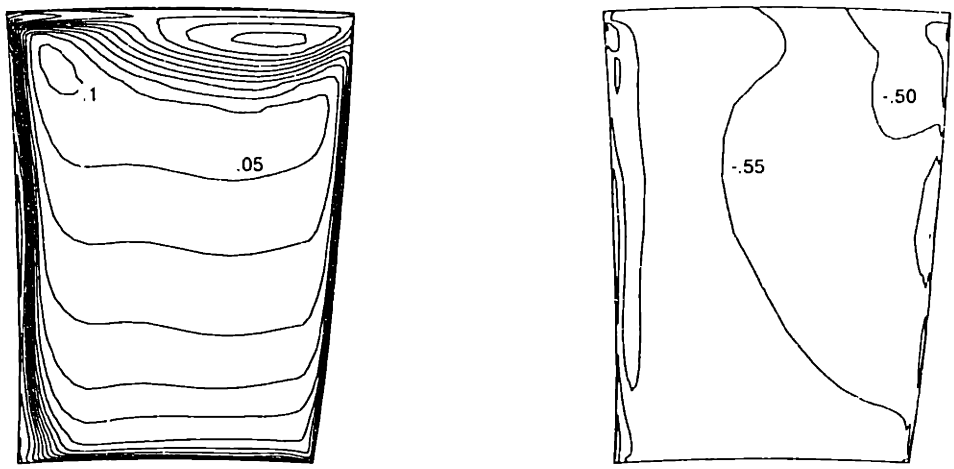

Figure 4-5: (a) C_{P_t} and (b) C_P at trailing edge for low speed rotor with 3.0% clearance and $C_x/U = 0.42$

in each row of Table 4.2. For the geometries, clearances, and loadings examined the blockage obtained by neglecting the direction of the flow at the trailing edge plane was within 20% of the value obtained when the direction was accounted for, implying that crossflow makes only a minor contribution to the clearance-related blockage.

The importance of relative total pressure level, compared to crossflow, in determining the blockage can be seen by comparing the variations in relative total pressure and in static pressure at compressor exit. Figure 4-5a shows contours of C_{P_t} at the trailing edge plane for the low speed rotor with 3.0% clearance and $C_x/U = 0.42$. Figure 4-5b shows contours of C_P for the same flow field and station using same fraction of dynamic pressure for the contour interval. Variations in static pressure are considerably less than those in total pressure, so it is the local defects in relative total pressure near the endwall that have the major impact on blockage.

While the effect of swirl on blockage growth and the contribution of the flow angularity to blockage were found to be minor, there is a key role that the presence of a vortical structure plays. The presence of an identifiable vortex core suggests that

the high loss fluid is concentrated in that region as a result of the formation of the vortex. This implies less mixing of this low energy fluid than would otherwise occur, and thus higher blockage. Also, since the leakage flow leaving the clearance has a relative total pressure which is similar to that of the freestream, the defect in total pressure in the vortex core indicates that much of the crossflow energy is lost as the flow is turned into the mainflow direction.

4.3 Parametric Dependence

4.3.1 Obtaining relevant parameters

The results of flow visualization in the tip region indicate that the principal contribution to blockage comes from the increase in area occupied by low relative total pressure fluid in negotiating the adverse pressure gradient in the passage. The total pressure defect results from the interaction between the leakage and the passage flow. The vortical structure need not be considered, except insofar as it affects the relative total pressure distribution. Thus, a simple yet plausible view of the development of clearance-related blockage is that of the growth of a one-dimensional streamtube (if appropriate averages are used). With this view, we seek to describe the endwall blockage in terms of an appropriate loading parameter.

The factors that determine the blocked area due to tip clearance can be suggested to be: (1) the size of the clearance vortex core or total pressure defect, (2) the severity of the relative total pressure defect, (3) the passage pressure rise in the tip region, and (4) the inlet dynamic pressure for the tip region (since we are considering a streamtube near the tip). The high speed computations did not provide any strong evidence that the list of important factors is different for transonic and subsonic flow, so a common set of parameters will be sought for both low and high speed flows.

The size of the defect region at the passage exit might be expected to scale with the clearance area. Thus, clearance, τ, and blade chord, c, should be included in the

list of parameters which determine the blocked area.

Streamlines in the endwall region indicate that flow which enters the passage from the clearance acquires a direction which is approximately that of the mainflow as it rolls up into the clearance vortex. This is a consequence of the fact that much of the leakage crossflow appears to be dissipated within a short distance (relative to the blade chord) into the passage.

Models for clearance-related loss such as that presented by Storer and Cumpsty (1993) suggest that increasing leakage crossflow momentum increases the loss. The correspondence between leakage crossflow momentum flux and endwall loss suggests that a reasonable hypothesis is that the loss of leakage crossflow momentum (the product of the density and square of the the leakage velocity component normal to the blade) largely determines the decrease in total pressure in the clearance vortex. Storer and Cumpsty (1991) indicated that this quantity depends on midspan loading. Therefore, the midspan pressure difference acoss the blade, denoted by $\Delta_B P$, will be added to the list of parameters.

Changes in the relative total pressure along a streamtube in the clearance vortex occur as a result of mixing. For example, flow visualization of computed flow fields indicated that the flow in the vortex core is energized by the surrounding fluid. These are reflected in the average total pressure change in the endwall region denoted by ΔP_t.

Items (3) and (4) in the list of important factors are denoted by the parameters ΔP and Q_{in}, respectively. The list of parameters relevant to the clearance-related blocked area at passage exit is thus: τ, c, ΔP, $\Delta_B P$, ΔP_t, and Q_{in}.

4.3.2 Normalizing blocked area

In the computations blockage is calculated in nearly axial planes. Thus, the plane "slices" the defect region at roughly the mainflow angle with respect to the axial direction. The mainflow angle varies with radius, but a value which is representative

of the clearance-related defect region is β_e, the flow angle at the edge of the defect at midpitch. For each geometry the blocked area in an axial plane will depend on the flow defect as well as the angle that the plane makes with the mainflow direction. To remove this dependence on plane orientation, the quantity $A_b \cos\beta_e$ will be related to the relevant parameters obtained above.

Because of its relation to clearance mass flow, the clearance area, τc, appears appropriate to normalize the blocked area at passage exit.

The severity of the total pressure defect in the tip region is related to the leakage crossflow momentum flux normal to the blade. The crossflow leakage momentum flux per unit area scales with the square of the leakage velocity normal to the blade, which is fixed by the pressure difference across the blade (Storer and Cumpsty, 1991). Increasing $\Delta_B P$ tends to increase A_b. Thus, $\Delta_B P$ should appear in the denominator of the normalized blocked area expression.

$\Delta_B P$ must be normalized by another quantity with the same units to construct a non-dimensional blocked area. Of the parameters listed as relevant to the blocked area, ΔP, ΔP_t, and Q_{in} have the same dimensions as $\Delta_B P$. The relationship of ΔP to $\Delta_B P$ is linked to the blade geometry and ΔP will be used to normalize $\Delta_B P$ in the non-dimensional blocked area parameter. The relationship between the two pressure difference parameters is derived below.

Figure 4-6 shows a control volume consisting of a constant radius slice of a blade passage. Neglecting viscous forces and assuming that the flow is two-dimensional the blade force due to the blade pressure difference acts in the vector mean flow direction, β_{vm}. The axial component of the blade force balances the axial force due to the passage pressure rise. Balancing the forces in the axial direction yields

$$\frac{\Delta_B P}{\Delta P} = \frac{s}{c}\frac{1}{\sin\beta_{vm}}.$$

A non-dimensional blocked area parameter (corresponding to the trailing edge of

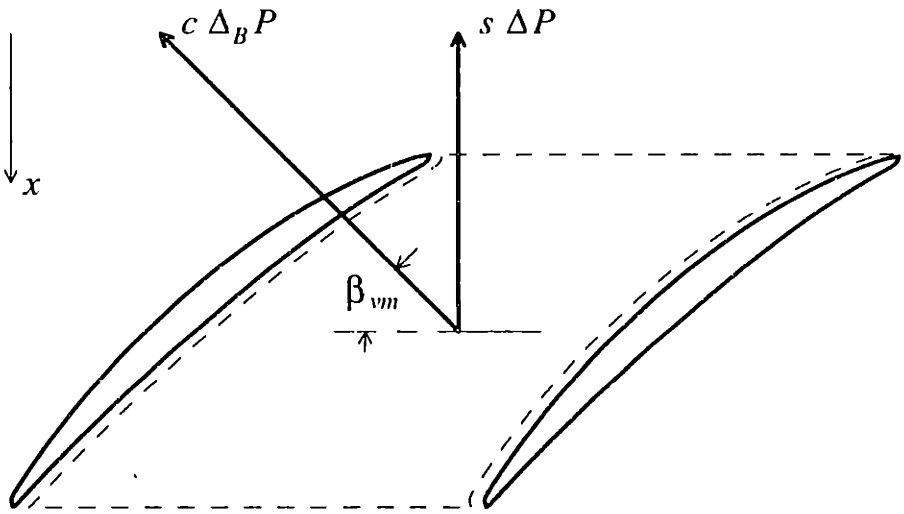

Figure 4-6: Control volume of blade passage to obtain relationship between passage and blade pressure differences

the passage), $A_b \cos\beta_e/(\tau c\frac{\Delta_B P}{\Delta P})$, can thus be written as

$$\frac{A_b \cos\beta_e}{\tau s/\sin\beta_{vm}}.$$

A surprising result is that the blade chord drops out of the parameter, so that the clearance-related blocked area A_b, does not depend on the length of the clearance gap from the leading edge to the chordwise station at which A_b is calculated. Chord and spacing, c and s, respectively, are taken at the blade tip. The flow angles at the tip do not relate to the blade loading as illustrated in Figure 4-6 since the endwall flow is strongly three-dimensional. Therefore, vector mean flow angle, β_{vm}, is obtained at midspan.

4.3.3 Choosing loading parameter

In Section 4.2.1 the strong link between deceleration and pressure rise along the vortex core downstream of the roll-up location was illustrated for the low speed rotor. If we

regard the overall endwall flow as a streamtube from a station upstream of the blade row to the passage exit near the endwall, it is reasonable to expect that the passage pressure rise coefficient near the endwall is a primary variable which determines its deceleration, or blockage growth. The extent of the endwall streamtube and the radial location for the pressure rise coefficient should be based on the location of the clearance-related defect region, i.e., the clearance vortex.

The reference dynamic pressure, Q_{in}, can vary considerably with radial location in the endwall boundary layer and the radial location used for reference should represent a mean distance of the clearance-related defect region from the endwall. As is evident from Figure 1-2, the mean distance of the clearance-related defect from the endwall is a few clearance heights. The upstream reference location for the pressure rise coefficient will thus be taken (somewhat arbitrarily) at 2τ from the endwall. As is shown in Appendix D, a distance of 3τ can also be used with the present flow fields to yield essentially the same parametric dependence.

Using a distance such as two or three clearance heights for the reference conditions relevant for the endwall flow also appears reasonable based on an estimate of the growth of a shear layer presented in Section B.3.3. Casting the average velocities for the leakage and passage flow into velocities for a planar shear layer indicates that the vorticity thickness spreads to one clearance height (3% of chord for the example in Section B.3.3) over a streamwise distance of 50% of chord. Hence, for similar leakage to passage flow velocity ratios and clearance levels the location of minimum relative total pressure associated with leakage would be expected to be from one to a few clearance heights from the endwall at the exit of the blade row.

Because the blockage development is regarded here as one-dimensional, an appropriate average pressure rise coefficient over the clearance-related defect region is required. An area average is a simple choice which weights low total pressure regions (which grow the most in the adverse pressure gradient) more heavily. The difference between the area averaged pressure over the defect region and the upstream value 2τ

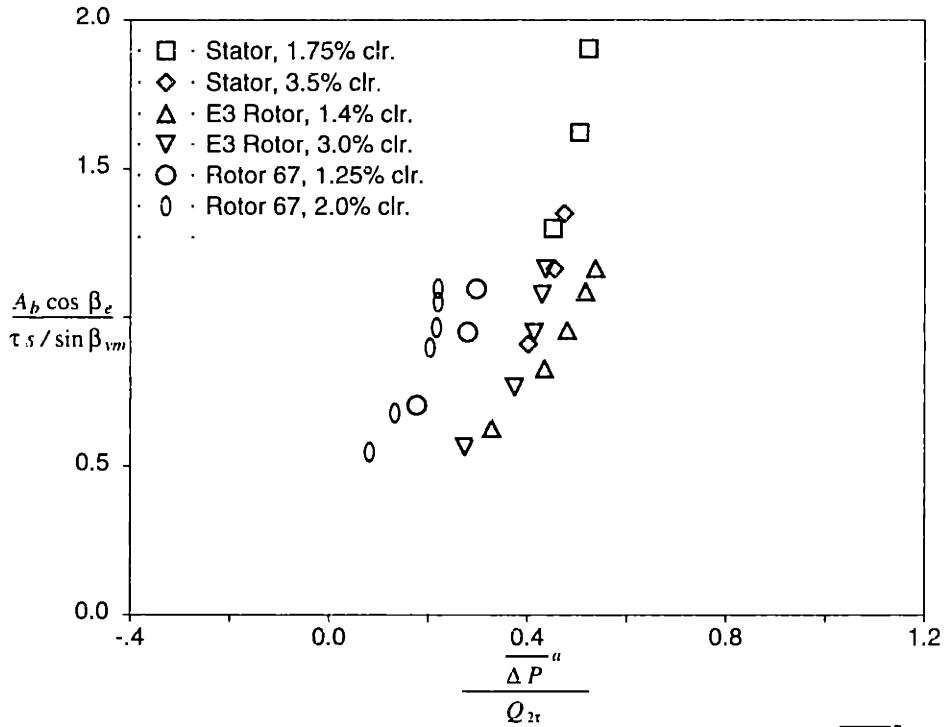

Figure 4-7: Trailing edge $A_b \cos\beta_e/(\tau s/\sin\beta_{vm})$ vs. $\overline{\Delta P}^a/Q_{2\tau}$

from the endwall is denoted by $\overline{\Delta P}^a$.

Figure 4-7 shows $A_b \cos\beta_e/(\tau s/\sin\beta_{vm})$ vs. $\overline{\Delta P}^a/Q_{2\tau}$ for the stator, low speed rotor, and high speed fan, each at two clearances. Changing the clearance changes the normalized blocked area for a given pressure rise. This implies that an additional parameter is required in the normalization.

At a given blade loading increasing clearance increases the spatial extent of the total pressure defect associated with tip clearance. This decreases the mixing and thus the energizing of the minimum total pressure streamline. Increasing the clearance should thus result in greater blockage growth for a given passage pressure rise.

The change in relative total pressure from inlet to passage exit is reflected in ΔP_t. For incompressible flow the velocity change is related to static and total pressure changes along a streamline as follows:

$$\frac{\Delta P - \Delta P_t}{\frac{1}{2}\rho V_1^2} = 1 - \left(\frac{V_2}{V_1}\right)^2$$

The same reference location and averaging method is used for the total pressure

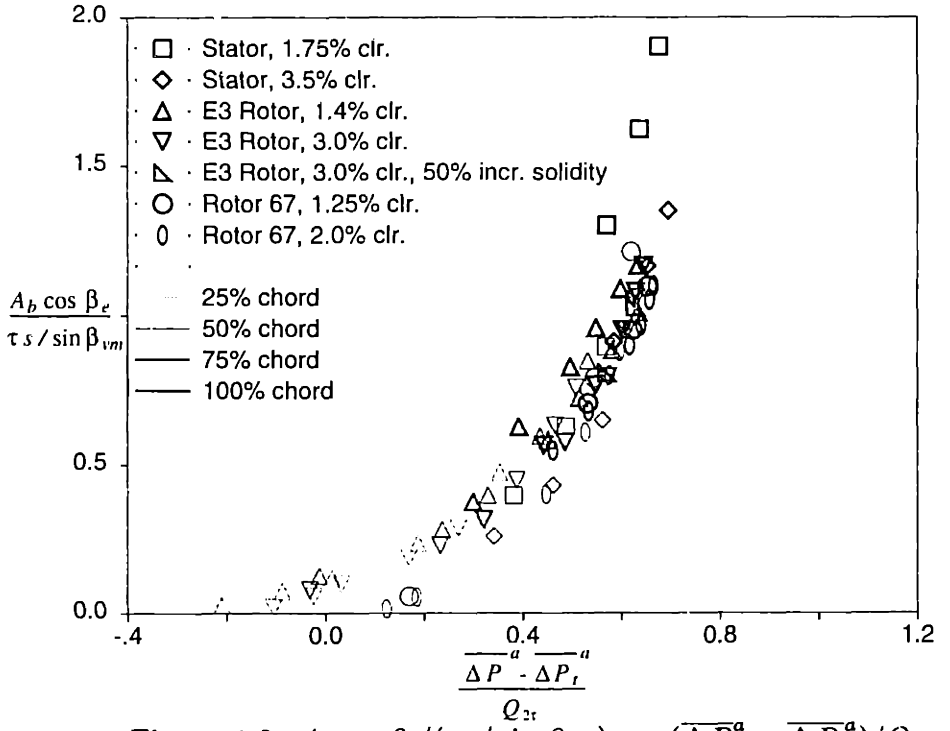

Figure 4-8: $A_b \cos\beta_e/(\tau s/\sin\beta_{vm})$ vs. $(\overline{\Delta P}^a - \overline{\Delta P_t}^a)/Q_{2\tau}$

coefficient as for the static pressure coefficient. Because the relative total pressure decreases from upstream to passage exit the quantity $\overline{\Delta P}^a - \overline{\Delta P_t}^a$ is greater than $\overline{\Delta P}^a$. Data points for larger clearances should move to the right relative to those for smaller clearances, tending to collapse the overall data spread.

Figure 4-8 shows $A_b \cos\beta_e/(\tau s/\sin\beta_{vm})$ vs. $(\overline{\Delta P}^a - \overline{\Delta P_t}^a)/Q_{2\tau}$ for all computed flow fields with clearance of 1.25% or greater.[1] Non-dimensional blocked area versus loading parameter data points are plotted for the passage exit station as well as for other axial locations. The averages of P and P_t used to construct the loading parameter were taken over the clearance vortex at the corresponding axial station. Different axial locations are indicated by the different line types for each symbol. The data collapse onto a narrow band, suggesting that this combination of non-dimensional blocked area and loading parameter captures the parametric dependence of clearance-related blockage for the flow fields examined.

All of the physical geometries upon which the computations were based had solidi-

[1]In the 0.25% clearance fan flow fields the defect region associated with clearance could not be identified, so clearance-related blocked area could not be obtained.

ties (chord to spacing ratios) near unity. To examine the effect of solidity, data from two low speed rotor computations with a solidity 1.5 times the solidity of the physical blade passage is also plotted in Figure 4-8. These two points, plotted with right triangle symbols, also fall on the band. This serves to emphasize that blade spacing, not chord, is a relevant parameter for clearance-related blockage. The independence of blockage on chord is further demonstrated in Appendix E.

For rotor flow fields with significant radius change near the tip, one might consider using reduced and rotary quantities to construct the loading parameter rather than the static and relative total quantities used in Figure 4-8. For incompressible flow the term $\rho(r\omega)^2/2$ appears in both the reduced pressure and the rotary total pressure, so the term drops out of the loading parameter. For compressible flow reduced pressure and rotary total pressure lose their significance due to density variations. Hence there is no benefit to using using reduced pressure and rotary total pressure to construct the loading parameter.

The loading parameter, $(\overline{\Delta P}^a - \overline{\Delta P_t}^a)/Q_{2\tau}$, was developed for incompressible flow with a total pressure change. Figure 4-8 indicates that even the compressible flow data points collapse onto the narrow band. One might ask if this is is coincidental, i.e., whether the collapsing of high speed and low speed data is because the important flow physics have been captured or simply because important but cancelling physics have been ignored.

To address this question the effects of using a loading parameter which relates to the velocity change for a compressible streamtube will be examined. If there is no net heat and work transfer into a streamtube, the enthalpy change determines the velocity change, i.e.,

$$\frac{\Delta H}{\frac{1}{2}V_1^2} = 1 - \left(\frac{V_2}{V_1}\right)^2 .$$

Figure 4-9 shows $A_b \cos\beta_e/(\tau s/\sin\beta_{vm})$ vs. $\overline{\Delta H}^a/\frac{1}{2}V_{2\tau}^2$ for the same flow fields and stations plotted in Figure 4-8. The data do not collapse as well as they did when

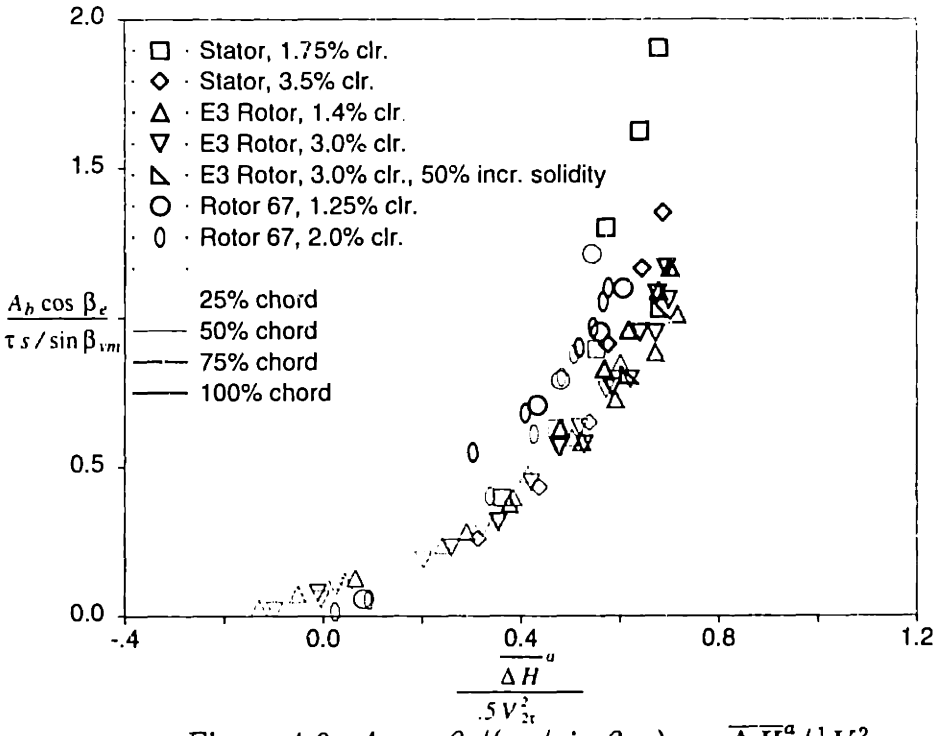

Figure 4-9: $A_b \cos\beta_e/(\tau s/\sin\beta_{vm})$ vs. $\overline{\Delta H}^a/\frac{1}{2}V_{2\tau}^2$

the static and relative total pressure changes were used.

The data which are furthest from collapsing are the points for the transonic fan in which the casing radius is not constant. The loading parameter used in Figure 4-9 does not account for radius changes for the streamtube and a reduced enthalpy change coefficient might be more appropriate.

Figure 4-10 shows $A_b \cos\beta_e/(\tau s/\sin\beta_{vm})$ vs. $\overline{\Delta H^{\bullet}}^a/\frac{1}{2}V_{2\tau}^2$ for the same flow fields and stations plotted in Figure 4-8. The reduced enthalpy is the static enthalpy minus $(r\omega)^2/2$. The collapsing of the data is improved in comparison to Figure 4-9, but the trend is not as distinct as that shown in Figure 4-8.

An effect assumed to be negligible when using $\overline{\Delta H^{\bullet}}^a/\frac{1}{2}V_{2\tau}^2$ as the loading parameter is work transfer from the endwall to the tip-region streamtube. Work transfer due to the endwall motion relative to the blade passage results in a net increase in relative total enthalpy to the endwall flow.[2] A more general parameter is one which

[2]We have assumed that the solid boundaries are adiabatic in the computations, so there is no heat transfer to or from the endwall.

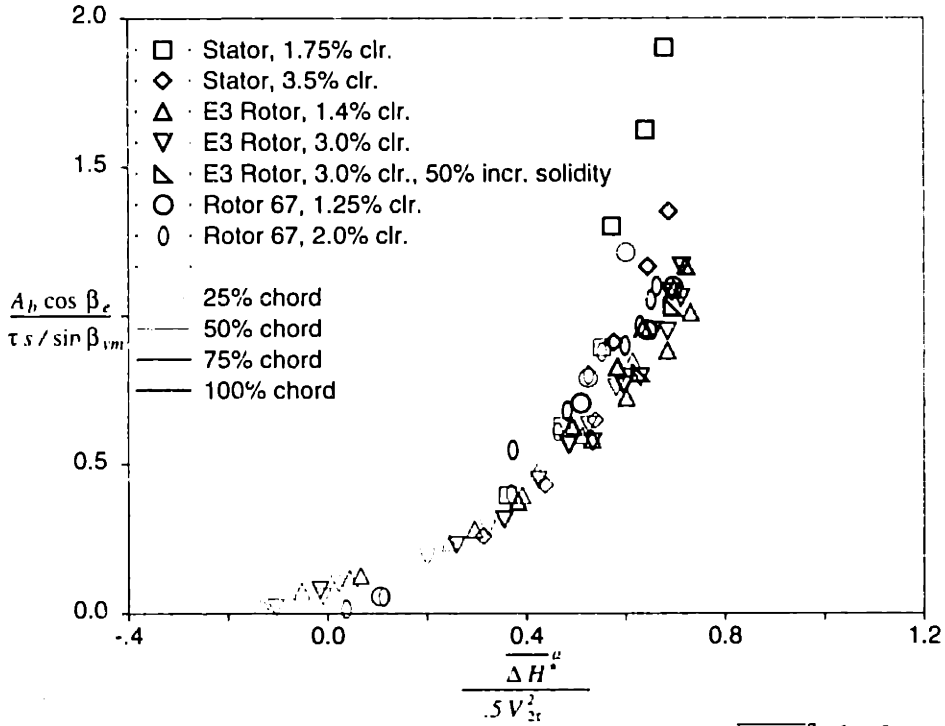

Figure 4-10: $A_b \cos\beta_e/(\tau s/\sin\beta_{vm})$ vs. $\overline{\Delta H^*}^a/\frac{1}{2}V_{2\tau}^2$

allows for changes in rotary total enthalpy (or rothalpy), H_t^*:

$$\frac{\Delta H^* - \Delta H_t^*}{\frac{1}{2}\rho V_1^2} = 1 - \left(\frac{V_2}{V_1}\right)^2$$

Since the $(r\omega)^2$ terms in H^* and H_t^* cancel, the static and relative total enthalpies can be used instead and the parameter will be the same. Figure 4-11 shows $A_b \cos\beta_e/(\tau s/\sin\beta_{vm})$ vs. $(\overline{\Delta H}^a - \overline{\Delta H_t}^a)/\frac{1}{2}V_{2\tau}^2$ for the same flow fields and stations plotted in Figure 4-8. As in Figure 4-8, the data collapse well.

The final loading parameter, $(\overline{\Delta H}^a - \overline{\Delta H_t}^a)/\frac{1}{2}V_{2\tau}^2$, is the most generally applicable loading parameter of the ones examined: it is suitable for low and high speed flows with and without radius changes. While this parameter does specify the velocity ratio for a compressible streamtube, it does not rigorously specify the area ratio since the density is not fixed. However, for the flow range represented by the computations, this loading parameter appears to fix the non-dimensional blocked area parameter. Also, comparison of Figures 4-8 and 4-11 suggests that the equivalent loading parameter for incompressible flow (using static and relative total pressure changes) is useful even

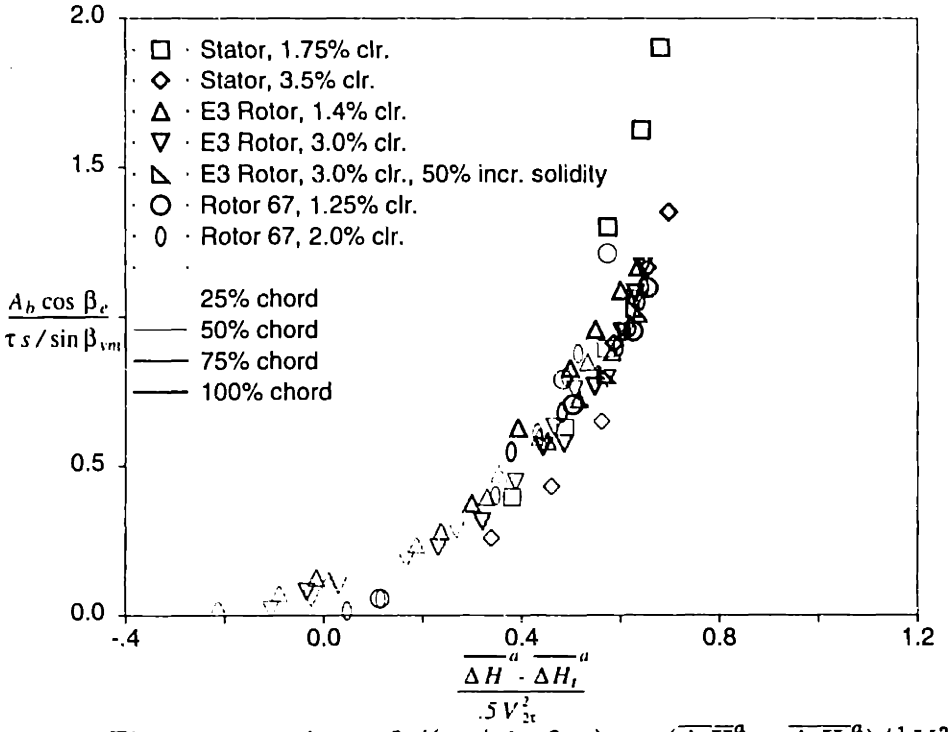

Figure 4-11: $A_b \cos\beta_e/(\tau s/\sin\beta_{vm})$ vs. $(\overline{\Delta H}^a - \overline{\Delta H_t}^a)/\frac{1}{2}V_{2\tau}^2$

for the transonic flow fields.

Since static and total pressures are commonly measured in experiment, and because their effect on velocity is readily apparent for incompressible flow, the loading parameter of Figure 4-8 would have advantages over the more general parameter in most axial compressor flow fields. However, as the radius change in a compressible flow becomes more significant, the more general parameter becomes more appropriate.

4.4 Fluid Dynamic Model

4.4.1 Important modeling aspects

The computations show that the essential features which must be included in a model for clearance-related blockage are: (1) the decreased P_t due to the leakage flow compared to that at the upstream station, (2) the adverse passage pressure gradient, and (3) the mixing of the low P_t fluid. A simple flow which includes these features is a two-dimensional turbulent wake in an adverse pressure gradient and it is useful to cast a model for blockage in these terms. The point of this simplified approach

(compared to the three-dimensional Navier-Stokes computations) is not to provide blockage values, but rather to highlight the essential physics and to enable the role of the important blockage mechanisms to be assessed. We with thus model the leakage flow in this fashion as described below.

4.4.2 Brief description of wake model of Hill et al. (1963)

Hill et al. (1963) derived a equations describing the growth of a two-dimensional wake. As input the model requires two parameters for the wake (for example, depth and width), the streamwise variation in freestream velocity, and a description of eddy viscosity. The model assumes two-dimensional incompressible flow, wake profile similarity, shape factor near unity, small wake depth, and constant value of eddy viscosity normalized by the product of the momentum thickness and the local freestream velocity.

In experiments with a bluff body in a uniform stream Hill et al. (1963) found that the wake profiles at all downstream locations could be collapsed in terms of wake depth and wake width as shown in Figure 4-12. The wake depth parameter is defined as

$$\beta = \frac{U - u_c}{U}$$

where

$$U = \text{freestream velocity, and}$$

$$u_c = \text{velocity at wake centerline.}$$

The wake width, b, is defined as the distance across the wake where $u = (U - u_c)/2$.

The integrals in the streamwise momentum and moment of momentum equations were evaluated assuming $\beta \ll 1$. Also, the relation between the eddy viscosity of the

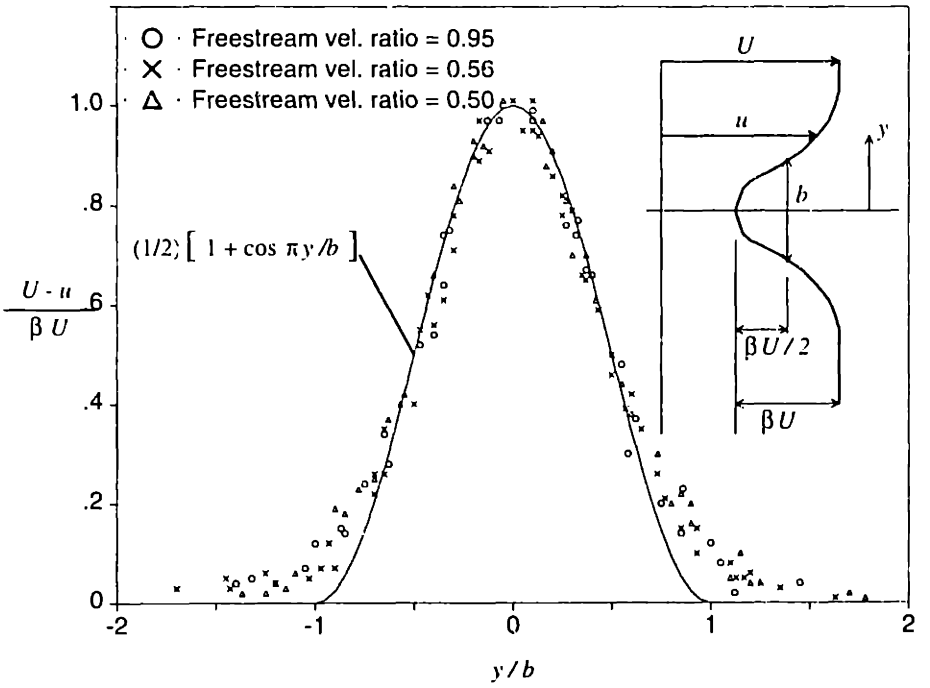

Figure 4-12: Normalized wake profiles from Hill et al. (1963)

wake and wake parameters was assumed as

$$\frac{\epsilon}{U\theta} = \text{constant} \tag{4.1}$$

where ϵ is the eddy viscosity coefficient and θ is the momentum thickness of the wake. Such a dependence was proposed by Schlichting (1960).

Using the approximation that for small wakes the shape factor δ^*/θ is near unity the final wake depth and wake width could be expressed in terms of the initial values as follows.

$$\frac{\beta}{\beta_0} = \left(\frac{U_0}{U}\right)^2 \left[1 + \frac{8\pi^2}{\pi^2 - 4}\left(\frac{\epsilon}{U\theta}\right)\int_{x_0} \frac{U_0}{U} d\left(\frac{\beta_0^2 x}{\theta_0}\right)\right]^{-1/2} \tag{4.2}$$

$$\frac{b}{b_0} = \left(\frac{U_0}{U}\right)^3 \frac{\left(\frac{1}{\beta_0} - \frac{3}{4}\right)}{\left(\frac{1}{\beta_0} - \frac{3}{4}\frac{\beta}{\beta_0}\right)\frac{\beta}{\beta_0}} \tag{4.3}$$

The variable x denotes the streamwise location coordinate and the subscript 0 indicates conditions at the initial wake location. The parameter b is the width of the wake. Although the expressions are restricted to small values of β, comparison with

experiment by Hill et al. (1963) showed that they are useful in the range $0 < \beta_0 < 0.5$. The pressure rise experienced by the wake appears in the equations as the freestream velocity ratio, U_0/U. These equations gave the form of the wake at any downstream station.

For the wake profile assumed, the wake parameters b and β are related to the wake displacement and momentum thicknesses, δ^* and θ, which specify the wake shape. For the wake shape used by Hill et al. (1963),

$$\beta_0 = \frac{4}{3}\left(1 - \frac{\theta_0}{\delta_0^*}\right) \tag{4.4}$$

$$b_0 = \frac{\delta_0^*}{\beta_0} \tag{4.5}$$

The initial wake parameters for input into the expressions for wake growth, Equations 4.2 and 4.3, can be obtained from the integral wake quantities for the wake profile indicated in Figure 4-12.

4.4.3 Overview of simple blockage model

As described in Section 4.3.2 we assume that the low relative total pressure in the clearance vortex is determined by the loss of leakage crossflow. Figure 4-13 shows the development of the velocity profile of the leakage and neighboring passage flow at two locations viewed in a crossflow plane within the blade passage. The velocity at the clearance exit is indicated by the profile shown nearest to the blade. The solid curve represents the velocity magnitude and the dashed curve represents the mainflow component of velocity. The flow leaving the clearance has the same velocity as the passage flow near the suction surface, but the mainflow component of the leakage velocity is considerably less. As the leakage flow penetrates further into the passage all of the leakage crossflow velocity is lost and the leakage jet is effectively a wake. The plausibility of this hypothesis is reinforced by the presence of a relative total pressure defect in the center of the clearance vortex, indicating that there is significant loss as

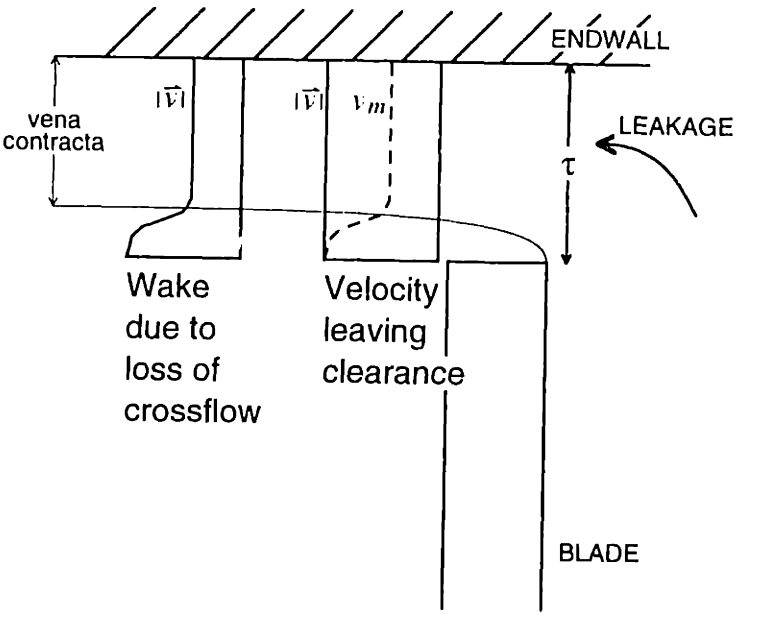

Figure 4-13: Leakage velocity profile development in crossflow plane illustrating development of wake

the leakage flow is turned into the streamwise direction.

The model of Hill et al. (1963) applies to a two-dimensional wake. Figure 4-14 shows how the two-dimensional wake model is applied to the clearance flow in a blade passage. The mainflow velocity defect at the clearance exit is broken up into discrete individual wakes corresponding to neighboring chordwise locations in the computational grid along the blade chord. Each wake is imagined to maintain its integrity[3] and to have its own trajectory as it proceeds downstream. For simplicity the length over which mixing occurs is assumed to be the straight-line distance from clearance exit to mid-passage at the axial location for which blockage is to be calculated.

Each wake is regarded as two-dimensional, i.e., it grows only in the transverse direction and the elemental length, Δl, of each discrete wake is assumed constant. Δl is fixed by two factors as shown in Figure 4-14. The leakage enters the passage along a projected length based on the chordwise length, Δc, and the angle, α, formed by the leakage flow and the tangent to the local blade surface. The expression for the

[3]By "integrity" we mean that the wake is regarded as retaining its structure, unaffected by other wakes or the three-dimensionality of the flow.

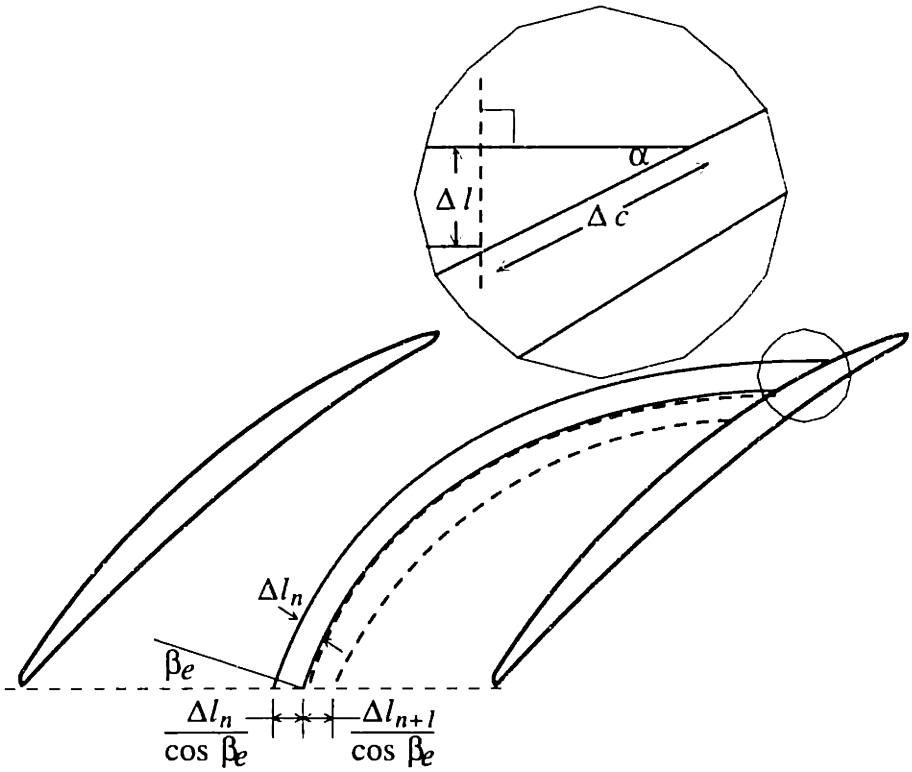

Figure 4-14: Radial view illustrating hypothetical discrete wake to which wake model is applied

wake elemental length is thus

$$\begin{aligned} \Delta l &= \Delta c \cos(90^\circ - \alpha), \\ &= \Delta c \sin \alpha. \end{aligned}$$

The initial wake displacement and momentum thicknesses for each wake originating at the clearance exit is obtained by integrating the defect in mainflow velocity, referenced to the passage velocity near the suction surface outside the blade boundary layer, over the radial extent of the leakage jet. The wake model then gives the final displacement thickness for each wake, given the pressure rise and length over which mixing occurs. The contribution to blocked area in an axial plane due to each wake is

$$\Delta A_b = \delta^*_{final} \Delta l / \cos \beta_e.$$

The reason for dividing by $\cos\beta_e$ can be seen from Figure 4-14. An axial plane intersects the hypothesized wake at the angle, β_e. Thus, the length of the wake in the axial plane is $\Delta l/\cos\beta_e$.

Two elementary wakes (solid and dashed) are indicated in Figure 4-14 and denoted by the indices n and $n+1$, respectively. Summing the blocked area contributions of all wakes originating along the blade surface yields the total blocked area due to clearance.

4.4.4 Implementing the wake model

Issues covered

Having described conceptually the implementation of the wake model to obtain clearance-related blockage, some details will be addressed. These are: (1) obtaining the mainflow velocity profile at each chordwise location along the clearance, (2) obtaining the velocity at the edge of the wake, (3) calculating the pressure gradient for each wake, (4) setting the turbulent mixing coefficient, and (5) applying the model to compressible flows.

Wake velocity profile

The mainflow velocity component is calculated based on the results of Storer and Cumpsty (1991). Using the nomenclature of Figure 4-15,

$$v_m(y) = \sqrt{\frac{2\left(P_t(y) - P_p\right)}{\rho}} \tag{4.6}$$

$P_t(y)$ is known at the grid nodes at the clearance boundary. P_p and P_s are blade surface static pressures a few clearance heights inboard of the blade tip on the pressure and suction sides of the blade, respectively.

The leakage jet forms a vena contracta as it accelerates to match the suction surface pressure. (Only the velocity component normal to the blade, v_n increases —

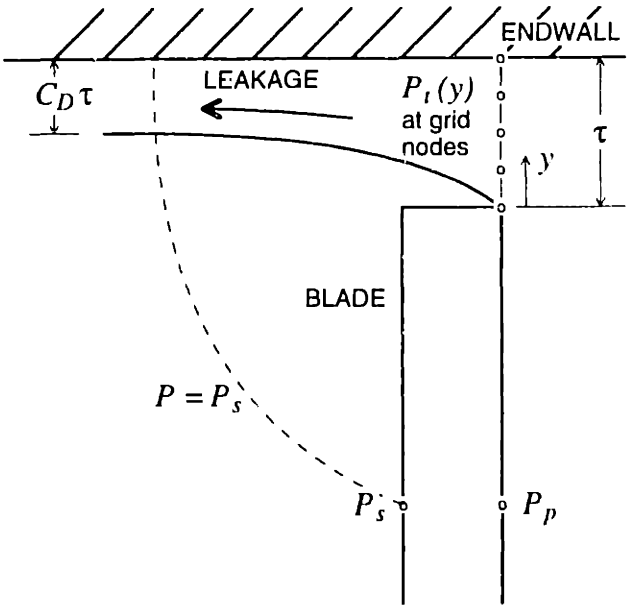

Figure 4-15: Illustration of leakage model used to calculate leakage velocity profile

$v_m(y)$ is determined by $P_t(y)$ and P_p.) Thus, the radial extent of the jet is less than τ when its pressure is P_s. The ratio of the leakage height to the clearance height is the discharge coefficient, C_D, given by Equation 2.1.

Knowing $P_t(y)$ at the entrance to the clearance, P_p, and P_s, the wake displacment and momentum thicknesses can be calculated:

$$\delta^* = C_D \int_{tip}^{wall} \left(1 - \frac{v_m(y)}{v_e}\right) dy, \tag{4.7}$$

$$\theta = C_D \int_{tip}^{wall} \frac{v_m(y)}{v_e} \left(1 - \frac{v_m(y)}{v_e}\right) dy. \tag{4.8}$$

Since the velocity profile is only known at grid nodes, discrete approximations to the integrals in Equations 4.7 and 4.8 are used.

The locations of s and p in Figure 4-15 were obtained as described in Section 2.4.5. If the wake growth were assumed to be inviscid the final displacement thickness would be determined by $P_t(y)$ and the final pressure and would thus be independent of P_s. In the blockage model the wakes are not assumed inviscid, however using a higher value of P_s increases C_D (and thus the initial δ^*) and decreases the pressure rise. The

blocked area is thus not sensitive to the location of P_s.

Wake edge velocity

To obtain the integral wake parameters using Equations 4.7 and 4.8 the reference or edge velocity for the defect is required. For incompressible flow the edge velocity outside the wake can be obtained from the relative total pressure and static pressure there. The region outside the wake does not undergo any loss and its total pressure is taken as the upstream value at the same radius. The pressure P_s, used to specify the initial wake velocity profile, is used to fix the edge velocity, v_e.

Radial distributions of relative total pressure were examined at a tangential distance of approximately two clearance heights away from the clearance exit boundary for the low speed rotor. The results indicate that as the leakage jet mixes, it spreads to a distance of several (two or three) clearance heights from the endwall. Thus, the same distance from the endwall used for P_p and P_s is appropriate to use for the wake edge relative total pressure. The inlet relative total pressure at 3τ from the endwall, $P_{t,3\tau}$ was, therefore, used to specify the wake edge velocity.

Streamwise pressure gradient

In Equation 4.2 the freestream velocity ratio appears within the integral over the streamwise trajectory of the wake. The variation of the freestream velocity along the path traveled by the wake is thus required. We used the simplest description for this, a linear variation in freestream velocity from the initial to final wake locations. The initial velocity (U_0 in Equations 4.2 and 4.3) is the same as the edge velocity, v_e, for the initial wake and the final velocity is obtained by assuming that the relative total pressure at the wake edge does not change and that the downstream pressure is equal to the area averaged pressure over the clearance-related defect region. Thus,

$$\frac{U_0}{U_{final}} = \sqrt{\frac{P_{t,3\tau} - P_s}{P_{t,3\tau} - \overline{P}^a}} \tag{4.9}$$

where $\overline{P}^a$ is the area averaged pressure over the defect region at the axial station at which the blocked area is desired.

Turbulent mixing

Mixing acts over the path traced by the wake and its influence is represented by the integral in Equation 4.2. Hill et al. (1963) used the relationship given by Equation 4.1 with the constant equal to the value proposed by Schlichting (1960) of 0.044. The Navier-Stokes computations with the mixing length turbulence model predicted that the eddy viscosity in the clearance vortex is greater than this value. For the low speed rotor computation with 3.0% clearance and $C_x/U = 0.42$, the turbulent viscosity at midchord in the vortical region near the endwall was such that

$$\frac{\epsilon}{U\theta} = 0.18.$$

with U and θ as the initial wake edge velocity and momentum thickness.

The effect of mixing is largely included in the wake model by the specification that the wake profiles are similar at all downstream locations (for inviscid flow this would not be the case). Thus, the results of implementing the wake model are not expected to be sensitive to the value for the constant in Equation 4.1. Although no survey of the turbulent viscosity for different flow fields was performed, the relationship obtained above was assumed to be representative for flows in the vortex core and was applied when modeling blockage growth for all flow fields. The blockage model results are shown to be insensitive to the value used for $\epsilon/(U\theta)$ in Appendix F.

4.4.5 Compressible flow

The implementation of the wake model as discussed so far pertains to incompressible flow fields. To apply the (incompressible) wake model to the transonic fan flow fields, we must calculate (1) the initial wake parameters and (2) the pressure rise.

The mainflow velocity profile can be obtained by assuming the flow to be compressible. If one assumes that the initial wake fluid has a density equal to the density at location s on the blade (where the near-tip suction surface pressure, P_s, is taken), then the wake velocity profile can be obtained using ρ_s, P_s, P_p, and P_t. The density is assumed to be constant ($= \rho_s$) across the wake and Equations 4.7 and 4.8 are still used to get the initial wake parameters.

The pressure gradient is represented by the freestream velocity ratio in Equations 4.2 and 4.3. The freestream velocity change in the high speed flow fields thus does not represent the pressure rise and should not be used in equations written for incompressible flow. Therefore, the velocity ratio was calculated from the pressure rise as if the flow were incompressible. This "incompressible" velocity ratio is then used in the incompressible wake growth equations.

4.4.6 Results of the simple model

The results of the wake model are summarized in Figure 4-16. Blocked area values are normalized by the same parameters used in Figures 4-8 through 4-11 and are plotted for the same flow fields and locations. Abscissa values for each data point are the same as used in Figure 4-11. Comparison of Figures 4-16 and 4-11 indicates that the trend in blockage predicted by the simple model is in good agreement with the trend obtained with the three-dimensional Navier-Stokes computations. The absolute values predicted by the model are particularly good at high values of the loading parameter.

There are several discrepancies between the wake model and the actual flow situation. The most obvious regards the assumption of wake two-dimensionality. A segment of the wake that forms due to the loss of leakage crossflow momentum does not remain as a coherent structure as it proceeds downstream. The velocity profile becomes skewed as the leakage flow furthest from the endwall interacts most strongly with the passage flow. Furthermore, the presence of the clearance vortex ensures that

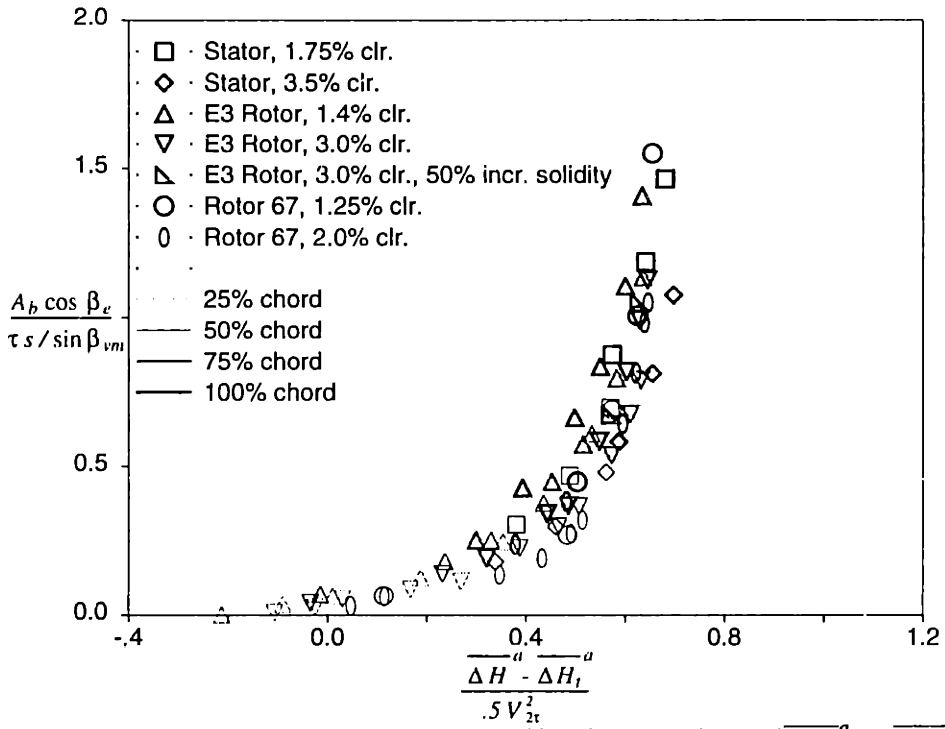

Figure 4-16: Simple model $A_b \cos\beta_e/(\tau s/\sin\beta_{vm})$ vs. $(\overline{\Delta H}^a - \overline{\Delta H_t}^a)/\frac{1}{2}V_{2\tau}^2$

any wake segment does not remain distinct. However, the point of implementing the wake model is *not* to assert that the individual wake segments actually behave as modeled. The important point is rather that the development of blockage can be understood in terms of the growth of a wake and the overall growth of the low energy fluid can be quantified *as if* each wake behaved independently. To put this more succinctly, the purpose of the model is not to simulate the details of the actual flow, but to highlight the essential mechanisms of blockage growth.

Another difference between the model assumptions and the present implementation involves the assumed wake profile. The wake profile indicated in Figure 4-12 is quite different from the profile of v_m at the clearance exit boundary (similar to that shown in Figure 4-13). If the wake growth depends more on integral wake parameters than on details of the wake profile, the important aspects are captured by the displacement and momentum thicknesses for the class of wakes associated with the leakage flow.

A related discrepancy involved the shape factor of the clearance-related wake. Near the midchord location the wake shape factor ranged between 1.4 and 2.0. Even

with these values, however, the wake model was useful for describing blockage generation.

4.5 Conclusions

The most important mechanism of clearance-related blockage has been shown to be the increase in area occupied by low relative total pressure fluid in the adverse pressure gradient of the blade passage. The deceleration of the clearance vortex core was found to depend essentially only on relative total pressure at the vortex roll-up location and pressure rise along the vortex centerline. The swirl velocity did not play a significant part in the vortex growth and the crossflow contribution to the blockage was minor compared to the contribution due to the defect in relative total pressure. The role of the vortical structure is in affecting the rate of mixing of the high loss fluid.

The functional dependence of the blocked area can be expressed as

$$\frac{A_b \cos\beta_e}{\tau s/\sin\beta_{vm}} = f\left(\frac{\overline{\Delta P}^a - \overline{\Delta P_t}^a}{Q_{2\tau}}\right), \tag{4.10}$$

or, more generally,

$$\frac{A_b \cos\beta_e}{\tau s/\sin\beta_{vm}} = f\left(\frac{\overline{\Delta H}^a - \overline{\Delta H_t}^a}{\frac{1}{2}V_{2\tau}^2}\right). \tag{4.11}$$

The clearance-related blocked area thus depends on parameters which are known or can be estimated in the design process.

A simple fluid dynamic model for clearance-related blockage was also developed. The model incorporates the essential features that determine the blockage growth: (1) initial relative total pressure defect, (2) adverse pressure gradient, and (3) turbulent mixing. The wake model of Hill et al. (1963) was implemented to treat the defect due to leakage as a series of two-dimensional turbulent wakes, each with its own pressure gradient and distance over which mixing occurs. In spite of the simplicity of the wake

model and the assumptions required to implement it, the blockage model agreed well with the three-dimensional computations.

Chapter 5

Developing Strategies to Control Endwall Flows

5.1 Introduction

In this chapter we discuss results concerning the mechanisms of blockage presented in Chapter 4. Insights from the parametric dependence will be discussed first and then the implications of the model regarding the mechanisms of blockage growth will be examined. Application of the findings including uses of the parametric dependence and simple model in design practices are proposed.

5.2 Results from Correlation of the Numerical Experiments

The parametric dependence of that has been found for clearance-related blockage can be used to evaluate the influence of energizing the low total pressure that results from the leakage flow. The data of Figure 4-8 relate the normalized blocked area to the sum of pressure rise and loss near the endwall. Increasing the relative total pressure in the clearance-related defect region would be expected to reduce the normalized

blockage according to the trend in the correlation.

Figure 4-8 also indicates that blockage grows more rapidly at increased values of loading parameter. At loading parameters greater than 0.7 the blockage growth with loading becomes quite steep. This suggests that, as a design rule for blading within the parameter range examined here, loading parameter values of this magnitude should be avoided. This loading parameter might be useful to avoid tip critical conditions, playing a role similar to that of the Lieblein (1956) diffusion factor for two-dimensional boundary layer separation on compressor blades. The computational data are too sparse at high values of the loading parameter, however, to determine if there is an asymptotic limit of loading parameter.

The parametric data also indicate that the details of the adverse passage pressure gradient are not important. The normalized blocked area is largely fixed by the overall change in static and relative total pressure near the endwall. This was found for a variety of blade designs, loading conditions, and axial stations. Khalsa (1994) has examined the effect of variations in pressure gradient on wake growth predicted by the model of Hill et al. (1963). For a given overall pressure rise different streamwise pressure distributions, as might be associated with different regions of the passage or differences in blading, changed the ratio of final to initial displacement thickness by a few percent only.

5.3 Results from the Simple Model

Adamczyk et al. (1993) found that by eliminating the clearance on the leading half of the transonic fan geometry examined here (with 1.25% clearance), a higher pressure rise and lower mass flow could be obtained than with the full clearance. When clearance was eliminated over the first 29% chord of the blade, the peak pressure rise was roughly midway between the peak pressure rise values corresponding to full clearance and zero clearance. It was thus suggested that the leading half of the blade

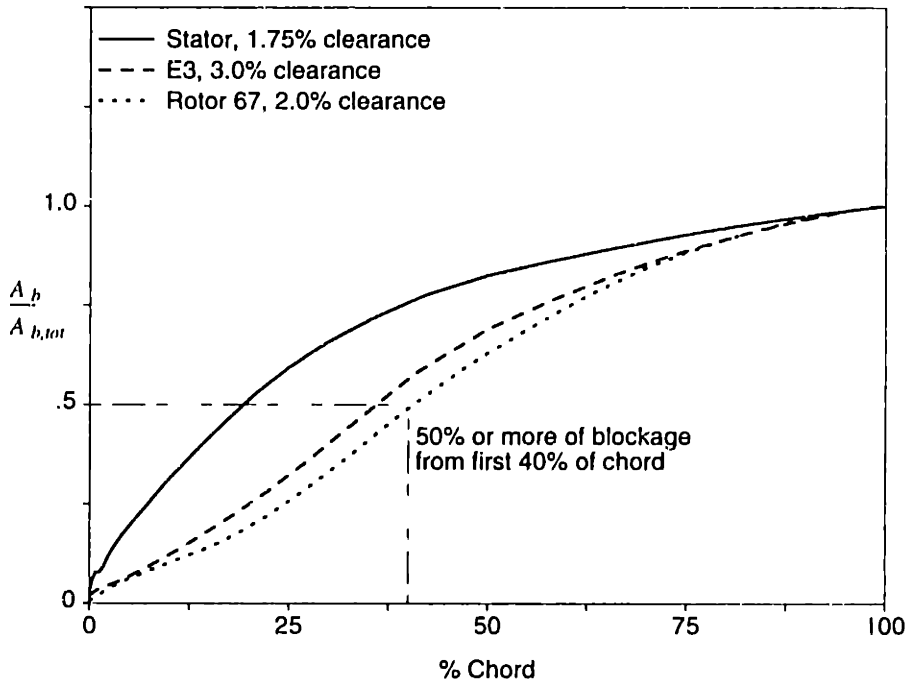

Figure 5-1: Sample distributions of chordwise contribution to trailing edge clearance-related blockage as predicted by the simple model

has a larger contribution to blockage, but the chordwise blockage contribution was not examined explicitly. The blockage model described in Section 4.4 provides a simple means of doing this.

The cumulative contribution to trailing edge blocked area obtained from the simple blockage model for three flow fields is shown in Figure 5-1. Trailing edge blocked area contribution from the leading edge to each chordwise location is normalized by total clearance-related blocked area obtained from the model (the blocked area due to contributions over the entire chordwise extent of the clearance) and plotted against chordwise location from the leading edge. The slope of each curve represents the contribution to blockage per unit chord length. The solid, dashed, and dotted curves correspond to the highest loading flow conditions of the 1.75% clearance stator, 3.0% clearance low speed rotor, and 2.0% clearance transonic fan, respectively.

These results indicate that the majority of the blockage is due to the leakage from upstream of the 40% chord station along the clearance. Reducing the clearance over the leading half of the blade has greater leverage with respect to reducing blockage,

although the contribution due to the leakage from the aft half of the clearance is still significant. The wakes from the clearance in the leading half of the blade undergo greater pressure rise than wakes from the aft half of the blade, but they also experience more mixing. As described in Section 4.2.1, flow visualization indicates that energizing of the low energy fluid in the fluid originating near the tip and leading edge can nearly balance the loss which occurs in the shear layer.

The simple model also suggests that the dissipation of the leakage crossflow largely determines the relative total pressure defect in the vortex core. In the blockage model the leakage velocity component in the mainflow direction is used for the wake velocity profile at a given chordwise location. The kinetic energy associated with the velocity component normal to the mainflow direction is assumed to be lost as the wake is turned into the mainflow direction. The total pressure deficit associated with the wake in the simple model thus corresponds to the total pressure deficit associated with the vortex core before mixing acts to energize the core. It is proposed here, therefore, that a good estimate of the difference between the upstream relative total pressure and that in the vortex core is the crossflow kinetic energy of the leakage flow. Evaluation of this idea in any detail was not carried out in the present investigation.

5.4 Design Applications

The quantity $\tau s/\sin\beta_{vm}$ is the normalizing area for the blocked area in Figure 4-8. For a given loading parameter if one wishes to reduce the blocked area, A_b, one must reduce the normalizing area $\tau s/\sin\beta_{vm}$. Clearance, τ, directly reduces the normalizing area, but presumably the clearance has already been made as small as possible. The other opportunities for reduction in blocked area are: (1) reducing the blade spacing, and (2) increasing the mean flow angle. Reducing the blade spacing or increasing mean flow angle will also tend to reduce the loss contribution to the loading parameter because these changes reduce the blade pressure difference which drives

the leakage flow. Since these changes reduce the loading parameter as well as the normalizing area, they may have high leverage for blockage reduction. The dependence on mean flow angle is consistent with the correlation by Koch (1981) which indicates that increasing the blade stagger leads to enhanced compressor stability.

Epstein (1994) suggested that the simple model could be used by a designer to examine the sensitivity of blockage to aspects of a particular blade design and to investigate tradeoffs. For example, after obtaining model results for a given baseline design, the model could be used to compare the effects of changes in clearance and changes in pressure rise. One advantage of the simple model over the parametric curve for this purpose is that the blocked area can be obtained without knowledge of the relative total pressure loss near the endwall.

Another potential use for the blockage model is to predict off-design effects of tip clearance. The pressure rise for a compressor passage may be known at a particular operating point, but the effect of changes in flow rate, blade speed, or inlet profile on pressure rise might be unknown. In this case the change in clearance-related blockage would be of interest. If the effect of the off-design operating point on the loading parameter and freestream flow angles can be calculated or estimated, the blockage correlation or simple model can be used to obtain the change in blockage associated with the change in operating point.

It has not been determined whether the parametric dependence is general enough to include endwall flows with casing treatment, but the relationship between normalized blocked area and loading parameter should still provide a useful framework to evaluate casing treatment. Lee and Greitzer (1990) found that the increase in stalling pressure rise which accompanied endwall injection correlated well with the streamwise momentum of the injected flow. The relative total pressure increase in the endwall region due to the injection should be related to the streamwise momentum. Similarly, flow removal from the endwall region results in an increase in the average relative total pressure. If the increase in relative total pressure due to the injection

and removal of flow associated with casing treatment is known, locating the resulting loading parameter on the parametric curve provides a quantitative assessment of the change in blocked area. Thus, if analysis or experiment reveals the streamwise momentum injection due to different casing treatments, the correlation might be useful to predict the effect of casing treatment designs.

An additional benefit of either the correlation or the wake model would be obtained if it could be used in existing compressor design systems. Typical design methods involve an axisymmetric streamline curvature calculations which rely on empirical models for blockage. Dring et al. (1983) have pointed out that "the limiting feature in the accuracy of a through-flow analysis is not so much the numerics but rather in the aerodynamic data that the analysis requires as input." They further state, "Errors in estimated blockage are one of the primary reasons for compressors initially not achieving their design goals of flow, pressure rise and efficiency."

In a design system blockage due to the blade boundary layers and the flow near the endwall opposite the tip would be obtained separately from that due to clearance. The simple blockage model might thus be applied in a design system as follows.

1. An initial pass of the streamline curvature calculation would yield velocity triangles for the streamline nearest to the tip. These triangles would be used to obtain the pressure difference which drives the leakage flow.

2. The tip chordwise pressure distribution and clearance discharge coefficient are assumed and the inlet relative total pressure near the tip estimated.

3. The simple model would then be used to calculate the tip region blocked area at the trailing edge of the passage.

4. The blocked area is then converted into a displacement thickness for the casing "boundary layer" by dividing the blocked area by the tangential blade spacing at the tip. This displacement thickness reduces the annular area and increases

the core region velocity obtained by subsequent iterations of the streamline curvature procedure.

The loss model of Storer and Cumpsty (1993) can make use of some of the same inputs as the blockage model utilizes: clearance height, blade loading, and inlet conditions to the blade row. Both models share the common feature of being physically-based models for the flow (rather than empirical correlations) and they could be used simultaneously in the design procedure procedure described above.

Chapter 6

Conclusions and Recommendations for Future Work

6.1 Summary

Three-dimensional Navier-Stokes computations have been used to investigate the effects of tip clearance on axial compressor pressure rise. Clearance has been shown to be a dominant factor in determining the endwall flow structure.

A definition for blockage in axial compressors has been developed. The mainflow component of velocity, i.e., the component in the neighboring freestream direction, is the relevant velocity component for use in the definition. The edge of the velocity defect is determined by using the gradient of this velocity component. Clearance-related blockage was calculated in flow fields in which the defect region associated with leakage, i.e. the clearance vortex, could be identified, for a low speed rotor and a transonic fan.

The principal mechanism of blockage generation was found to be the growth of streamtubes with low relative total pressure fluid. Further, the low total pressure

resulted from loss as the leakage flow enters the passage. This loss occurs as a result of the interaction between the leakage flow and the passage flow. Flow visualization showed that the growth of the vortex core was largely determined by its relative total pressure at the point of roll-up and the pressure rise along the core.

The main effect of the clearance vortical structure was the influence on mixing. More specifically, swirl ratios of the leakage vortices were considerably less than the values typically associated with "vortex breakdown." The flow angularity contribution to blockage was also found to be minor. The vortical structure was critical, however, in identifying the clearance-related defect region so that the related blocked area could be quantified.

The parametric dependence of clearance-related blockage was found to collapse well when plotted in terms of normalized blocked area parameter versus a static and total pressure loss parameter as shown in Figures 4-8 and 4-11. The loading parameter used in the latter figure is the more appropriate one for high speed flows.

A simple model for blockage was developed using a description of the growth of a two-dimensional turbulent wake in an adverse pressure gradient. In this, the wake profile for discrete segments along the chord is obtained from the mainflow component of the leakage velocity, each discrete wake is analyzed using the two-dimensional wake model, and the areas associated with each wake are summed to yield the blocked area.

The simple model, which gave blockage values in good agreement with the three-dimensional computations, provides insights as to the important processes associated with blockage growth. The overall passage pressure rise is an important parameter, the details of the pressure distribution being relatively unimportant. Hence whether the pressure gradient arises from passage diffusion or shocks is not critical for blockage. The model also highlights the importance of the relative total pressure defect in establishing the blockage. The ability of the model to capture the blockage trends obtained from the three-dimensional computations suggests that the defect in the vortex core can be quantified by the same mechanism used to obtain the wake defect

in the model, i.e., dissipation of the crossflow component of the leakage.

From a design perspective, the parametric dependence and the simple model allow a designer to examine, in terms of blockage, the effect of varying a given design parameter. The correlation of normalized blocked area indicates that a limiting value of the loading parameter can be specified as a design criterion for compressor stability. Further, the design parameters can be chosen so as to minimize the blockage for a given loading parameter. The model or the correlation of numerical results could also be incorporated into the overall compressor design system so that physically based blockage values can be used to predict performance.

6.2 Conclusions

The functional dependence of the blocked area can be expressed as

$$\frac{A_b \cos\beta_e}{\tau s/\sin\beta_{vm}} = f\left(\frac{\overline{\Delta P}^a - \overline{\Delta P_t}^a}{Q_{2\tau}}\right), \tag{6.1}$$

or, more generally,

$$\frac{A_b \cos\beta_e}{\tau s/\sin\beta_{vm}} = f\left(\frac{\overline{\Delta H}^a - \overline{\Delta H_t}^a}{\frac{1}{2}V_{2\tau}^2}\right). \tag{6.2}$$

The clearance-related blocked area thus depends on parameters which are known or can be estimated in the design process.

Clearance-related blockage is not sensitive to details of pressure gradient or loss, but is primarily determined by the overall pressure rise and loss which occurs near the endwall.

The mechanism of blockage which is of primary importance is the response of the low total pressure fluid (associated with the leakage process) to the passage pressure rise. The simple model for blockage suggests that leakage crossflow largely determines the total pressure in the vortex core.

Modifying the details of the flow, such as tailoring the pressure gradient, is not likely to significantly affect blockage due to tip clearance — the blockage is largely determined by more global parameters. However, energizing the clearance vortex core has good potential to reduce blockage.

6.3 Recommended Future Work

All the flow fields used in this investigation were obtained from a computational code. Detailed measurements from physical experiments should be obtained to check the ability of the parametric curve and blockage model to capture experimental trends. The range of applicability of the parametric trend and simple model should also be examined further. For example, clearance-related blockage for blade rows with clearances less than 1.25% of chord (the minimum clearance used), but still large enough to produce a well-defined clearance vortex should be obtained using the quantification method described in Chapter 3 and using the simple model.

The correlation developed in Section 4.3 suggests a limiting loading parameter for endwall flows with tip clearance. Koch (1981) related stage pressure rise capability to blade parameters and inlet flow conditions for a large amount of experimental data. The present work should be adapted so it can be expressed in terms of the stalling pressure rise in Koch's correlation. Examination of the agreement between the correlation developed in this work and that developed by Koch using experimental data would be very useful not only as a design guideline, but in tying the present results more closely to experiment.

The $\overline{\Delta P_t}^a$ term in the loading parameter used in Figure 4-8 has been taken as an independent input. The simple model for blockage indicates that the reduced total pressure in the clearance vortex is due to the loss of leakage crossflow momentum. A general relationship between $\overline{\Delta P_t}^a$ and the blade loading, $\Delta_B P$ should be developed so that the former can be estimated rather than measured or calculated from the

three-dimensional flow field. This would mean that fewer independent inputs would be required to specify the normalized blocked area since, as shown in Section 4.3.2, the blade loading is also related to the passage pressure rise via the blade geometry.

To use the parametric curve in the design of casing treatment the effect on the loading parameter needs to be established. The effect of flow injection and removal on blockage, the change in relative total pressure in the endwall region, and the loading parameter should be investigated. Numerical computations provide a means of carrying out such an investigation.

The flow fields examined were for isolated blade rows. Work is required to determine how the ideas developed using this framework carry over into the multistage environment. (This is related to the connection with Koch's work.)

Use of the blockage model would be even simpler if the chordwise pressure distribution near the blade tip were not required. The effect of using an average blade pressure difference or a simple chordwise profile (e.g. triangular) should be examined. This would indicate how useful the model can be in the preliminary design phase.

The final objective of this work was to produce tools which improve predictive and design practices for axial compressors. The parametric dependence and simple model for clearance-related blockage developed can enable a designer to rationally, and in a quantitative manner, investigate the limits on pressure rise due to endwall blockage. The results also provide a framework for evaluating of strategies designed to alter the endwall flow, such as casing treatment, by examining their effect on blockage.

References

Adamczyk, J. J., Celestina, M. L., Beach, T. A., and Barnett, M., 1989, "Simulation of Three-Dimensional Viscous Flow within a Multistage Turbine," ASME Journal of Turbomachinery, Vol. 112, pp. 370–376.

Adamczyk, J. J., 1992, Personal communication.

Adamczyk, J. J., Celestina, M. L., and Greitzer, E. M., 1993, "The Role of Tip Clearance in High-Speed Fan Stall," ASME Journal of Turbomachinery, Vol. 115, pp. 28–38.

Baldwin, B. and Lomax, H., 1978, "Thin Layer Approximation and Algebraic Model for Separated Turbulent Flows," AIAA Paper No. 78-257.

Brookfield, J. M., 1993, "Vortical Flows in an Adverse Pressure Gradient," M. S. Thesis, Department of Aeronautics and Astronautics, Massachusetts Institute of Techology.

Celestina, M. L., 1992, Personal communication.

Chen, G. T., Greitzer, E. M., Tan, C. S., and Marble, F. E., 1991, "Similarity Analysis of Compressor Tip Clearance Flow Structure," ASME Journal of Turbomachinery, Vol. 113, pp. 260–271.

Cheng, P., 1982, "Effects of Compressor Hub Treatment on Stator Stall and Pressure Rise," MIT Cambridge, Mass., GT&PDL Rep. 167.

Cheng, P., Prell, M. E., Greitzer, E. M., and Tan, C. S., 1984, "Effects of Compressor Hub Treatment on Stator Stall and Pressure Rise," AIAA Journal of Aircraft, Vol. 21, No. 7, pp. 469–475.

Crook, A. J., 1989, "Numerical Investigation of Endwall/Casing Treatment Flow Phenomena," M. S. Thesis, Department of Aeronautics and Astronautics, Massachusetts Institute of Technology, pp. 14–21.

Crook, A. J., Greitzer, E. M., Tan, C. S., and Adamczyk, J. J., 1993, "Numerical Simulation of Compressor Endwall and Casing Treatment Flow Phenomena," ASME Journal of Turbomachinery, Vol. 115, pp. 501–512.

Cumpsty, N. A., 1989, *Compressor Aerodynamics*, Longman Scientific and Technical Publications.

Dawes, W. N., 1987, "A Numerical Analysis of the Three-Dimensional Flow in a Transonic Compressor Rotor and Comparison with Experiment," ASME Journal of Turbomachinery, Vol. 109, pp. 83–90.

Dawes, W. N., 1992, Personal communication.

Dimotakis, P., 1989, "Turbulent Free Shear Layer Mixing," AIAA-89-0262.

Dring, R. P., Joslyn, H. D., and Wagner, J. H., 1983, "Compressor Rotor Aerodynamics," AGARD Conference *Viscous Effects in Turbomachines*, Copenhagen, CP351.

Dring, R. P., 1984, "Blockage in Axial Compressors," ASME Journal of Engineering for Gas Turbines and Power, Vol. 106, No. 3, pp. 712–714.

Epstein, A. H., 1994, Personal communication.

Haimes, R. and Giles, M., 1991, "Visual3: Interactive, Unsteady, Unstructured Three-Dimensional Visualization," AIAA Paper No. 91-0-794.

Hill, P. G., Schaub, U. W., and Senoo, Y., 1963, "Turbulent Wakes in Pressure Gradients," ASME Journal of Applied Mechanics, December, pp. 518–524.

Jameson, A., Schmidt, W., and Turkel, E., 1981, "Numerical Solutions of the Euler Equations by Finite Volume Methods Using Runge-Kutta Time-Stepping Schemes," AIAA-81-1259.

Johnson, M. C., 1985, "The Effects of Hub Treatment on Compressor Endwall Flowfields," M. S. Thesis, Department of Aeronautics and Astronautics, Massachusetts Institute of Technology.

Johnson, M. C., and Greitzer, E. M., 1987, "Effects of Slotted Hub and Casing Treatments on Compressor Endwall Flow Fields," ASME Journal of Turbomachinery, Vol. 109, pp. 380–387.

Khalsa, A. S., 1994, Personal communication.

Kirtley, K. R., Beach, T. A., and Adamczyk, J. J., 1990, "Numerical Analysis of Secondary Flow in a Two-Stage Turbine," Paper No. AIAA-90-2356.

Kirtely, K. R., 1990, Personal communication.

Koch, C. C., 1981, "Stalling Pressure Rise Capability of Axial Flow Compressor Stages," ASME Journal of Engineering for Power, Vol. 103, pp.645–656.

Lakshminarayana, B., and Horlock, J. H., 1962, "Tip-Clearance Flow and Losses for an Isolated Compressor Blade," Aeronautical Research Council of Great Britain, R & M 3316.

Lee, N. K. W., and Greitzer, E. M., 1990, "Effects of Endwall Suction and Blowing on Compressor Stability Enhancement," ASME Journal of Turbomachinery, Vol. 112, pp. 133–144.

Lieblein, S., 1956, "Experimental Flow in Two-Dimensional Cascades," Chapter VI of *The Aerodynamic Design of Axial Flow Compressors*, Reprinted NASA SP-36 in 1965, (originally NACA RME 56B03).

O'Sullivan, M. N., 1993, "A Computational Study of the Effects of Viscosity on Lobed Mixer Flowfields," M. S. Thesis, Department of Aeronautics and Astronautics, Massachusetts Institute of Techology, p. 42.

Rhoden, H. G., 1952, "Effects of Reynolds Number on the Flow of Air through a Cascade of Compressor Blades," Aeronautical Research Council of Great Britain, R & M 2919.

Schlichting, H., 1960, *Boundary Layer Theory*, McGraw-Hill Book Company, Inc., New York, N. Y.

Smith, G. D. J. and Cumpsty, N. A., 1984, "Flow Phenomena in Compressor Casing Treatment," ASME Journal of Engineering for Gas Turbines and Power, Vol. 106, No. 3, pp. 532–541.

Smith, L. H., Jr., 1970, "Casing Boundary Layers in Multistage Axial-Flow Compressors," Flow Research on Blading, ed., L. S. Dzung, Elsevier, Amsterdam.

Smith, L. H., Jr., 1994, Personal communication.

Storer, J. A. and Cumpsty, N. A., 1991, "Tip Leakage Flow in Axial Compressors," Journal of Turbomachinery, Vol. 113, pp. 252–259.

Storer, J. A. and Cumpsty, N. A., 1993, "An Approximate Analysis and Prediction Method for Tip Clearance Loss in Axial Compressors," ASME paper No. 93-GT-140.

Strazisar, A. J., Wood, J. R., Hathaway, M. D., and Suder, K. L., 1989, "Laser Anemometer Measurements in a Transonic Axial-Flow Fan Rotor," NASA TP 2879.

Wisler, D. C., 1977, "Core Compressor Exit Stage Study, Volume I — Blading Design," NASA CR-135391.

Wisler, D. C., 1981, "Core Compressor Exit Stage Study, Volume IV — Data and Performance Report for the Best Stage Configuration," NASA CR-165357.

Appendix A

The Effect of Clearance on Blade Bound Circulation and Shed Vortex Circulation

The measured clearance vortex circulation is usually not found to equal the midspan blade bound circulation. Navier-Stokes computations of the flow within a blade passage with tip clearance are used here to illustrate the physical basis for this observation.

Figure A-1 shows static pressure coefficient, C_P, on the blade suction surface for the low speed rotor for (a) 1.4 and (b) 3.0% clearance, both with $C_x/U = 0.42$. Increasing clearance results in a reduction in suction surface pressure near the clearance vortex roll-up location, hence increased blade loading near the tip.

The effect of clearance on blade loading can also be seen by examining the radial distribution of circulation calculated around closed contours around the blade. Figure A-2 shows circulation calculated around constant-radius contours at 50% pitch from the blade surfaces and 3% chord upstream and downstream of the blade. The solid and dashed curves correspond to the flow fields of Figure A-1a and b, respectively. With the increased clearance there is an increase in peak circulation calculated

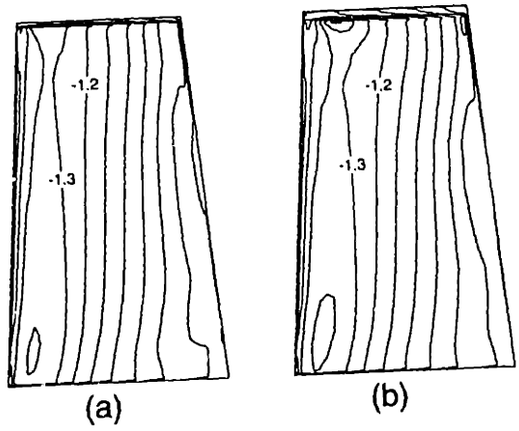

Figure A-1: Suction surface C_P for low speed rotor at $C_x/U = 0.42$ for (a) 1.4 and (b) 3.0% chord

around the blade in the endwall region.

The increased blade loading near the tip due to clearance can be understood by examining the effect of blockage. Increasing the clearance increases the blockage in the endwall region which implies a reduced relative velocity magnitude. The reduction in the tangential component of the passage exit velocity near the endwall contributes to an increase in circulation (since the difference between inlet and exit tangential components of velocity increases), hence the increase in peak circulation near the endwall with clearance shown in Figure A-2. Increased blade bound circulation near the tip implies that the shed circulation into the clearance vortex must increase. The increased vortex strength is accompanied by an reduction in the suction surface static pressure near the vortex roll-up locaton.

The above description of changes in the endwall flow field with clearance provides one explanation for the increase in measured clearance vortex circulation with increased clearance which has been noted by Lakshminarayana and Horlock (1962). Smith (1994) has addressed the fluid dynamic basis for the difference between the

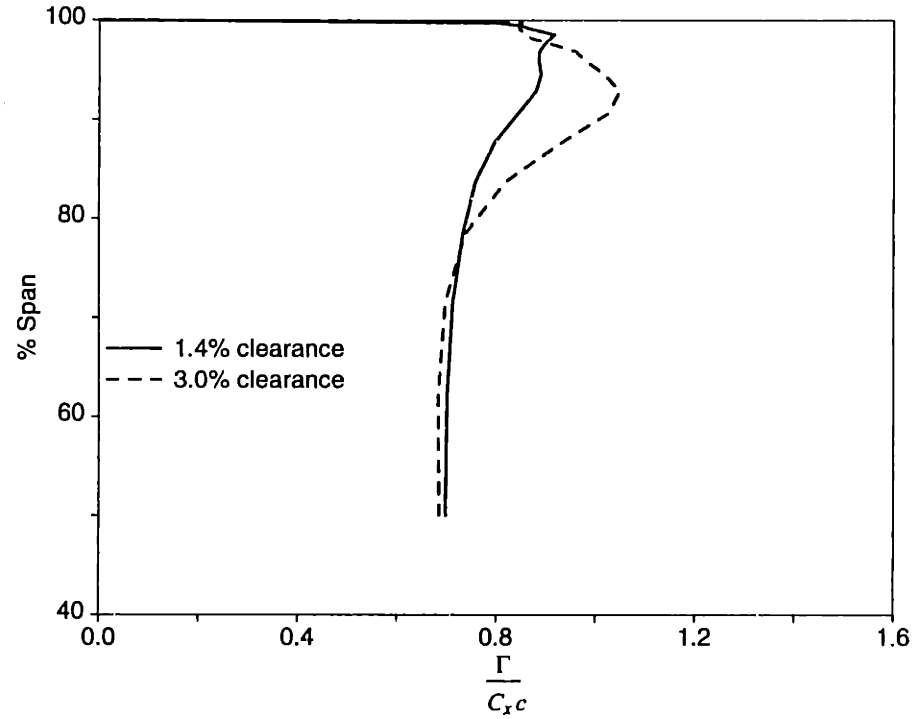

Figure A-2: Radial distribution of $\Gamma/C_x c$ for contour extending 3% chord upstream and downstream and 50% pitch from blade for low speed rotor with $C_x/U = 0.42$ for 1.4 and 3.0% clearance

blade bound circulation (at midspan) and the circulation shed into the clearance vortex. Other factors affecting the measured vortex circulation are addressed in Appendix B.

The increase in blade bound circulation near the tip compared to midspan is actually greater than indicated in Figure A-2. The circulation values shown in Figure A-2 are good assessments of the blade bound circulation at radial locations near midspan, but not in the tip region. The solid curve in Figure A-3 indicates the radial distribution of circulation using closed contours at 11.5% rather than 50% pitch from the blade surfaces for the 3.0% clearance low speed rotor. The dashed curve is the same as that shown in Figure A-2.

Changing the pitchwise extent of the closed contour has little effect on the calculated circulation near midspan, but has a pronounced effect near the tip. This difference between the solid and dashed curves in Figure A-3 is due to radial orientation of vortex lines which are shed from the tip. (This also explains the presence of net circulation for contours around the clearance gap, i.e. at radii between the tip and

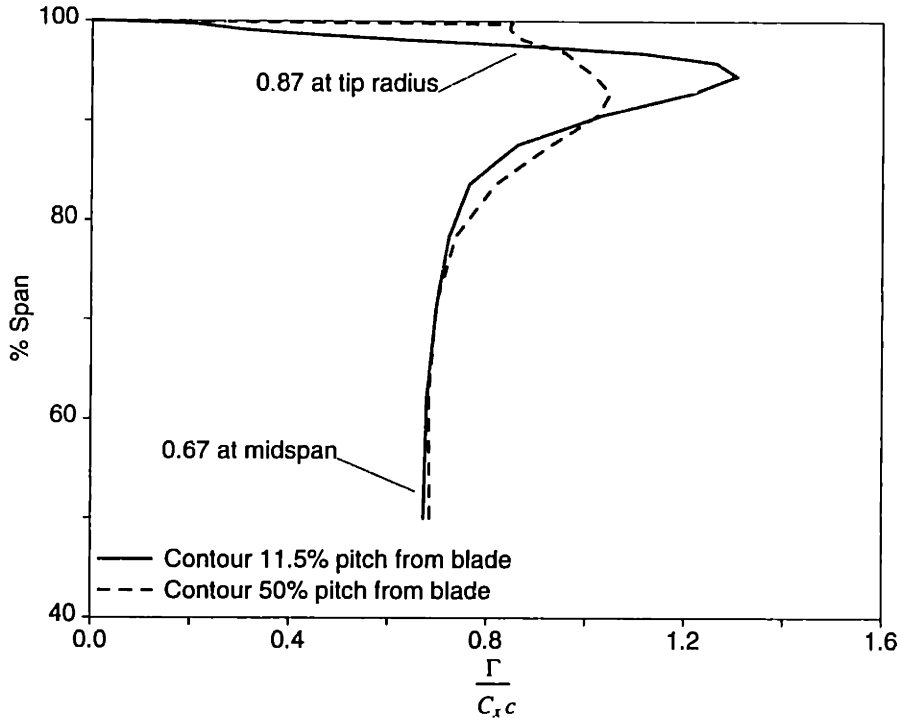

Figure A-3: Radial distribution of $\Gamma/C_x c$ for contour which extends 11.5 and 50% pitch from blade for low speed rotor with $C_x/U = 0.42$ and 3.0% clearance

endwall in Figure A-3.) The shed vortex lines acquire a radial orientation because of the diffusion of vorticity in the shear layer which forms between the passage flow and leakage, as discussed in Appendix B. The contour used to obtain the solid curve is a good representation of the blade bound circulation for all spanwise locations since it encloses the blade boundary layers, but for the most part it excludes the clearance vortex. The blade bound circulation at roughly one clearance height inboard of the tip is roughly a factor of two greater than the midspan bound circulation. The bound circulation which must be shed from the blade tip is indicated in Figure A-3.

The increase in bound circulation and blade pressure difference near the tip with increased clearance might lead one to believe that the leakage velocity increases with clearance. However, this was not found to be the case. The leakage mass flow scaled with clearance for the two flow fields represented in Figure A-1. In Section 2.4.5 the location 2τ inboard of the blade tip was shown to be appropriate to obtain the pressure difference which drives the leakage flow. In Figure A-4 the chordwise distribution of blade surface pressure at that radial location is shown for the flow

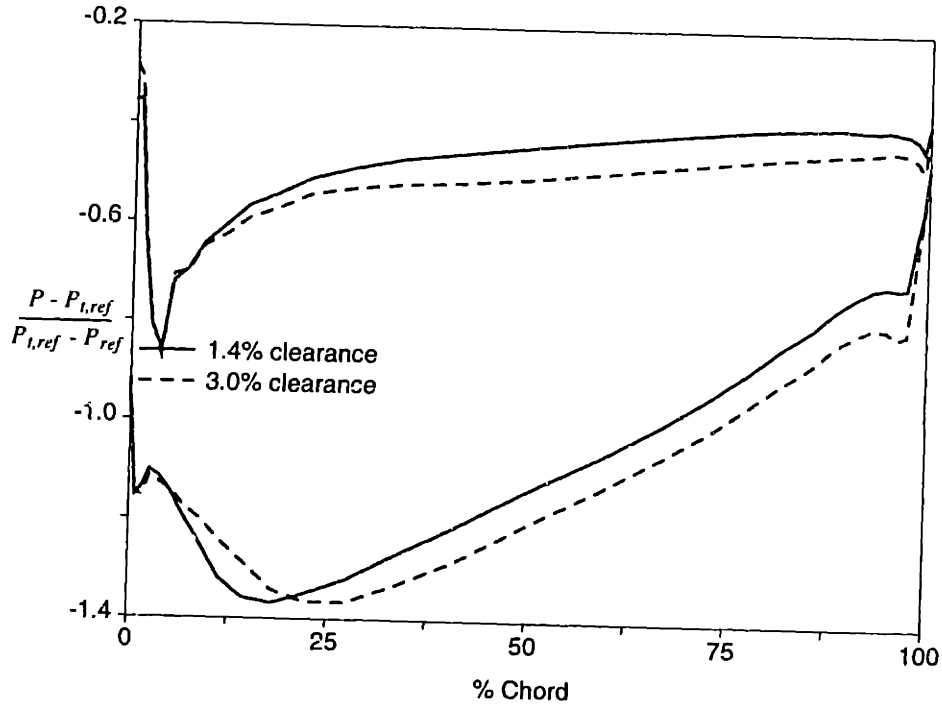

Figure A-4: Chordwise distribution of blade surface C_P at 2τ inboard of tip for low speed rotor with $C_x/U = 0.42$ for 1.4 and 3.0% clearance

fields shown in Figure A-1. The solid and dashed curves correspond to 1.4 and 3.0% clearance, respectively. The blade pressure difference over most of the chord length is roughly the same for the two clearances. The reduced suction surface pressure due to increased vortex strength is thus a localized effect with little influence on the leakage flow.

In summary, the blade bound circulation near the tip increases with increased clearance. As a result of the increased tip loading with increased clearance the shed circulation into the clearance vortex increases. Hence, attempts at comparing the clearance vortex circulation to the blade bound circulation at midspan are not well founded. *The computational results indicate that this effect is consistent with the increase in endwall blockage that accompanies increased tip clearance.* It is also shown that the increase in blade bound circulation does not imply an increase in the pressure difference which drives the leakage flow.

Appendix B

Factors Affecting Measured Vortex Circulation

B.1 Introduction

Several researchers have attempted to measure the circulation in the clearance vortex of a turbomachine blade passage and a common result is that the measured clearance vortex circulation is less than the bound circulation on the blade. Lakshminarayana and Horlock (1962) proposed that this observation is due to "retained lift." They suggested that only a fraction of the bound circulation is shed from the blade tip. However, Storer and Cumpsty (1991) showed that for typical clearances the leakage flow is essentially irrotational. If so, vortex lines from the blade cannot span the leakage jet and thus all of the circulation must be shed. Nevertheless, it will be shown below that there is no reason to expect the measured clearance vortex circulation to equal the circulation shed from the blade tip, or for that matter, the blade bound circulation.

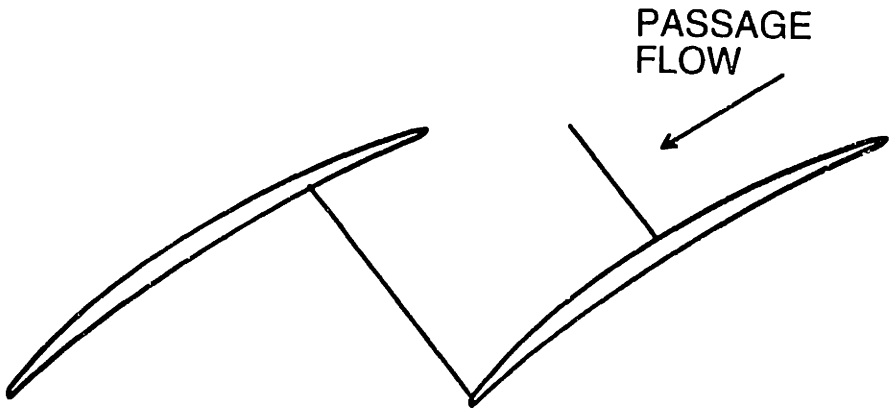

Figure B-1: Radial view of blade passage with midchord and trailing edge crossflow planes.

B.2 The Tip Region Vorticity Field

To determine the factors that affect the circulation measured in a plane intersecting the trailing edge of a blade passage we will consider the vorticity field near the blade tip. Figure B-1 shows a radial view of an axial compressor blade passage with two crossflow planes oriented normal to the blade stagger. One crossflow plane intersects the suction surface at midchord. The other crossflow plane intersects the suction surface at the trailing edge. The midchord plane will be used to illustrate the vorticity distribution near the tip at a typical chordwise location along the blade. The trailing edge plane will be used for the calculation of the clearance vortex circulation since such a plane must be located downstream of all locations along the blade tip from which bound vorticity is shed. The contour around which the clearance vortex circulation will be calculated is located in the trailing edge plane. The blade boundary layers will be not be enclosed by the contour.

The component of vorticity relevant for the measurement of circulation in a given plane is the component normal to that plane. Figure B-2 shows a sketch of the dis-

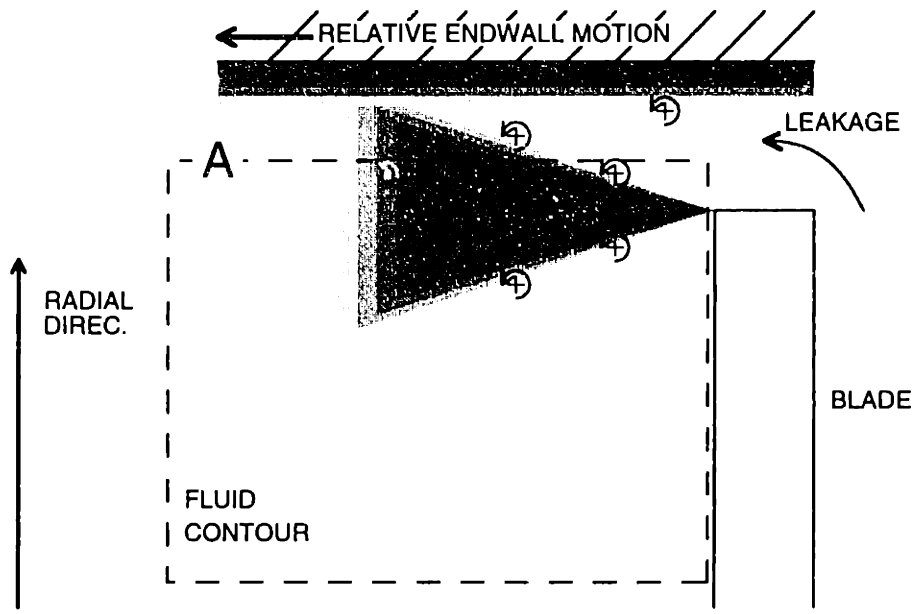

Figure B-2: Sketch of ω_γ distribution near tip in midchord crossflow plane. Trailing edge contour for circulation measurement also shown.

tribution of the vorticity component along the stagger, ω_γ, in the midchord crossflow plane. Greater ω_γ strength is indicated by darker gray shading. A contour in the *trailing edge* crossflow plane around which one might calculate the clearance vortex circulation is superimposed. The segment of the contour, labeled A, which is nearest to the endwall would typically be placed at a radius between the blade tip and the endwall radii. The radius of segment A would be made greater than the tip radius in an attempt to enclose the vorticity shed from the tip, but less than the endwall radius to avoid measuring a circulation due to the motion of the endwall relative to the blade.

The shear layer between the leakage and passage flow which contains the vorticity shed from the blade tip spreads due to turbulent diffusion. There may also be vorticity generated at the endwall which diffuses into the passage flow. Since the spreading angle for a turbulent free shear layer is larger than that for a wall bounded layer, one should expect that the vorticity diffusion from the blade tip region penetrates the region between the blade tip and the endwall faster than the vorticity diffusing from

the wall. Thus, regardless of the sign of the streamwise vorticity generated at the endwall, it is possible for vorticity shed from the blade tip to reach the trailing edge plane between segment A and the endwall (so some vorticity shed from the blade tip would not be enclosed by the contour). Since the radial velocities near the endwall are small, turbulent diffusion would be expected to be important in the vorticity transport near the endwall. Note that, for compressors, the vorticity generated at the endwall can contribute circulation of the same sign as circulation shed from the blade tip.

Consider the circulation calculated along the dashed contour shown in Figure B-2. The midchord plane ω_γ distribution will be taken as representative of the vorticity field that reaches the downstream contour. The circulation obtained using the contour depends on the radial location of segment A. If segment A is positioned as shown in Figure B-2 such that the some of the vorticity shed from the blade tip is not enclosed by the contour, circulation around the contour will be less than the circulation shed from the blade tip. If the radius of segment A is increased such that vorticity generated at the endwall is enclosed by the contour, the circulation value obtained cannot represent the circulation shed from the blade tip.

In Figure B-3, the range of circulation values that can be obtained with different trailing edge crossflow plane contours is indicated qualitatively as a function of radial placement of segment A of the downstream contour. If we assume that the spreading of the shear layer is equal in both radial directions, for segment A at the tip radius the circulation around the contour is half the circulation shed from the blade tip. As the radius of segment A is increased the measured circulation increases. As long as the contour does not enclose all the vorticity shed from the blade tip and excludes the vorticity generated at the endwall, the measured circulation will be less than circulation shed from the blade tip.

In the situation illustrated in Figure B-2, the vorticity field of the free shear layer merges with the vorticity field at the endwall. In this case the measured circulation

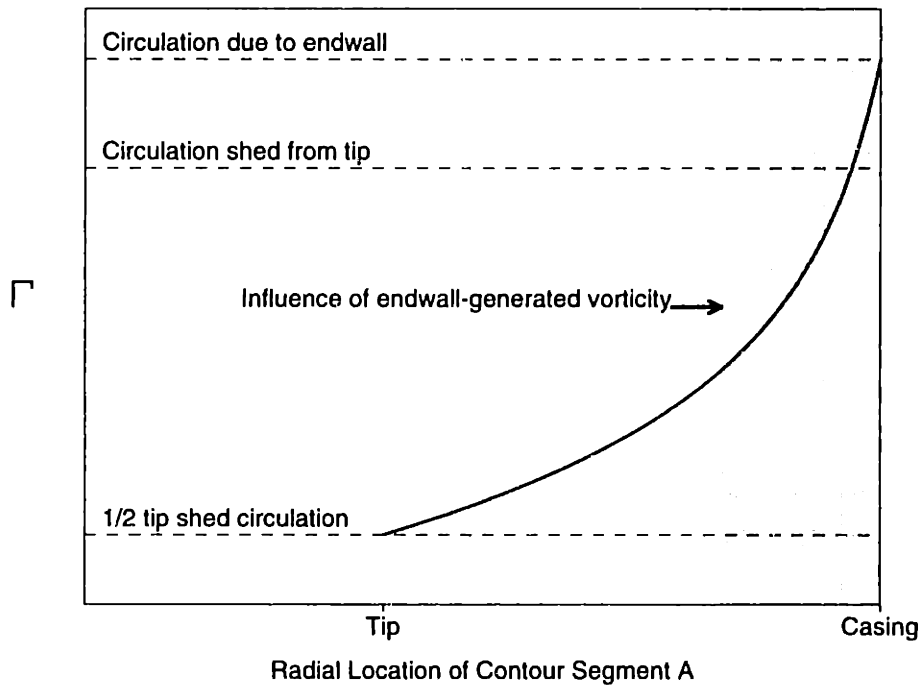

Figure B-3: Sketch of circulation as a function of radial placement of downstream contour used to measure clearance vortex circulation.

cannot increase to the value shed from the blade tip until vorticity associated with the endwall is included within the contour. Even when segment A is positioned such that the circulation around the contour is the same as that shed at the blade tip this circulation is not a measure of the shed circulation alone. The range of radii for which vorticity generated at the endwall influences the circulation calculation is indicated by the shaded region in Figure B-3.

For compressors when the radius of segment A equals the endwall radius the measured circulation exceeds the blade circulation. Neglecting any contribution along the contour except from segment A, the circulation equals the product of the relative wall speed resolved along segment A and the length of segment A.

A range of measured vortex circulation values can thus be obtained depending on the radial position of the contour around which the measurement is taken. If there were an irrotational region extending across the passage between the shear layer and the endwall, a contour could be chosen for which the measured circulation is equal to the circulation shed from the blade tip. However, as will be shown below, an unusually large tip clearance would be required for an irrotational region to separate

the vorticity shed from the tip from the vorticity generated at the endwall. Reducing the clearance would tend to reduced the measured circulation for a given distance of segment A from the endwall since bringing the tip closer to the endwall would result in less of the shed circulation being enclosed by the contour.

For turbines or stationary cascades the same general considerations apply to the discrepancy between the blade bound and measured clearance vortex circulation. However, including the endwall in the contour used to obtain the vortex circulation would yield opposite sign circulation (compared to the sign of the shed circulation) for a turbine, and zero circulation for a stationary cascade.

B.3 Computational Results

B.3.1 Description of the computations

Tne trends described above are illustrated below using a three-dimensional computation. A numerical simulation of a low speed rotor passage was obtained using a three-dimensional Reynolds-averaged Navier-Stokes flow solver developed by Adamczyk et al. (1989). The Navier-Stokes solver uses a mixing length turbulence model appropriate for wall bounded flows. The geometry is the General Electric low speed E^3 Rotor B, described by Wisler (1977). The blade row has a clearance of 3% of chord and a flow coefficient of 0.42. The inlet conditions used are described by Wisler (1981) for the Rotor B/Stator B single-stage configuration near design conditions. The tip of the blade was located at 97.5% of span.

B.3.2 Vorticity field and circulation

Contours of $\omega_\gamma/(C_x/c)$ in the midchord crossflow plane indicated in Figure B-1 are shown in Figure B-4. The two sources of vorticity described in Section B.2 are evident in Figure B-4: (1) vorticity shed from the blade tip which resides in the free shear layer, and (2) vorticity generated at the endwall. The ω_γ generated at the endwall is

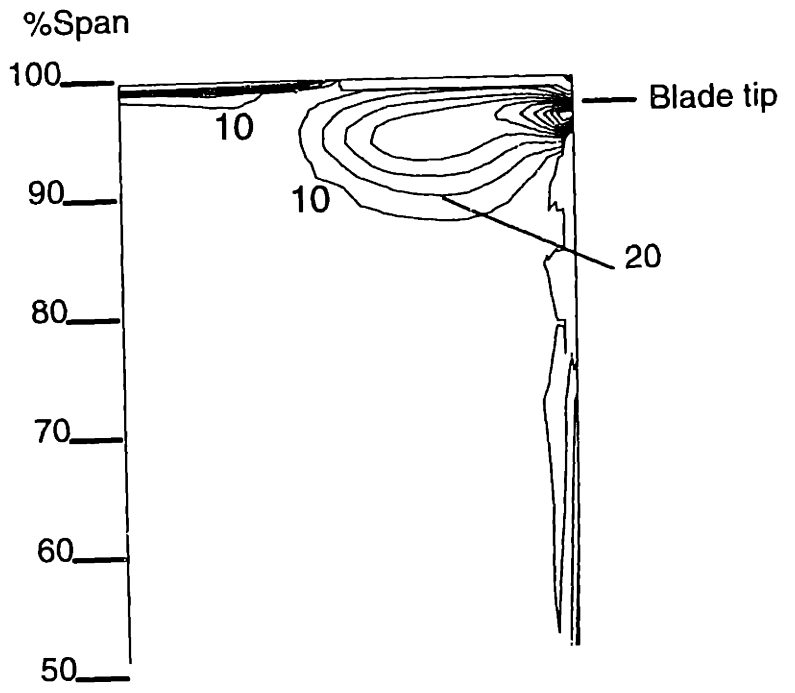

Figure B-4: $\omega_\gamma/(C_x/c)$ near tip in midchord crossflow plane for Navier-Stokes computation.

of the same sign as that shed from the blade tip, so the inclusion of endwall-generated vorticity in the clearance vortex circulation measurement increases the magnitude of the circulation obtained. The figure also indicates that there is more radial spreading of vorticity shed at the blade tip than of the vorticity generated at the endwall.

The circulation was calculated using a trailing edge crossflow plane contour similar to that shown in Figure B-2. The minimum radius segment of the contour was at roughly 50% span and the location of the maximum radius segment (segment A in Figure B-2) was varied between the blade tip and the endwall. Figure B-5 shows $\Gamma/(C_x c)$ calculated around the contour as a function of radial placement of the maximum radius segment. The trend in measured circulation with maximum radius enclosed by the contour is like that sketched in Figure B-3.

The circulation shed from the blade tip can be obtained as the flux of vorticity

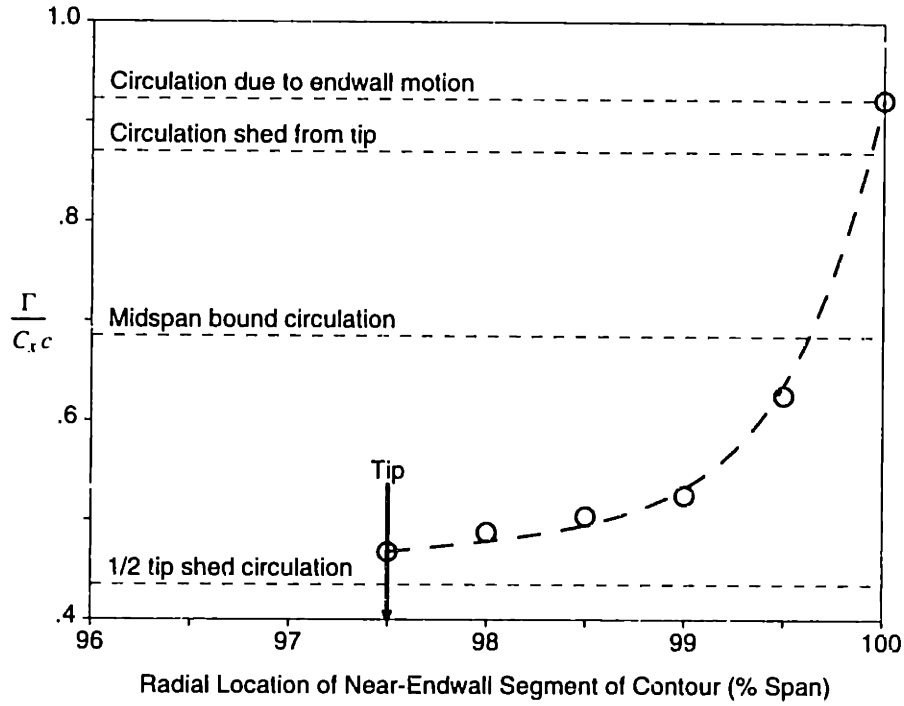

Figure B-5: $\Gamma/(C_x c)$ for computed flow field as a function of radial placement of downstream contour used to measure clearance vortex circulation.

for a surface defined such that it intersects all vortex lines leaving the blade tip and only those vortex lines. This requirement was satisfied by choosing a surface 5% pitch from the suction surface and extending 96 to 98.5% span. The value of $\Gamma/(C_x c)$ obtained with this surface was 0.86. This value indicated as the circulation shed from the tip in Figure B-5 and is essentially the same as the circulation obtained by using a closed contour extending 11.5% pitch from the blade surfaces at the tip radius. The agreement between the shed circulation calculated 5% pitch from the suction surface and the bound circulation demonstrates the importance of entirely and exclusively enclosing the vorticity shed from the blade tip to obtain the blade bound circulation.

Because of the influence of the clearance vortex, the loading near the blade tip excedes the loading at midspan. Thus, as indicated in Figure B-5, the bound circulation at midspan is less than the circulation shed from the blade tip. However, for all the radial placements of the contour which excluded the endwall, the circulation calculated for the clearance vortex is less than the blade bound circulation at midspan. This is consistent with the experimental observation that the measured clearance vortex circulation is less than the blade bound circulation at midspan.

B.3.3 Estimate of spread of shear layer

Diffusion also affects the measured clearance vortex circulation. We can estimate its importance by examining the growth of the shear layer. Although the shear layer formed by the tip leakage flow is not planar and does not have a unique velocity ratio, we can still get a rough idea of the vorticity layer thickness as a function of streamwise distance by using appropriate averages.

To obtain a velocity representative of the leakage side of the shear layer, the velocity resolved into the primary flow direction is area averaged over the clearance. The velocity on the freestream side of the shear layer was represented by the velocity magnitude area averaged over a surface two clearance heights from the endwall. Using these values in the expression for the growth of a shear layer (Dimotakis, 1989) we find that a distance of 50% chord would be required for the vorticity thickness to spread one clearance height (3% of chord). Thus, the the shear layer is likely to be affected by the endwall *within* the blade passage even for this rather large clearance of 3% of chord.

Contours of $\omega_\gamma/(Cx/c)$ in the trailing edge crossflow plane are shown in Figure B-6 from the Navier-Stokes computation. The absence of an irrotational region between the two sources of vorticity (blade tip and endwall) means that the shear layer is affected by diffusion of vorticity from the endwall and one cannot construct a contour which encloses all and only the vorticity shed from at the tip.

B.4 Complexity of Tip Region Flow

Much of past ambiguity concerning clearance vortex circulation appears to stem from oversimplifying the description of the flow in the tip region. Before summarizing the conclusions concerning the measured clearance vortex circulation, therefore, some common misconceptions will be addressed.

Figure B-7 shows velocity vectors viewed normal to the trailing edge crossflow

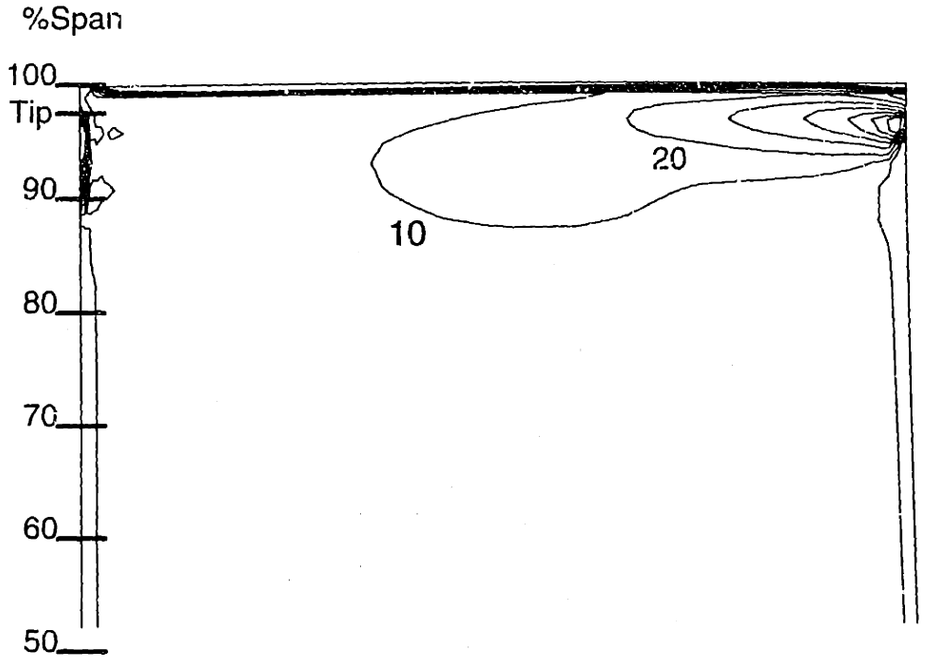

Figure B-6: $\omega_\gamma/(C_x/c)$ near tip in trailing edge crossflow plane for Navier-Stokes computation.

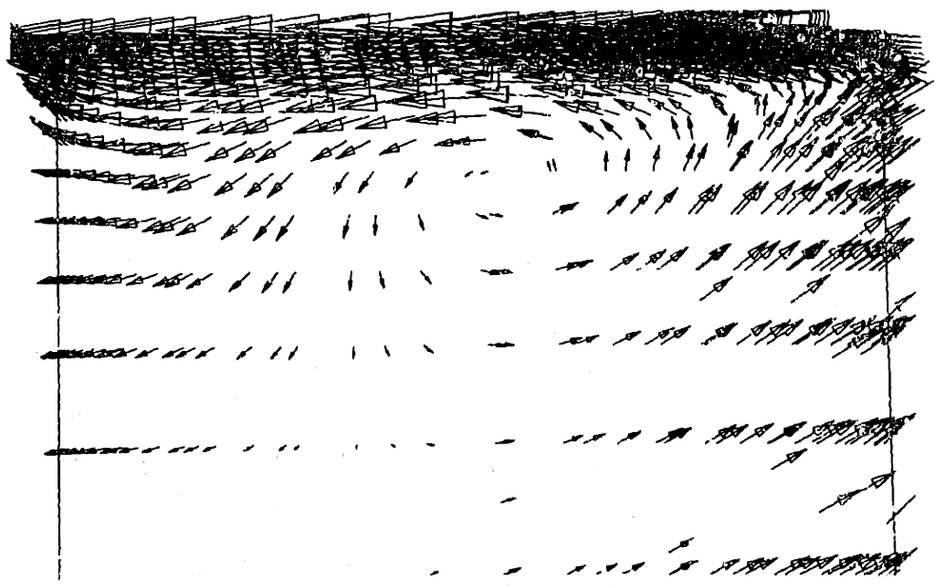

Figure B-7: Velocity vectors viewed along stagger in trailing edge crossflow plane for Navier-Stokes computation, 50–100% span.

plane. Comparing Figures B-6 and B-7 reveals that the vortex core is not the location of maximum ω_γ and that the highest vorticity component normal to the crossflow plane resides outside the vortex core. Thus, one cannot account for the circulation shed from the blade tip by calculating the circulation associated only with the vortex core.

Also, it is inappropriate to attempt to relate the circulation around the clearance space to a lift force there. The Kutta-Joukowsky theorem relates bound circulation to the lift force for a two-dimensional flow. The vorticity shed from the blade is not bound vorticity — it is convected with the flow and sustains no load. As shown in Figure B-2, this vorticity is present in the region between the tip and the endwall. The circulation around contours in a constant radius surface between the tip and the endwall (at the radius of segment A, say) will generally be non-zero.

B.5 Conclusions

For most practical cases, the circulation one measures for a turbomachine tip clearance vortex varies continuously with radial placement of the contour around which the measurement is taken. The primary factors contributing to the discrepancy between blade bound circulation and measured clearance vortex circulation are diffusion of vorticity shed from the blade tip and the proximity of the blade tip to the endwall. Diffusion causes shed vorticity to be transported towards the endwall. The proximity of the endwall prevents one from constructing a contour downstream of the blade which encloses all the vorticity shed from the blade tip and only that vorticity. Therefore, reducing the clearance tends to reduce the measured clearance vortex circulation.

In measuring the circulation associated with the clearance vortex rather than the circulation associated with the relative endwall motion, contours are commonly positioned so as to exclude the endwall. Therefore, measured clearance vortex circulation

is typically less than the circulation shed from the blade tip. This suggests that vorticity generation at the endwall is not a primary factor affecting the measured circulation.

The clearance vortex should not be regarded as an isolated vortex in which all the vorticity is contained within its core. Also, there can be a net circulation in a contour lying in a radial plane between the blade tip and the endwall, even though there is no lift force there.

Appendix C

Evaluating the Mainflow Velocity Component for Transonic Fan Blockage

In Section 3.5.2 the choice of appropriate velocity component to use to quantify blockage was examined using Equation 3.5 and the low speed rotor computations. For two different clearances the ideal core velocity collapsed as a function of mass flow when the mainflow velocity component was used in the defect region.

A similar test can be applied for the transonic fan (Rotor 67) flow fields to determine if the mainflow velocity component in the defect region is responsible for changes in core velocity. However, since density variations are significant Equation 3.5 must be modified so that the product of density and velocity is used in each of the terms where the velocity appears. The core flow angle variation for Rotor 67 is large, roughly 50 degrees, so treating the core flow as if it is unidirectional as in Equation 3.5 is expected to be a poor assumption. The edge criterion used is $|\nabla[\rho v_m]|_{r,\theta}/(\rho_{av}C_x/c) = 3$.

The solid curves in Figure C-1 show $\overline{\rho V}/(\rho_{av}C_x)$ against normalized mass flow. The triangle, square, and circle symbols correspond to 0.25, 1.25, and 2.0% clearances, respectively. Area averaging ρv_m in the defect region with ρV in the core region results

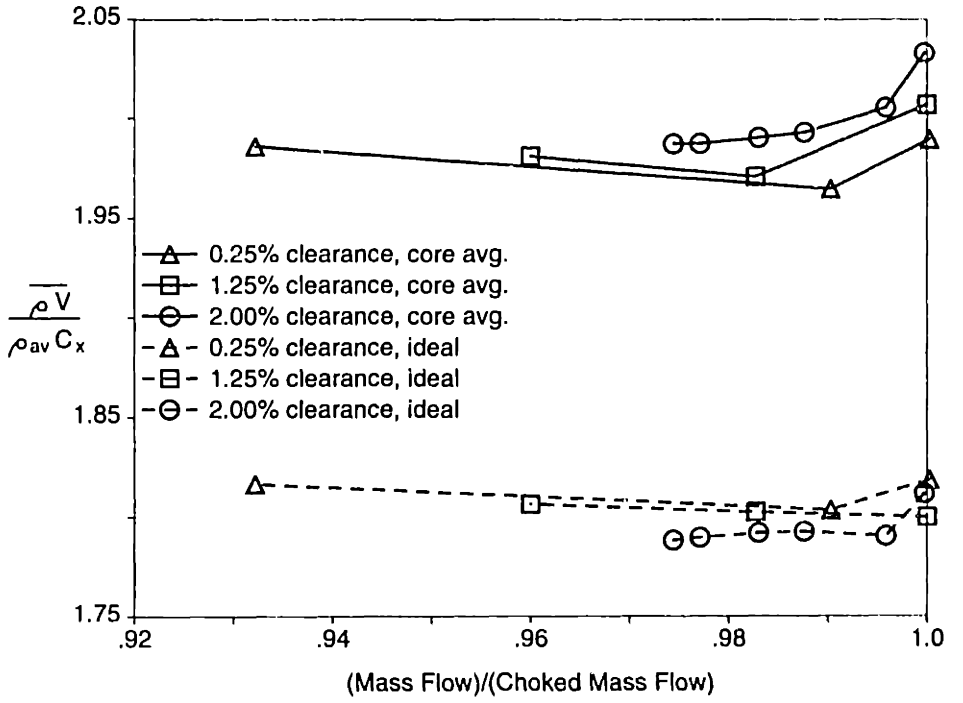

Figure C-1: $\overline{\rho V}/C_x$ and $\rho V_i/C_x$ using v_m vs. normalized mass flow at trailing edge for transonic fan

in dashed curves. The dashed curves are not significantly closer together than the solid curves.

Because the core flow angle variation was large, Equation 3.5 cannot be used to justify using the mainflow velocity component in the blockage definition for the high speed flow fields. However, in Section 3.3.1 it is shown that using the mainflow component is reasonable. Applying Equation 3.5 to the low speed rotor flow fields confirms this assessment. Thus, the mainflow velocity component is used in the blockage definition for both high speed and low speed flows.

Appendix D

Sensitivity of Parametric Dependence to Radial Location of Inlet Dynamic Pressure

In Section 4.3, the radial location two clearance heights from the endwall was used for the inlet reference conditions for the loading parameter. The sensitivity of the loading parameter to the radial location of the reference conditions is examined below.

Figure D-1 shows the non-dimensional blocked area parameter plotted against the loading parameter like that used in Figure 4-8, except that the inlet values of P, P_t, and Q are obtained 3τ from the endwall rather than 2τ. The loading parameter changes little when the inlet reference location is changed by one clearance height, indicating that for the flow fields examined the loading parameter in the tip region is not sensitive to the the radial location of the reference conditions, at least at a distance of a few clearance heights from the endwall.

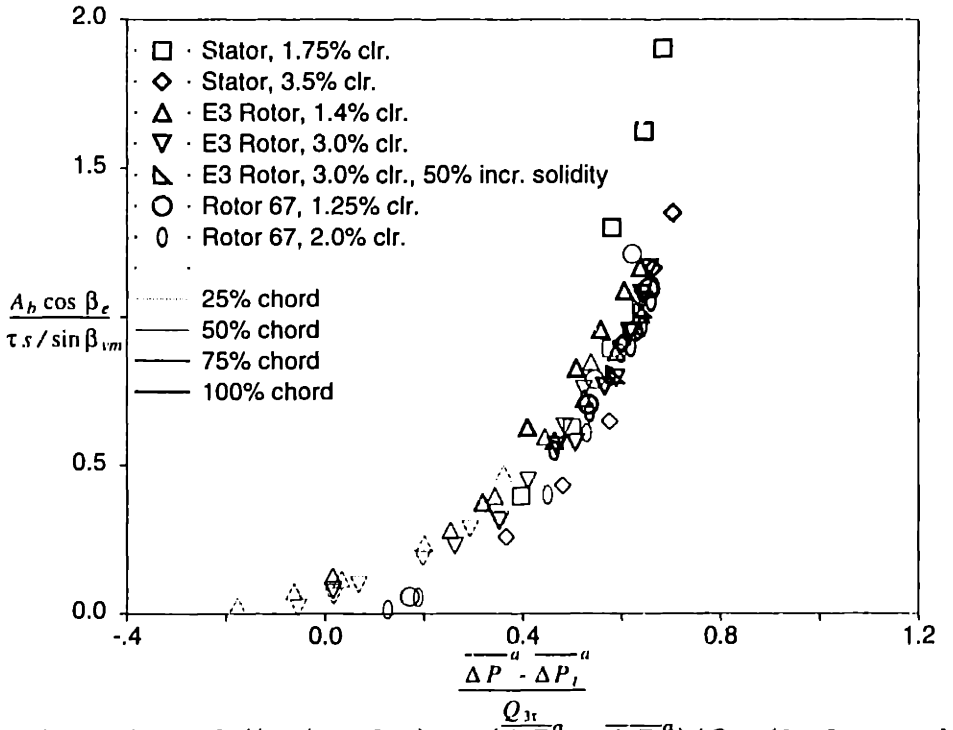

Figure D-1: $A_b \cos \beta_e / (\tau s / \sin \beta_{vm})$ vs. $(\overline{\Delta P}^a - \overline{\Delta P_t}^a)/Q_{3\tau}$ (3τ from endwall used for inlet P and P_t)

Appendix E

Role of Blade Chord in Setting Clearance-related Blockage

In Section 4.3, the blade chord was eliminated from the non-dimensional blocked area parameter by including the ratio of blade to passage pressure differences in the parameter. The lack of dependence on chord is demonstrated below.

Figure E-1 shows clearance-related blocked area normalized by clearance area, τc, for several flow fields and axial locations plotted against the loading parameter used in Figure 4-11. Regardless of the axial location at which the blocked area is evaluated, the normalizing area is the product of the clearance and the full blade chord. The data for all the geometries and axial locations, except for the increased solidity low speed rotor, fall more or less on the same trend, indicating that it does not matter what fraction of chord is used to construct the normalizing area. The geometries which form the trend have solidities near unity.

The data corresponding to the increased solidity low speed rotor, indicated by right triangles, fall below the trend, particularly when compared to symbols corresponding to the same blade geometry with the original solidity. In Figure 4-11, the increased solidity data points fall on almost the same curve as the 3.0% clearance low speed rotor with the original solidity.

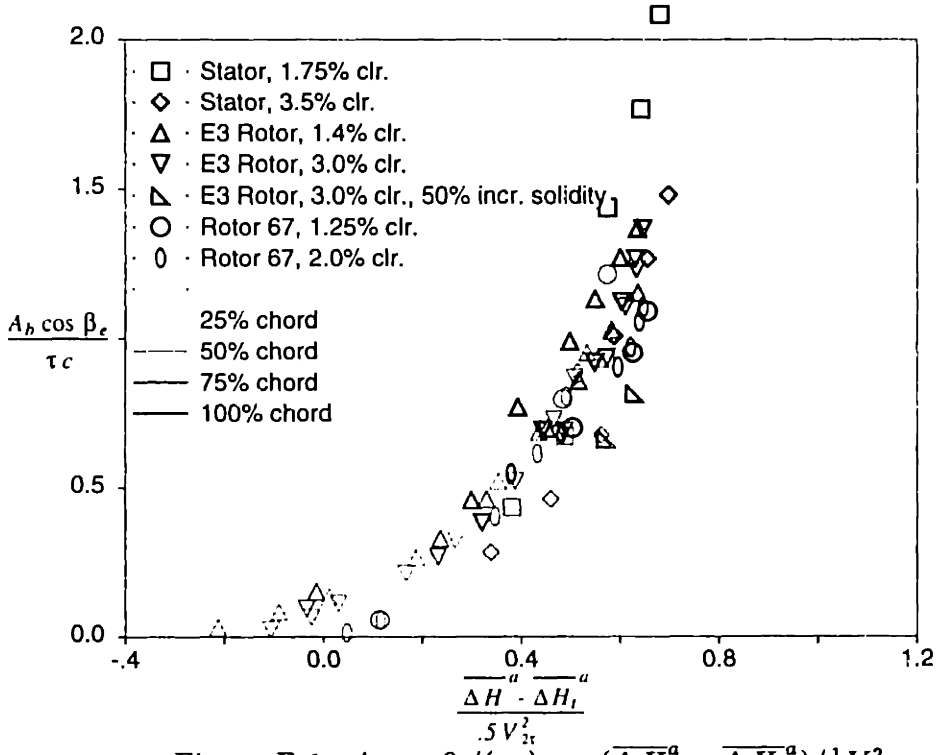

Figure E-1: $A_b \cos\beta_e/(\tau c)$ vs. $(\overline{\Delta H}^a - \overline{\Delta H_t}^a)/\frac{1}{2}V_{2\tau}^2$

Comparison of Figures 4-11 and E-1 demonstrates that it is not chord which determines the blocked area within the passage, but blade spacing.

Appendix F

Sensitivity of Blockage Model to Turbulent Viscosity

For the simple blockage model described in Section 4.4 the value for the turbulent viscosity was assumed to be given by

$$\frac{\epsilon}{U\theta} = 0.18,$$

with the value of 0.18 obtained from a low speed rotor flow field. This value was used for all flow fields and the sensitivity of the results to the constant chosen is examined below.

Figure F-1 shows the results of the normalized trailing edge clearance-related blocked area obtained with the blockage model using $\epsilon/(U\theta) = 0.044$, the value proposed by Schlichting (1960) for two-dimensional turbulent wakes. The value used to obtain Figure 4-16 is a factor of four larger. The trends in blockage indicated by the two figures is essentially the same.

Figure F-2 shows similar results for trailing edge blocked area obtained using $\epsilon/(U\theta) = 0.44$, a factor of ten larger than used in Figure F-1. Even with this significant change in the turbulent viscosity input into the model, there is little change in

the blockage trend.

While these results suggest that the model results that the simple model is insensitive to the value of turbulent viscosity used, they do not imply that the blockage is insensitive to turbulent viscosity. The simple model assumes that downstream wake profiles are similar as shown in Figure 4-12. The mixing is largely fixed by that assumption. It is still necessary to input a nonzero turbulent viscosity, however. Using zero viscosity with the simple model yielded erratic results, with blockage values several times those obtained from the Navier-Stokes computations in some cases and negative values in other cases.

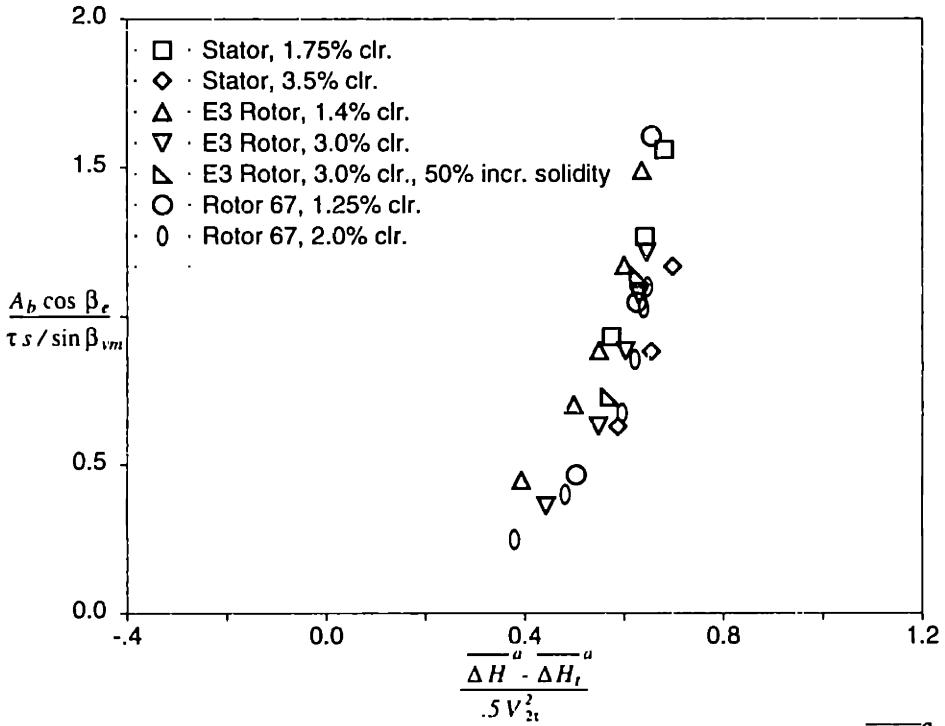

Figure F-1: Simple model trailing edge $A_b \cos\beta_e/(\tau s/\sin\beta_{vm})$ vs. $(\overline{\Delta H}^a - \overline{\Delta H_t}^a)/\frac{1}{2}V_{2\tau}^2$ using the eddy viscosity suggested by Schlichting (1960) for two-dimensional wakes

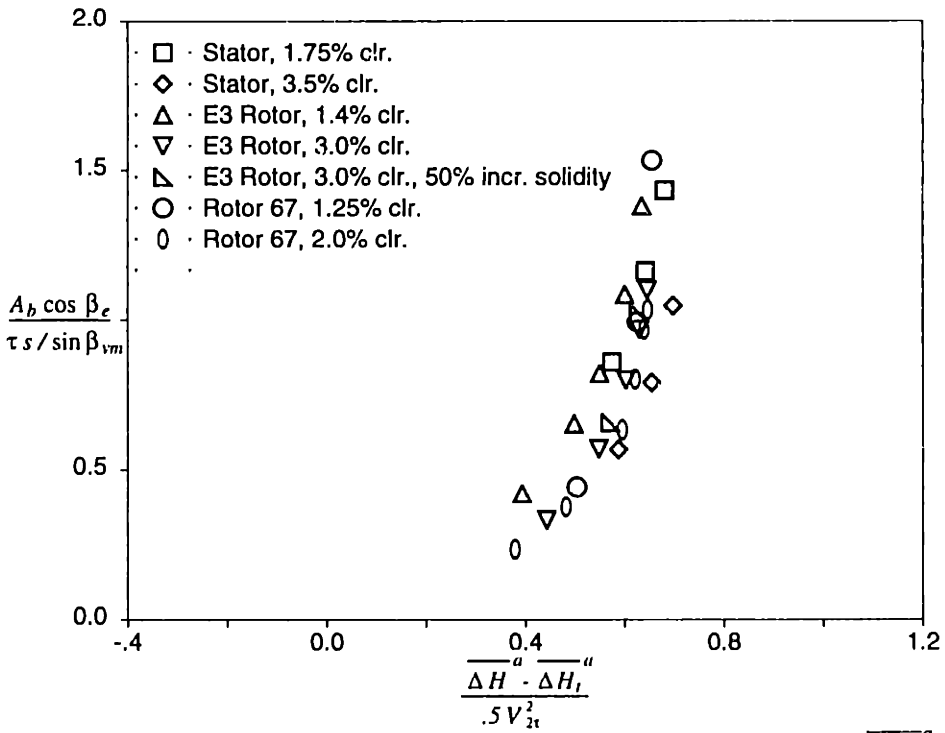

Figure F-2: Simple model trailing edge $A_b \cos\beta_e/(\tau s/\sin\beta_{vm})$ vs. $(\overline{\Delta H}^a - \overline{\Delta H_t}^a)/\frac{1}{2}V_{2\tau}^2$ using ten times the eddy viscosity suggested by Schlichting (1960) for two-dimensional wakes